Interfacial Dynamics in Complex Fluids: Studies of Drop and Free-Surface Deformation in Polymer Solutions

by

Diwen Zhou

A thesis submitted in partial fulfillment of the
requirements for the degree of

Doctor of Philosophy

in

The Faculty of Graduate Studies

(Chemical and Biological Engineering)

The University of British Columbia

(Vancouver)

December 2009

Abstract

Interfacial flows in complex fluids are an important subject, scientifically rich and technologically important. The main scientific attraction comes from the fact that the microstructure of the bulk fluids may evolve during interfacial flow, and thereby generating non-Newtonian stresses that act on the interface. Thus, interfacial motion and conformation of the microstructure are coupled. Such flow situations arise in many industrial applications, including processing of polymer blends, foaming, and emulsification.

In this thesis, I describe three projects aimed at exploring interfacial dynamics of viscoelastic polymeric liquids. The first project consists of finite-element simulations of drop deformation in converging flows in an axisymmetric conical geometry. The moving interface is captured using a diffuse-interface model and accurate interfacial resolution is ensured by adaptive refinement of the grid. The drop experiences a predominantly elongational flow. The amount of deformation sustained by the drop depends, besides the geometry and kinematics of the flow, on the rheology of both the drop and the matrix fluids. The second and third projects concern the same process of selective withdrawal, in which stratified layers of immiscible fluids are withdrawn from a tube placed a certain distance from the interface. We have chosen to work with an air-liquid system, with the suction tube embedded in the Newtonian or viscoelastic liquid. The second project is an experimental study, where we used video recording and imaging processing to analyze how the interfacial deformation is influenced by the non-Newtonian rheology of the liquid. We discover three regimes, subcritical, critical and supercritical. The third project consists of sharp-interface, moving-grid finite-element simulations of selective withdrawal for Newtonian and viscoelastic Giesekus liquids. The experiments and computations are in reasonable agreement.

The work of this thesis has led to two main outcomes. The first is a detailed understanding of how viscoelastic stress can lead to unusual and sometimes counter-intuitive effects on interfacial deformation. The second is a potentially important new method for measuring elongational viscosity of low-viscosity liquids. This is worth further investigation considering the poor performance of existing methods.

Contents

List of Tables

List of Figures

List of Symbols

a	Radius of drop
A	Y-intercept of the fitting function between $\log \xi$ and χ
b	Half-breadth of the deformed drop
B	Slope of the fitting function between $\log \xi$ and χ
Bo	Bond number
Ca	Capillary number
Cn	Cahn number
D	Drop deformation
$\boldsymbol{D}$	Strain-rate tensor
D_a	Diameter of air jet
De	Deborah number
$\boldsymbol{e}_i$	Eigen-vectors of $\boldsymbol{D}$
E	Elasticity number
g	Gravity
G	Chemical potential
G_1	Grading factor
h	Distance between tip and orifice of tube
h_1	Mesh size in the interface
h_2	Mesh size in the component $\phi = -1$
h_3	Mesh size in the component $\phi = 1$
H	Distance between the liquid level on the side wall and orifice of tube
k	Solvent viscosity ratio in Giesekus model
l	Half-length of the deformed drop
L	Length of the converging channel

L_1	Height of the computation domain for selective withdrawal
L_t	Length of the channel
N_1	First normal stress difference
N_1^{max}	Maximum N_1
$\boldsymbol{O}$	Local rotation of the strain-rate tensor
p	Pressure of the flow
p_1	Pressure at tip
p_2	Pressure at the side wall
p_a	Atmospheric pressure
Q	Flow rate at outlet
r	Radius of cylindrical coordinates
R	Diameter of orifice of tube
R_1	Inlet diameter of channel
R_2	Outlet diameter of channel
Re	Reynolds number
Re_t	Transient Reynolds number
S	Slope of drop deformation in converging channel
t	Time
t_{tr}	Total transit time in converging channel
t_{em}	Emulsion time
T	Time scale for the transient
$\boldsymbol{v}$	Velocity vector of the flow
v_0	Centerline velocity in z direction on the boundary
v_r	Velocity in r direction
v_z	Velocity in z direction
V^*	Critical value of bubble volume
w	Half-wide of the computational domain for selective withdrawal
$\boldsymbol{W}$	Modified vorticity tensor
z	Axial position of cylindrical coordinates

Greek letters

α	Mobility factor in Giesekus model
β	Drop-to-matrix viscosity ratio
β_M	Critical value of β
γ	Molecular mobility
$\boldsymbol{\gamma}$	Strain tensor
$\dot{\gamma}$	Strain rate
$\dot{\gamma}_1$	Shear rate
ϵ	Capillary width
$\dot{\epsilon}$	Extensional rate
$\bar{\dot{\epsilon}}$	Average extensional rate in the converging channel
η	Extensional viscosity
η_G	Extensional viscosity of Giesekus fluid
$\bar{\eta}$	Steady extensional viscosity
$\bar{\eta}^+$	Transient extensional viscosity
θ	Azimuth of cylindrical coordinates
κ	Curvature of tip
λ	Mixing energy density
λ_H	Relaxation time of polymer
μ	Shear viscosity of fluid
ν	Viscosity ratio between the liquid on the opposite side of nozzle and the liquid containing nozzle
ξ	Dimensionless extensional rate
ξ_c	Calculated dimensionless extensional rate
ρ	Density of fluid
ρ_1	Density of fluid component $\phi = -1$
ρ_2	Density of fluid component $\phi = 1$
σ	Interfacial tension or surface tension
$\boldsymbol{\Omega}$	Vorticity tensor
τ	Stress of flow
$\boldsymbol{\tau}$	Stress tensor

ϕ	Phase field parameter
χ	Dimensionless hump height
ψ	Flow type parameter
ω	Drop-to-matrix density ratio

Subscripts

d	Drop flow regime
m	Matrix flow regime
n	Newtonian fluid
p	Polymer component in Giesekus fluid
s	Solvent component in Giesekus fluid

Superscripts

$*$	Critical value
T	Transposition of tensor

Abbreviations

ALE	Arbitrary Lagrangian-Eulerian
AMPHI	Adaptive Meshing for Phase Field (ϕ)
CCD	Charge coupled device
GRUMMP	Generation and Refinement of Unstructured Mixed-element Meshes in Parallel
PB	Polybutene
PIB	Polyisobutene
SE	Strongly elastic
WE	Weakly elastic

Acknowledgements

I would like to express my gratitude to my supervisor Dr. James J. Feng, whose abundant knowledge, distinguished supervision and patience helped me in all the time of research and writing of this thesis.

I am indebted to Dr. Mark Martinez, who gave me guidance and suggestion about my experiment.

I want to thank my colleagues Dr. Pengtao Yue and Dr. Chunfeng Zhou for their important suggestion and help about my work, Dr. Zhiwei Chen and Dr. Steve Cochard for their help in the experiment and Wendi Guo for her support.

I also thank the staff of the Department of Chemical and Biological Workshop and Stores for their assistance.

Finally, I want to give my special thanks to my parents, for their love, understanding and encouragement.

Chapter 1

Introduction

1.1 Interfacial flows of complex fluid

Interfacial flows occur in two-component or multi-component systems with interface between the components. Many such flows exist in nature. For example, rain drops form when water vapor condenses in the atmosphere. This creates myriad air-water interfaces and a two-component system. As the drops grow too large to be suspended in a cloud, they fall down as rain. During the process of falling down, the drops may break up or coalesce with other drops. After the drops hit the surface of a solid substrate, they may splash, adhere and spread or fall off entirely without wetting the surface. Such wetting behavior depends on the contact angle of the drop on that surface, and is related to the mechanism of capillarity. In this context, a key property of the interface is the interfacial tension, also known as surface tension if one of the component is air. An intriguing demonstration of the surface tension of water is the water strider, an insect that floats on water and occasionally jumps up and falls back onto the water surface, all without sinking despite its weight. Because air has very low viscosity and density, air-liquid interfaces are sometimes called "free surfaces" based on the notion that the air exerts little affect on the interface.

Interfacial flows also play central roles in industry and technology. The manufacturing of two-phase materials, ranging from polystyrene foam to whipped cream, depends on interfacial flows. In polymer foams, in particular, the property and performance of the solidified material depend critically on the morphology of the interface [9], which is determined in turn by the interfacial flow during the molding or extrusion of the foam in the fluid state.

Polymer blends are another important class of composite materials whose processing relies on interfacial flows. In this case, the dispersed component first appears as drops suspended in a matrix of the other component. During forming of the polymer melts, the drops may be elongated into fibers, which may break up into finer droplets. For applications as structural materials, the fibrillar morphology is most advantageous since it affords excellent strength to the final product [10]. Again, the processing flow determines the morphology of the interfaces, which to a large extent determine the property of the final product. Other examples of interfacial flow include emulsification in oil extraction from tar sand [11] and chemical reactors that involve atomization or mixing of components [12]. In recent years, interfacial flows have found applications in microfluidic devices [13–16].

From a fundamental viewpoint, interfacial flows are intriguing because the position and morphology of the interfaces are not fixed but variable. The interfaces evolve as a result of the fluid forces arising from the bulk flow on either side. Thus, these flows provide an interesting case study where the usual fluid dynamics is coupled with morphological changes of these internal boundaries. In addition, interfaces are susceptible to non-hydrodynamic factors such as surfactants, electric fields and thermal gradients. These modify the interfacial tension, and consequently the fluid dynamics of the whole system. Interfacial flows in industrial processes often involve *complex fluids* [17]. This term refers to fluids such as polymers and liquid crystals that possess a *microstructure* that evolves in a flow and produces an additional stress that modifies the flow in return. In such systems, the rheology of the bulk fluids is coupled with the interfacial motion, and both contribute to the complexity of interfacial flows.

The studies reported in this thesis center on the idea that complex rheology in the liquid bulk modifies interfacial dynamics in important and sometimes unintuitive ways. In Newtonian fluids, the stress tensor is a linear function of the shear-rate tensor. Complex fluid are non-Newtonian with more complicated constitutive equations. For example, the stress may depend on the shear-rate nonlinearly (e.g., in a power law) for *shear-thinning* fluids [18]. More commonly, the stress may not only be a function of the shear-rate but also depends on the history of the deformation. This behavior, known as *viscoelasticity*, characterizes most polymer solutions and melts. Because of its importance, we give several examples to illustrate the role of complex rheology in interfacial flows.

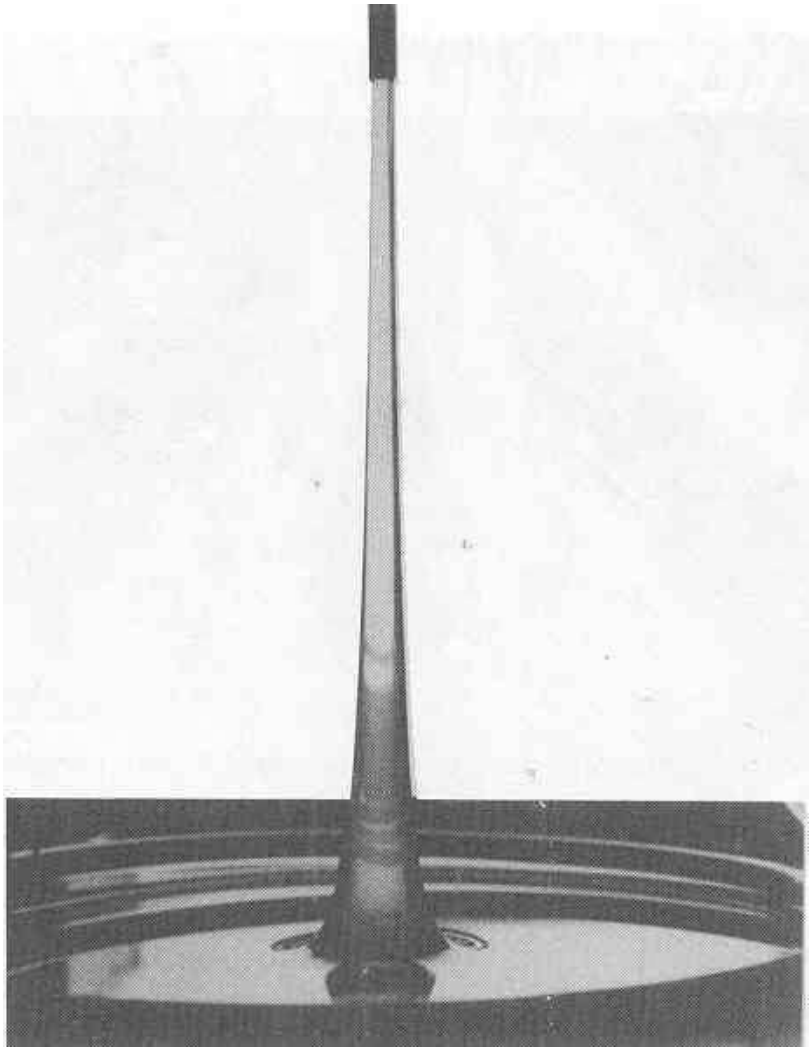

Figure 1.1: Tubeless siphon, from Peng and Landel [1]. The liquid is a high molecular weight hydrocarbon polymer (Conoco AM-1) in a jet fuel (JP-8) solvent.

The first example is the so-called tubeless siphon. When siphoning a Newtonian liquid, the opening of the tube must remain under the surface of the liquid. If we pull the tube out of the liquid bath, the liquid falls down and the suction stops. A different scenario takes place for a polymer solution (Fig. 1.1). If one pulls the orifice of the tube above the surface, the suction will not stop. Rather, the liquid continues to flow up in mid-air and enters the tube continuously. This is because the polymer solution, under stretching, could offer additional elongational stress to balance the surface tension and gravity of the thread.

Another intriguing phenomenon is the rise of air bubbles in a complex fluid. When an air bubble rises in a Newtonian fluid by buoyancy, the top of the bubble is round and the rear part is more or less flat. But in complex fluid, the shape of bubble can be quite different. Figure 1.2 shows the steady-state shape of bubbles of different volume rising in a polymer solution. When the volume exceeds a critical value ($V^* > 1$ in the pictures), the bottom of the bubble protrudes and forms a very long tail. This is because the strong extensional flow near the bottom of the bubble produces a large polymer stress, which overcomes the interfacial tension. Figure 1.3 shows the transient shape of an air bubble as it rises in a micellar solution. The bubble was created when a solid sphere plunges into the solution. When the bubble is in the near wake of the sphere, it shows a peculiar "inverted-heart" shape. As it moves farther away from the sphere, it recovers a shape typically of bubbles in viscoelastic solutions, with a round top and pointed bottom, similar to some of the pictures in Fig. 1.2. The inverted-heart shape has been attributed by Zhou *et al.*[ref] to a temporary nematic alignment of the micelles created by the flow in the wake of the sphere. Still more complex phenomena of interfacial flow in complex fluid include the Uebler effect [18,19] and self-assembly of droplets in nematic liquid crystals [20].

1.2 Research methodology

All three classes of research tools for fluid dynamics—experiment, theoretical analysis and numerical simulation—have been used to study interfacial flows in complex fluids. For example, Belmonte and coworkers have documented unusual surface dynamics of polymer and micellar solutions [21, 22]. Belmonte, McKinley and others have studied the equivalent

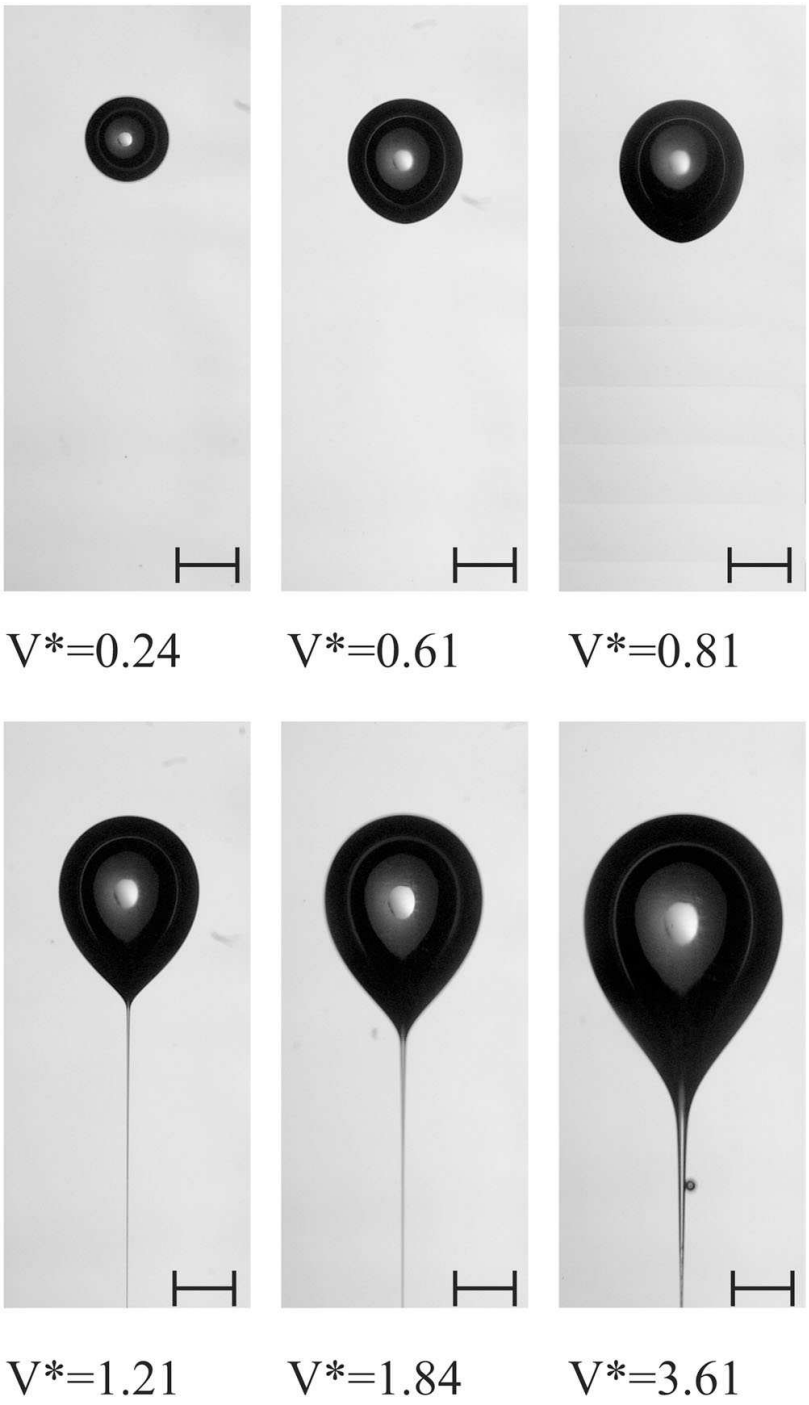

Figure 1.2: Steady-state shape of bubbles of different volume rising in a polymer solution [2]. The material used here is the Aqueous solution of HASE (Primal TT-935) on the weight concentration of 1.7%. The V^* in the picture is the dimensionless volume of the bubble, which is scaled by the critical volume. ©2006 American Institute of Physics

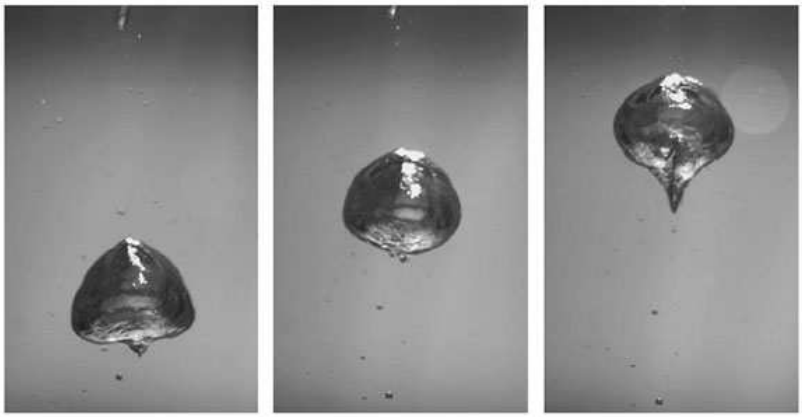

Figure 1.3: bubble rising in micellar solution [3]. The material used here is aqueous solution of the wormlike micellar system cetylpyridinium chloride (CPCl)/sodium salicylate (NaSal).

of Rayleigh breakup of a viscoelastic filament, and documented the formation of the bead-on-string morphology [23,24]. Shaqfeh *et al.*observed surface instability of polymeric liquids in coating flows [25]. Spaid and Homsy recorded viscoelastic contact line instability in spin coating [26]. Analytically, lubrication models have been developed by a number of authors to describe the flow of thin films of Newtonian and non-Newtonian fluids, ranging from spin coating to spreading of drops on substrates [27–29].

For numerical simulation of interfacial flows, we give a somewhat more detailed overview here because it is a relatively new development and particularly relevant to the work reported in this thesis. A conceptual problem is the mathematical representation of the interface. In the early 1800s, Young, Laplace and Gauss viewed the interface as a surface of zero thickness [30]. This surface has all the physical properties of the real surface such as interfacial tension. They also assumed that the physical properties such as density and viscosity would be discontinuous on the interface. This idea of sharp and discontinuous interfaces is conceptually simple, but produces a problem with moving internal boundaries that is difficult to compute numerically. The bulk fluids on both sides of the interface have their own governing equations, which are solved with boundary conditions that must be matched on the moving interfaces. Since the location of the interfaces is not known a priori, it has to be solved together with the governing equations in the bulk. Such methods typically require tracking of the interface with grid points and a deforming or moving grid [31].

They work well when there is no topological changes of the interface. But if the interface undergoes breakup or coalescence, these methods would break down, which is often avoided by an ad hoc scheme to remove or connect interfaces "manually". There are also situations where the interface cannot be considered thin relative to other length scales of the problems. This arises, for example, for gas-liquid systems near the critical condition [32] or during phase change [32]. With the advent of nanofluidics, the overall length scale of the problem may be so small that the thickness of interfaces becomes appreciable.

An alternative to the traditional sharp interface formalism is the diffuse-interface model. There are at least two aspects to this, one physical and the other computational. The physical origin of the diffuse interface goes back to van der Waals [33], who viewed the interface not as a mathematical surface separating two fluids, but as a thin but finite transition region in which the two species mix to a limited extent. This led to the formulation of a mixing energy which gives rise to a counterpart of the interfacial tension. The computational aspect emerged much more recently, of course, when sharp-interface simulations of interfacial flows encountered various difficulties. For one, the interfacial discontinuity calls for matching of boundary conditions on a moving internal boundary. Moreover, grid representation of moving interfaces also runs into difficulties with catastrophic morphological changes such as breakup and coalescence. In such cases, the diffuse-interface model affords a more natural and computationally more rational approach to robust algorithms [34, 35].

Although the diffuse-interface method is a powerful method for interfacial flows, it has its own shortcomings. First, in reality, the thickness of the interface between two immiscible fluids is on the order of 10 nm. In our simulation, the thickness of the mixing layer cannot reach down to this length scale. Usually, it is 1/40 of the characteristic length in the calculation (such as drop radius). This thick interface may introduce large errors when the deformation of interface is very large. Secondly, the diffuse-interface method has difficulty handling very large viscosity and density ratios.

In the thesis research reported herein, we have employed experimental observation and numerical simulations, the latter using both sharp-interface and diffuse-interface models. The choice of one over another depends on the nature of the problem, and we will give more details of the methodology in the following chapters.

1.3 Scope of the thesis

In this Ph.D. dissertation, my general goal is to probe the coupling between bulk rheology and interfacial deformation in polymer solutions. In other words, we study how the non-Newtonian stresses, especially the viscoelastic normal stresses, change interfacial deformation, and how the interfacial morphology affects the flow field in return. For this purpose, we have selected three projects:

(a) Simulation of drop deformation in converging flows. In the first project, I study the drop deformation under an inhomogeneous flow in a converging axisymmetric channel. This introduces a complex deformation history and interesting development of the polymer stress, which is reflected by the drop deformation. A diffuse-interface finite-element method is used, with the moving interface being captured by a phase-field parameter. Accurate interfacial resolution is ensured by adaptive refinement of the grid.

(b) Experimental study of selective withdrawal in polymer solutions. For the second and third projects, I study the deformation of the free surface of a viscoelastic liquid induced by a suction tube placed some distance below the interface. For historic reasons this process is known as selective withdrawal. In the first project, we study the selective withdrawal of Newtonian and polymer solutions experimentally. The main finding is that viscoelastic polymer stress in the liquid modifies the surface deformation fundamentally.

(c) Simulation of selective withdrawal in viscoelastic liquids. The third project complements the second in that I carry out simulations of the same selective withdrawal process, with the aim of predicting the experimental observations. Because the surface becomes highly deformed in selective withdrawal, we encounter very high curvatures of the interface that is difficult to capture using diffuse-interface models. Thus, we have adopted a sharp-interface Arbitrary-Lagrangian-Eulerian scheme to compute the interfacial deformation. By comparison with experiments, the numerical results confirm the role of highly developed polymer stresses near the deformed interface. Furthermore, we suggest that this configuration may potentially be used to measure the elongational viscosity of complex fluids.

The three projects are reported in the following three chapters, and the final chapter presents a summary of conclusions and offers suggestions for future work.

Chapter 2

Drop deformation in converging flow

2.1 Introduction

Drop deformation in a flowing medium is important to processing engineering materials such as emulsions and polymer blends [36] and to physiological processes in microcirculation [37]. In both contexts, the fluid components are often non-Newtonian complex fluids containing macromolecules, and the drop deformation depends on their viscoelastic rheology. In homogeneous shear and extensional flows, numerous studies have formed a rather coherent picture on how capillary, viscous and viscoelastic forces affect drop deformation [38–48]. In simple shear flows, viscoelasticity in the drop tends to reduce drop deformation while that in the matrix has a non-monotonic effect: it reduces drop deformation in lower Deborah number but increases drop deformation with stronger viscoelasticity [45]. In uniform extensional flows, a polymer drop deforms less than its Newtonian counterpart while a polymer matrix tends to enhance drop deformation [40–42]. This is consistent with the heuristic idea that drop deformation is controlled by the balance among fluid stresses inside and outside and the interfacial tension [49].

In comparison, our knowledge of drop deformation in *inhomogeneous* flow geometries, such as channels or pipes with varying cross sections, is rather fragmentary and sometimes contradictory. In the conical section of a converging pipe flow, a drop moving along the centerline experiences inhomogeneous and time-dependent elongation. Of the handful of experiments

in this geometry, Chin and Han [50] reported that increasing the polymer concentration in the drop fluid suppresses drop deformation, while increasing the polymer concentration in the matrix has the opposite effect. This seems consistent with the behavior in homogeneous elongation. The more recent experiment of Bourry *et al.* [51], on the other hand, was inconclusive as to whether a polymeric drop deforms more or less than a Newtonian one with comparable viscosity. Both experiments were complicated by the strong strain-rate-dependent rheology of the fluids; it is uncertain whether the effect is due to elasticity or viscosity that has changed with the deformation. As a matter of fact, Kim and Han [52] later attributed the observations of Chin and Han [50] entirely to viscosity. Mighri *et al.* [53] attempted to clear up this issue by carrying out similar experiments with Boger fluids in one or both components. Their results seem in agreement with the simple argument advanced in homogeneous elongational flows: polymer in the drop hinders its deformation while that in the matrix enhances deformation. These authors further correlated drop deformation with the difference in elasticity between the drop and the matrix. In the only theoretical or computational study known to us, Kayat [54] computed drop deformation in a conical pipe using a linear Oldroyd-B model. The results exhibit the opposite trend to that of Mighri *et al.* [53]. That is, a polymeric drop deforms more while a polymeric matrix causes a suspended drop to deform less.

This contradiction was the initial motivation for the present work. Using the nonlinear Giesekus model, we have systematically investigated the effect of viscoelasticity on drop deformation in a converging pipe flow over a wide range of the Deborah number. The results reveal an intricate picture that contains both prior studies as special cases at opposite ends of the parameter space. Note that historically, the conical geometry has been used as an *imperfect* device for generating elongational flows in which to measure the fluid's elongational viscosity [55] or to study drop deformation [50]. Our perspective is different: we see this not only as a prototypical geometry for various polymer processing operations, but also as an inhomogeneous flow that is simple enough to allow detailed analysis of the fluid mechanics of drop deformation.

2.2 Viscoelasticity and constitutive equations

Polymer melts and solutions exhibit viscoelasticity in the sense that the material behaves elastically on a short time scale, but flows like a viscous liquid over a long time scale. In the literature, this behavior has been studied through two different routes. Microscopically, viscoelasticity has been attributed to flexible chain-like macromolecules that stretch and relax under deformation. The conformational changes occur on an inherent time scale, the relaxation time λ_H, and the macromolecules collectively generate a stress that depends on their configuration. Based on this picture, so-called kinetic theories can be developed [56] based on (a) an convection-diffusion equation that describes how the polymer configuration evolves in a flow field; and (b) a polymer stress tensor expressed in terms of the statistics of polymer configuration. Effectively, these two equations connect the polymer stress tensor to the flow field (more specifically, the strain rate tensor and its temporal and spatial gradients), and form a complete *constitutive equation* for the polymeric liquid. The simplest such model is the linear elastic dumbbell model for dilute polymer solutions [56], which gives rise to a constitutive equation known as the Oldroyd-B equation. The more sophisticated kinetic models deal with entanglement among polymer chains in concentrated solutions and melts, with the best known example being the Doi-Edwards model [57].

The macroscopic or continuum-mechanical approach to viscoelasticity aims to write down partial differential equations that capture the behavior of the material. The simplest models can be written based on heuristic spring-dashpot models due to Maxwell and Kelvin [58]. These can be generalized to multiple dimensions and reformulated using Oldroyd's convective derivations to make them frame-independent [18]. The most widely used model is perhaps the Oldroyd-B model:

$$\boldsymbol{\tau} + \lambda_H \boldsymbol{\tau}_{(1)} = \mu(\boldsymbol{\gamma}_{(1)} + \lambda_2 \boldsymbol{\gamma}_{(2)}) \tag{2.1}$$

where $\boldsymbol{\tau}$ and $\boldsymbol{\gamma}$ are the stress and strain tensors, μ is the shear viscosity; λ_H is the relaxation time; and λ_2 is the retardation time. The subscript $_{(i)}$ to a tensor $\boldsymbol{A}_{(i)}$ denotes the convected time derivative:

$$\boldsymbol{A}_{(i)} = \frac{D}{Dt}\boldsymbol{A}_{(i-1)} - (\nabla \boldsymbol{v})^{\mathrm{T}} \cdot \boldsymbol{A}_{(i-1)} + \boldsymbol{A}_{(i-1)} \cdot \nabla \boldsymbol{v} \tag{2.2}$$

$$\boldsymbol{A}_{(0)} = \boldsymbol{A} \tag{2.3}$$

It is among the favorite constitutive equations for numerical computation because it is relatively simple but captures the key features of viscoelasticity. For example, in abrupt start and cessation of shear and elongational flows, the Oldroyd-B model predicts an exponential growth and relaxation of the stress tensor on the time scale of λ_H. In simple shear of shear rate $\dot{\gamma}$, it predicts a normal stress difference that scales with $\dot{\gamma}^2$. However, there is no shear thinning. In steady homogeneous elongational flow, it predicts an elongational viscosity that increases with the strain rate $\dot{\epsilon}$. Compared with experimental data for typical polymer solutions, the Oldroyd-B falls short in that it does not predict shear-thinning, and has a stress blowup in elongational flows as $De = \lambda_H \dot{\epsilon} \to 0.5$. The former might not be a grave concern for the Boger fluids, i.e. dilute polymer solutions with little shear-thinning. But the latter is a major problem for elongation-dominated flows.

In these aspects, the Giesekus model is superior. It has an additional quadratic stress term that acts to produce shear-thinning and avert the singular stress blowup in elongational flows [18]:

$$\boldsymbol{\tau} = \boldsymbol{\tau}_s + \boldsymbol{\tau}_p, \tag{2.4}$$

$$\boldsymbol{\tau}_s = \mu_s \boldsymbol{\gamma}_{(1)}, \tag{2.5}$$

$$\boldsymbol{\tau}_p + \lambda_H \boldsymbol{\tau}_{p(1)} + \alpha \frac{\lambda_H}{\mu_p} \boldsymbol{\tau}_p \cdot \boldsymbol{\tau}_p = \mu_p \boldsymbol{\gamma}_{(1)}, \tag{2.6}$$

where α is the mobility parameter and μ_s and μ_p are the solvent and polymer viscosities, respectively. The computations to be reported in this chapter and later in chapter 4 will be based on both the Oldroyd-B and Giesekus models.

Finally, we must mention the connection between the kinetic and continuum approaches to viscoelsticity. As it turns out, the Oldroyd-B model can be derived from a kinetic theory for a dilute solution of linear elastic dumbbells in a Newtonian solvent. The convective derivatives, originally proposed by Oldroyd to avoid dependence on reference frames, arise naturally from the convection of the dumbbells in the flow field. Similarly, the Giesekus model corresponds to a dumbbell model incorporating anisotropic effects in the Brownian motion and friction force on the polymer chain [56].

2.3 Theoretical model and numerical method

2.3.1 Diffuse-interface model

To simulate a moving internal boundary, one either tracks it with boundary grids that are part of a moving mesh or captures it on a fixed grid using some scalar field [31]. In this work, we employ the diffuse-interface method in the latter category. In this model, the two nominally immiscible fluid components are assumed to mix in a thin interfacial region; a phase field ϕ varies smoothly from one bulk value ($\phi = -1$) to the other ($\phi = 1$) The interfacial tension derives from a mixing energy that is a functional of ϕ. One advantage of this method is in handling morphological changes such as drop coalescence [59]. But in the present problem, it is mostly a numerical device for capturing the deforming and moving drop surface. The diffuse-interface model has been the subject of several reviews [32, 35, 60], and the numerical implementation used here has also been detailed before [46]. Therefore, we will give only a brief outline in the following.

Through a formal variational procedure, one may derive the governing equations of a two-phase system consisting of a Newtonian fluid and a Giesekus fluid:

$$\nabla \cdot \boldsymbol{v} = 0, \tag{2.7}$$

$$\rho\left(\frac{\partial \boldsymbol{v}}{\partial t} + \boldsymbol{v}\cdot\nabla\boldsymbol{v}\right) = -\nabla p + \nabla\cdot\boldsymbol{\tau} + G\nabla\phi, \tag{2.8}$$

$$\boldsymbol{\tau} = \left(\frac{1-\phi}{2}\mu_n + \frac{1+\phi}{2}\mu_s\right)[\nabla\boldsymbol{v} + (\nabla\boldsymbol{v})^{\mathrm{T}}] + \frac{1+\phi}{2}\boldsymbol{\tau}_p, \tag{2.9}$$

$$\boldsymbol{\tau}_p + \lambda_H \boldsymbol{\tau}_{p(1)} + \alpha\frac{\lambda_H}{\mu_p}\boldsymbol{\tau}_p\cdot\boldsymbol{\tau}_p = \mu_p[\nabla\boldsymbol{v} + (\nabla\boldsymbol{v})^{\mathrm{T}}], \tag{2.10}$$

$$G = \lambda\left[-\nabla^2\phi + \frac{\phi(\phi^2-1)}{\epsilon^2}\right], \tag{2.11}$$

$$\frac{\partial\phi}{\partial t} + \boldsymbol{v}\cdot\nabla\phi = \gamma\nabla^2 G, \tag{2.12}$$

where $\rho = \frac{1-\phi}{2}\rho_1 + \frac{1+\phi}{2}\rho_2$ is the average density between the two fluids, G is the chemical potential derived from a Landau-Ginzburg mixing energy, μ_n is the viscosity of the Newtonian component, and μ_s and μ_p are the solvent and polymer viscosities of the Giesekus component. In the Giesekus model, λ_H is the polymer relaxation time, α is the so-called mobility factor, and the subscript (1) denotes upper convected derivative [18]. We have taken the

Newtonian component to be fluid 1 ($\phi = -1$) and the Giesekus component fluid 2 ($\phi = 1$). In the simulations, either may be the drop or matrix fluid. The diffuse-interface model has 3 parameters: the mixing energy density λ, the capillary width ϵ and the molecular mobility γ. These are chosen so that the proper sharp-interface limit is approached [61–63], with the interfacial tension being $\sigma = \frac{2\sqrt{2}}{3}\frac{\lambda}{\epsilon}$.

The Giesekus model is used chiefly because it strikes a balance between simplicity and realistic rheological predictions. Derived from a dumbbell model with anisotropic viscous friction and Brownian motion [56], the Giesekus model is perhaps the simplest nonlinear model with reasonable normal stress differences. Applied to polymer melts and solutions in step shear, startup of uniaxial elongation and step biaxial extension, the Giesekus model "can describe the shear damping function and elongational viscosity quite accurately" [64, 65]. In prior computations on drop breakup and coalescence, the Oldroyd-B model sometimes caused difficulties in convergence [66]. Although this is not a concern for the relatively mild strain rates in this work, we nevertheless prefer the Giesekus model as it better represents the rheology of real polymeric liquids.

2.3.2 Computational scheme

The computations are done in an axisymmetric geometry using AMPHI, a finite-element package based on the diffuse-interface model with adaptive meshing developed for interfacial flows of complex fluids [46]. The algorithm has two major ingredients: a finite-element flow solver and an adaptive meshing scheme. The former is based on a Navier-Stokes solver that Hu and coworkers [67, 68] have used for simulating particle motion in Newtonian and viscoelastic fluids, while the latter is based on the mesh generator GRUMMP developed by Ollivier-Gooch [69]. Each ingredient has been generalized and adapted for the current purpose and then integrated. A brief description of each is given below.

The discretization of the governing equations follows the standard Galerkin formalism [67]. However, the Cahn-Hilliard equation requires special attention. With C^0 elements, which are smooth within each element and continuous across their boundaries, one cannot represent spatial derivatives of higher order than 2. Thus the fourth-order Cahn-Hilliard equation has been decomposed into two second-order equations:

$$\frac{\partial \phi}{\partial t} + \boldsymbol{v} \cdot \nabla \phi = \frac{\gamma \lambda}{\epsilon^2} \Delta (\psi_1 + s\phi) \tag{2.13}$$

$$\psi_1 = -\epsilon^2 \Delta\phi + (\phi^2 - 1 - s)\phi, \tag{2.14}$$

where s is a positive number that enhances the convergence of the iterative solution of the final linear system (see below). For all the calculations in this paper, $s = 0.5$ is used. The chemical potential G in Eq. (2.8) is now simply $G = \frac{\lambda}{\epsilon^2}(\psi_1 + s\phi)$.

On an unstructured triangular mesh, we have used piecewise quadratic (P2) elements for $\boldsymbol{v}$, ϕ and ψ_1, and piecewise linear (P1) elements for p and $\boldsymbol{\tau_d}$. After spatial discretization of the weak form of the governing equations, the nonlinear algebraic system can be written in the following general form:

$$\boldsymbol{\Lambda} \cdot \left(\frac{\partial \boldsymbol{U}}{\partial t}\right)^{n+1} + \boldsymbol{F}(\boldsymbol{U^{n+1}}) = 0, \tag{2.15}$$

where $\boldsymbol{U}$ is the solution vector, known at time step n and unknown at the next step $n+1$, $\boldsymbol{\Lambda}$ is a diagonal matrix with 1 or 0 on the diagonal depending on whether the corresponding $\boldsymbol{U}$ component appears in a time derivative, and $\boldsymbol{F}(\boldsymbol{U})$ contains all the other terms. For temporal discretization, we have used the Crank-Nicholson scheme and the 3-point backward difference scheme [67], and these second-order implicit schemes give nearly identical results. Equation (2.15) is solved using an inexact Newton's method with backtracking [70] for enhanced convergence and stability. To save computational cost, the Jacobian matrix is updated once in several iterations. Within each Newton iteration, the sparse linear system is solved by preconditioned Krylov methods such as the Generalized Minimum Residual (GMRES) method and the Biconjugate Gradient Stabilized (BCGSTAB) method. ILU(0) and ILU(t) preconditioners are found to be robust for the calculations in this paper. By design, our grid size varies greatly from the interface to the bulk. This gives rise to a highly ill-conditioned sparse matrix, which is treated by a scaling procedure whereby a diagonal scaling matrix is left-multiplied to the mass matrix prior to applying the aforementioned preconditioners. Thus, each row of the matrix is scaled by the inverse of the sum of the absolute values of the entries in that row before the linear system is sent to the preconditioned Krylov solvers.

The second key component of AMPHI is an adaptive mesh generator. We need a mesh with dense grids covering the interfacial region and coarser grids in the bulk. As the interface moves out of the fine mesh, the mesh in front needs to be refined while that left behind

needs to be coarsened. Such adaptive meshing is achieved by using a general-purpose mesh generator GRUMMP, which stands for Generation and Refinement of Unstructured Mixed-Element Meshes in Parallel [69]. GRUMMP produces triangular elements in 2D by using Delaunay refinement, and controls the spatial variation of grid size using a length scale L_S, which specifies the intended grid size at each location in the domain. In our work, the grid size distribution is dictated by the need to resolve thin interfaces. Since the phase-field variable ϕ is constant (± 1) in the bulk but varies steeply across the interface, we can impose a prescribed small grid size h_1 on the interface by making L_S depend on $|\nabla\phi|$ on every nodes:

$$L_S(x,y) = \frac{1}{|\nabla\phi|\frac{\sqrt{2}}{C} + \frac{1}{h_\infty}} \tag{2.16}$$

where h_∞ is the mesh size in the bulk, and the constant C controls the mesh size in the interfacial region: $h_1 = L_S|_{\phi=0} \approx C \cdot \epsilon$, ϵ being the capillary width. In this paper, we have used C values between 0.5 and 1; $h_1 \leq \epsilon$ ensures that the thickness of the interface typically contains on the order of 10 grid points [34]. Furthermore, the length scale h_∞ can be set to differing values h_2 and h_3 in the two bulk fluids. This will allow, for example, the interior of a drop to be more finely resolved than the far field of the suspending fluid. Of course, the benchmarks h_1, h_2 and h_3 are guidelines that most of the elements satisfy approximately but not exactly. A grading factor $G_1 \sim 5$ is found to produce generally satisfactory transitions among different regions of the mesh.

More details of the numerical method can be found in Yue *et al.* [46,66], who also reported detailed parametric studies and validation with benchmark problems. Our simulations follow the recommendation in these studies in terms of numerical parameters and mesh size, and adequate spatial and temporal resolution is ensured for the simulations presented in this chapter. Specifically, the Cahn number is fixed at $Cn = \frac{\epsilon}{a} = 0.01$. The mesh sizes are as follow: $h_1 = 0.01a$, $h_2 = 0.3a$ and $h_3 = 0.1a$. Mesh refinement studies, on drop deformation in simple shear and extensional flows, have shown that this mesh resolution controls the discretization errors to within 1% of the results.

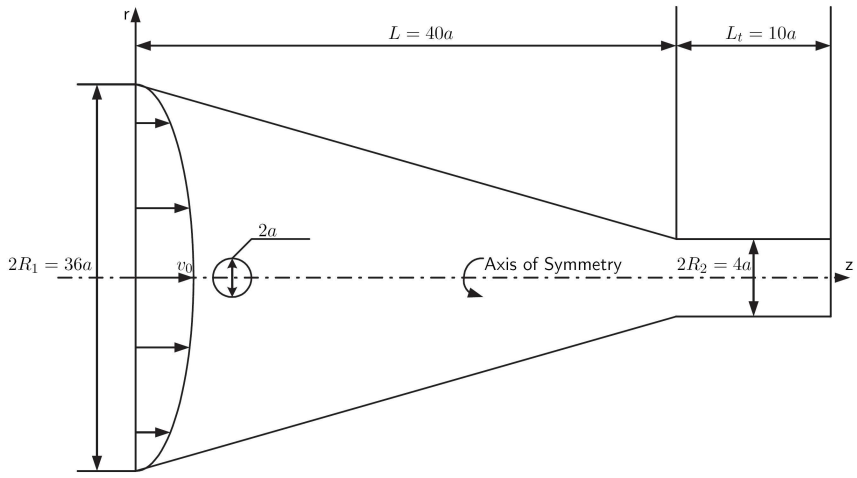

Figure 2.1: Schematic of the flow geometry, with the computational domain being half of the meridian plane. Not drawn to scale.

2.4 Problem setup

Figure 2.1 depicts the axisymmetric geometry of the converging flow channel. The computational domain is the upper half of the meridian plane. On the upstream boundary, we specify a parabolic profile for the axial velocity v_z with a centerline velocity v_0 and zero radial velocity v_r. If the matrix fluid is viscoelastic, we also impose fully developed polymer stresses at the entrance. Fully developed entrance conditions are not exactly correct in our geometry, even if it is preceded by a long straight section upstream. They are used here for simplicity, and numerical experiments show that the drop deformation in the conical section is not sensitive to the entry condition. For example, imposing the steady velocity and stress profiles at the beginning of the contraction that have been computed with a long straight section upstream will produce a 3% difference in drop deformation. Along the centerline, we assume conditions of symmetry with $\frac{\partial}{\partial r} = 0$ for all velocity and stress components except $v_r = 0$. At the exit, natural boundary conditions are used. Initially, a spherical drop of radius a is placed at $z_0 = 5a$ on the centerline in a quiescent matrix; the initial velocity and stress fields are zero. At time $t = 0$, the inflow velocity profile is activated and the flow starts throughout the domain. The drop elongates while moving down the centerline of the pipe.

Upon non-dimensionalizing the governing equations and boundary conditions, the following 6 dimensionless groups emerge (in addition to the Giesekus mobility α and the 4 length ratios indicated in Fig. 2.1):

$$\omega = \frac{\rho_d}{\rho_m} \quad \text{(drop-to-matrix density ratio)}, \tag{2.17}$$

$$\beta = \frac{\mu_d}{\mu_m} \quad \text{(drop-to-matrix viscosity ratio)}, \tag{2.18}$$

$$k = \frac{\mu_s}{\mu_s + \mu_p} \quad \text{(solvent viscosity ratio in Giesekus fluid)}, \tag{2.19}$$

$$Ca = \frac{\mu_m a \bar{\dot{\epsilon}}}{\sigma} \quad \text{(capillary number)}, \tag{2.20}$$

$$Re = \frac{\rho_m v_0 a}{\mu_m} \quad \text{(Reynolds number)}, \tag{2.21}$$

$$De = \bar{\dot{\epsilon}} \lambda_H \quad \text{(Deborah number)}, \tag{2.22}$$

where the subscripts d and m denote the drop and matrix components. For the viscoelastic fluid, the total zero-shear viscosity $\mu_s + \mu_p$ is used in computing β, be it in the drop or the matrix. Since the strain rate varies along the centerline, we have used an averaged strain rate $\bar{\dot{\epsilon}}$ in defining the capillary and Deborah numbers. Assuming that the centerline velocity varies according to the inverse of the cross-sectional area, the total Hencky strain from $z = 0$ to $z = L$ is $2 \ln \frac{R_1}{R_2}$ and the total transit time is

$$t_{tr} = \int_0^L \frac{dz}{v_z} = \frac{L}{3v_0} \frac{R_1^2 + R_1 R_2 + R_2^2}{R_1^2}. \tag{2.23}$$

We define the average strain rate $\bar{\dot{\epsilon}}$ as the ratio between these two quantities.

Several parameters are fixed throughout the simulations. The drop-to-matrix density ratio is kept at $\omega = 1$, and the Reynolds number remains at $Re = 0.01$. Depending on the viscosity ratio, the Re based on drop viscosity could be as large as 1. But in all cases, inertia plays at most a marginal role. All the length ratios are fixed at their values in Fig. 2.1. To avoid the stress blowup in the Oldroyd-B model but to produce sufficiently large viscoelastic stresses, we have used a small $\alpha = 0.03$ for all the simulations. The polymer relaxation time is varied over a wide range to capture a comprehensive picture of the viscoelastic effect. Thus, the value of rheological parameters is based more on the need to reveal interesting physics than to approximate specific fluids. The discussion in the next section will focus on the effects of Ca, β and De on drop deformation.

2.5 Numerical Results

To explore the drop deformation in a converging pipe flow, we have done three groups of simulations: a Newtonian drop in a Newtonian matrix as the baseline, a Giesekus drop in a Newtonian matrix, and a Newtonian drop in a Giesekus matrix.

In the literature, drop deformation has been represented by two length ratios: $\frac{l-b}{l+b}$ and $\frac{l}{a}$, l and b being the half-length and half-breadth of the drop. The first is sensitive to small departures from sphericity, while the second is more suitable for highly elongated drops [71, 72]. We will use $D = \frac{l}{a}$ in this paper since the drop deformation may be quite large.

When the rheology of either the drop or the matrix changes, the drop speed and displacement will vary. Thus, it is awkward to compare D based on the same time or the same drop position on the centerline. Following Mighri *et al.* [53], we use the matrix strain *in the absence of the drop* as the benchmark for comparing drop deformation. From the local strain rate $\dot{\epsilon} = \frac{dv_z}{dz}$ on the centerline, the matrix Hencky strain ϵ_m can be calculated. The corresponding matrix stretch ratio $D_m = \exp(\epsilon_m)$ turns out to be

$$D_m(z) = \frac{v_z(z)}{v_z(z_0)}, \tag{2.24}$$

where $z_0 = 5a$ is the initial position of the drop. Thus, $D_m(z)$ is the deformation of a matrix fluid particle currently at z with respect to its initial configuration at z_0, where the undeformed drop sits initially. Drop deformation D will be examined vis-à-vis the matrix deformation D_m at the same z as the drop's centroid on the centerline of the converging pipe.

2.5.1 A Newtonian drop in a Newtonian matrix

In our geometry, the drop experiences a spatially inhomogeneous and temporally transient extensional flow as it moves along the centerline of the converging pipe. As a result of this, the drop deformation is always in a transient state and the velocity of interface is not zero. Figure 2.2 depicts the kinematics of the flow around the drop. The streamlines, in a reference frame fixed on the centroid of the drop, resemble those of an elongational flow

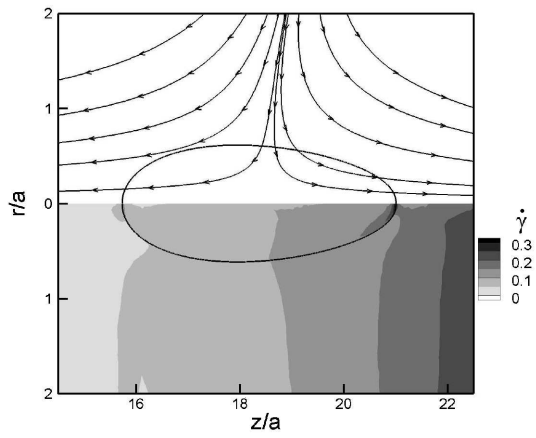

Figure 2.2: A snapshot of the flow field around the drop when $D_m = 2.5$ and the drop centroid is near $z = 18a$. $Ca = 2.9$, $\beta = 0.5$. The top half shows streamlines in a reference frame fixed on the centroid of the drop, while the bottom half shows contours of the strain rate $\dot{\gamma}$, the second invariant of the strain rate tensor. For a clearer view of the drop interior, we have magnified the r coordinate relative to z.

but exhibits a fore-aft asymmetry. Consequently, the drop is asymmetric as well, being more elongated in the front. The contours of the strain rate exhibit a general increase downstream. But within the drop, $\dot{\gamma}$ achieves a maximum at the front tip.

Figure 2.3 depicts the deformation of a Newtonian drop in a Newtonian matrix for several viscosity ratios. Comparing the $D(z)$ and $D_m(z)$ profiles in Fig. 2.3(a), we note that for the relatively high capillary number $Ca = 2.9$, the drop deforms more than the matrix if it is less viscous ($\beta = 0.01$) and vice versa ($\beta = 2$), in agreement with experimental observations [73]. For D_m, we also plot a curve based on the exact Stokes flow solution in an infinite cone [4]. The actual stretching ratio turns out to be rather higher than the analytical solution, thanks to the inlet and outlet conditions.

Figure 2.3(b) plots the drop deformation D as a function of the matrix deformation D_m for five β values. All curves have an initial transient, obviously due to the somewhat artificial initial condition, but eventually assume a constant slope. This linearity has been observed experimentally by Mighri *et al.* [53]. In steady and homogeneous elongation, the steady-state deformation of a drop (for sub-critical Ca) is often viewed as the result of the balance between viscous and capillary forces. In our situation, the strain rate in the matrix continues to increase as the drop moves downstream (cf. Fig. 2.3a), as does the viscous force. Thus,

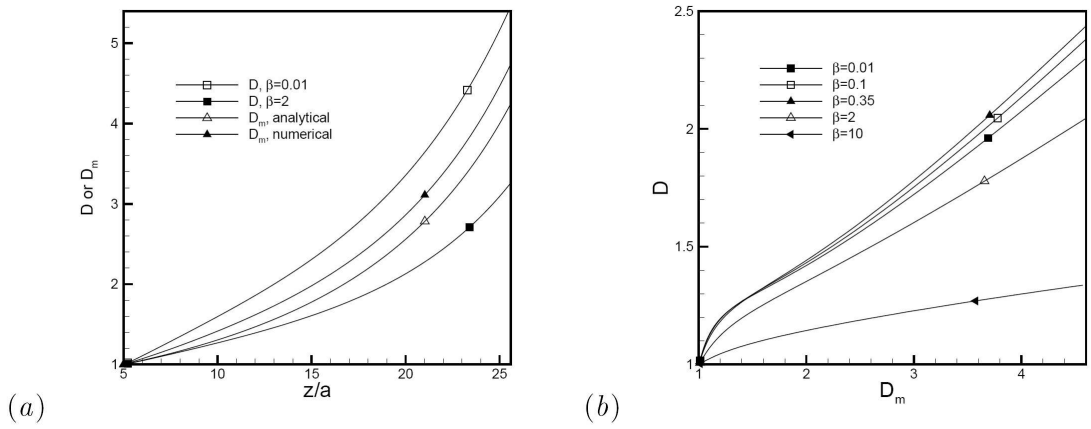

(a) (b)

Figure 2.3: (a) Drop and matrix deformation as functions of the position z for Newtonian systems at $Ca = 2.9$. For the drop deformation D, two viscosity ratios are shown. For the matrix deformation D_m, an analytical result based on creeping flow in an infinite cone is also shown for comparison [4]. (b) Drop deformation D as a function of the matrix deformation D_m for Newtonian systems at $Ca = 0.29$.

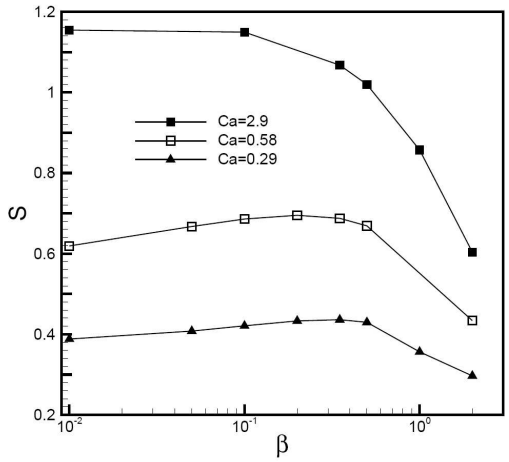

Figure 2.4: The slope of drop deformation S as a function of viscosity ratio β in Newtonian systems at different Ca.

the drop deformation increases continuously. For the rest of the paper, we will use the slope S of the straight portion of the $D(D_m)$ curves to indicate the speed of drop deformation. For Newtonian systems, S will be shown to depend on Ca and β, while for non-Newtonian fluids, the Deborah number De is involved as well.

A curious observation in Fig. 2.3(b) is that for this Ca the drop deformation does not seem to depend on the viscosity ratio β monotonically. This effect is more clearly illustrated in Fig. 2.4 in terms of the slope S. For smaller Ca, there is a intermediate viscosity ratio β_M at which the drop deforms the fastest. With Ca increasing from 0.29 to 1.45, β_M decreases from approximately 0.35 to 0.20, and seems to disappear for larger Ca.

The non-monotonic dependence of S on β can be explained by the transient deformation of a drop after the startup of an elongational flow at a fixed strain rate. Numerical computations by Hooper *et al.* [42] show that a more viscous drop reacts to the startup more slowly; its initial deformation lags behind that of a less viscous drop. However, it eventually achieves a greater steady-state deformation, provided that Ca is below the critical value for drop burst. The slower initial reaction is due to a longer "emulsion time" $t_{em} = \frac{\mu_d a}{\sigma}$ for the drop [74], and the greater steady-state deformation is because the more viscous interior sustains higher internal stresses so as to afford the exterior fluid a firmer "grip" on the interface. In our geometry, the drop experiences an unsteady external flow in the Lagrangian sense. So it deforms continually and is in a perpetual transient state. For small β values, t_{em} is short and the drop is close to equilibrating with the local strain rate. Thus, it exhibits the *steady-like* behavior with the instantaneous $D(t)$ increasing with β. For large β values, the contrary is true and the drop is dominated by the *transient* response, with $D(t)$ decreasing with β. This explains the non-monotonic $S(\beta)$ curves in Fig. 2.4 for smaller Ca. Larger Ca may be thought of as the result of increased flow rate or decreased interfacial tension. Either way, a drop would take longer dimensional time to reach steady state upon startup of the uniform elongation. In our geometry, therefore, the transient response prevails and D decreases with β monotonically. This monotonic decrease confirms previous computations in the limit of $Ca \to \infty$ [51].

2.5.2 A Giesekus drop in a Newtonian matrix

Figure 2.5 depicts the deformation of viscoelastic Giesekus drops as a function of the local matrix deformation for several capillary and Deborah numbers. Similar to the Newtonian drops in Fig. 2.3, the viscoelastic drop attains a "linear regime" of deformation after an initial transient. This is consistent with the observations of Mighri *et al.* [53]. Thus, the

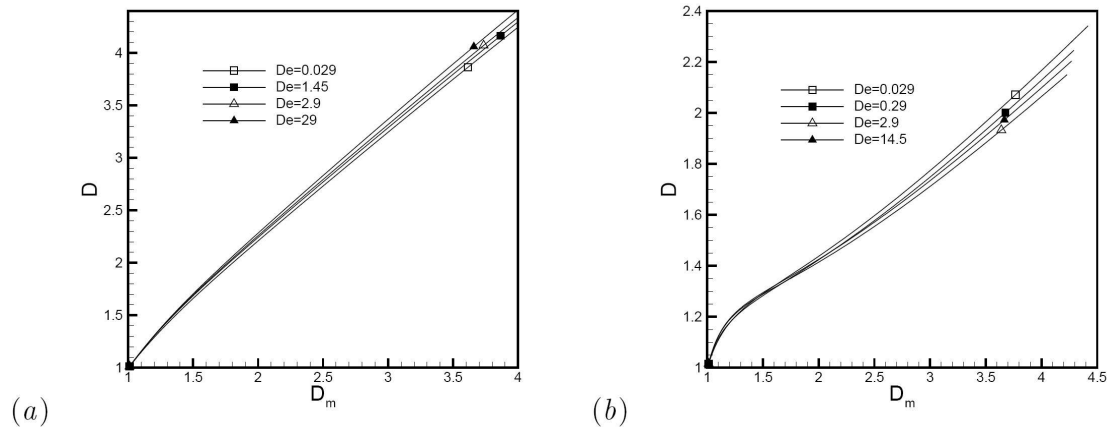

Figure 2.5: Deformation of Giesekus drops as a function of the Newtonian matrix deformation with $\beta = 0.5$ and $k = 0.2$. (a) $Ca = 2.9$; (b) $Ca = 0.29$. Although the differences among the curves are small in magnitude, they are much greater than discretization errors and represent a real physical effect.

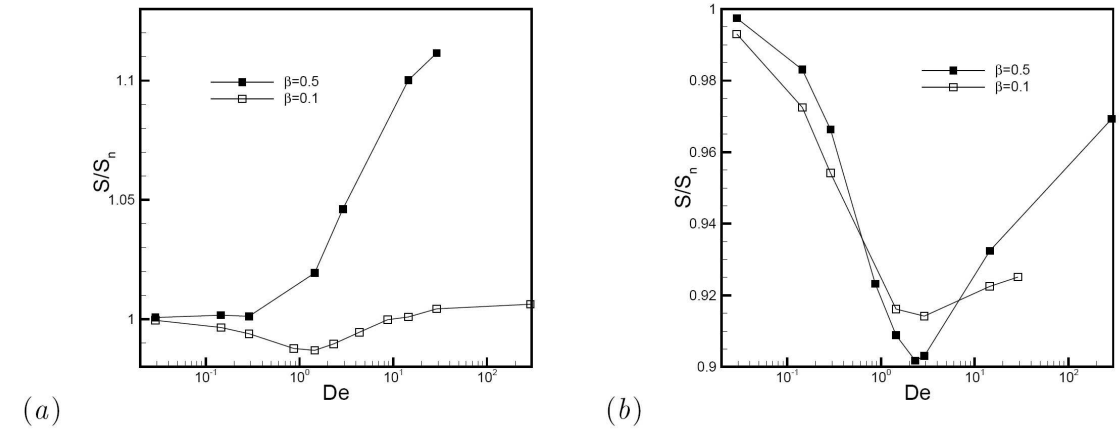

Figure 2.6: Viscoelastic effects on the deformation of a Giesekus drop in a Newtonian matrix at (a) $Ca = 2.9$, (b) $Ca = 0.29$. The drop deformation is represented by the slope S scaled by the corresponding Newtonian slope S_n, and exhibits different trends with varying Deborah number De. For all cases, the Giesekus fluid has a solvent viscosity ratio $k = 0.2$.

drop deformation may be analyzed in terms of the slope S as before, but now as a function of the Deborah number De.

Figure 2.6 shows four $S(De)$ curves for different Ca and β values. For $\beta = 0.5$, two different behaviors are manifested for large and small Ca. For highly deformed drops at $Ca = 2.9$, viscoelasticity promotes drop deformation. That is, the polymeric drop deforms faster than

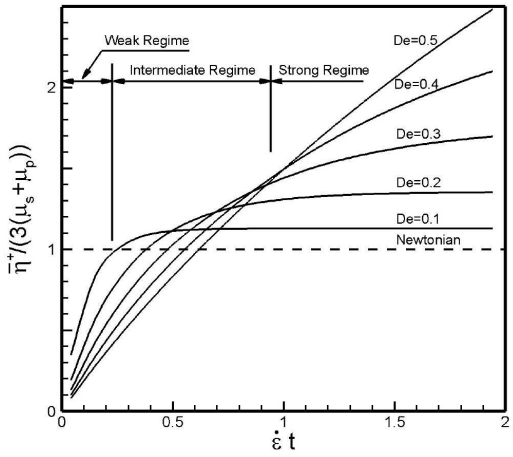

Figure 2.7: Stress growth predicted by Giesekus model after startup of uniaxial elongation. The elongational viscosity $\bar{\eta}^+$ is scaled by that of a Newtonian fluid with the same zero-shear viscosity $\mu_s + \mu_p$, the Deborah number is $De = \dot{\epsilon}\lambda_H$ and time is scaled by $1/\dot{\epsilon}$.

the Newtonian drop, and the difference increases monotonically with De. For moderately deformed drops at the lower $Ca = 0.29$, the viscoelastic effect is non-monotonic; S first decreases with De, reaches a minimum around $De = 2$ and then increases. At the largest De computed, the drop deformation is still below that of the Newtonian drop. For $\beta = 0.1$, the non-monotonic behavior is seen for both Ca values.

The differing trends can be explained in terms of the "effective viscosity" of the non-Newtonian drop. The polymer stress takes a finite time ($\sim \lambda_H$) to react to flow, and as the simplest example, Fig. 2.7 shows the stress growth curves for a Giesekus fluid after startup of a homogeneous elongation at a constant strain rate $\dot{\epsilon}$. For short times, the polymer viscosity is smaller than its Newtonian counterpart, and indeed it decreases with De. This may be called the "weak regime" where the polymer molecules do not have time to unravel and sustain stress. For long times, the polymer stress eventually outgrows the Newtonian value, and in this "strong regime", $\bar{\eta}^+$ increases with De. The longer the polymer relaxation time, the longer the weak regime persists. Note that these so-called regimes are rather loosely defined; they refer to how $\bar{\eta}^+$ varies with De within a *certain time interval* and a *certain range of* De.

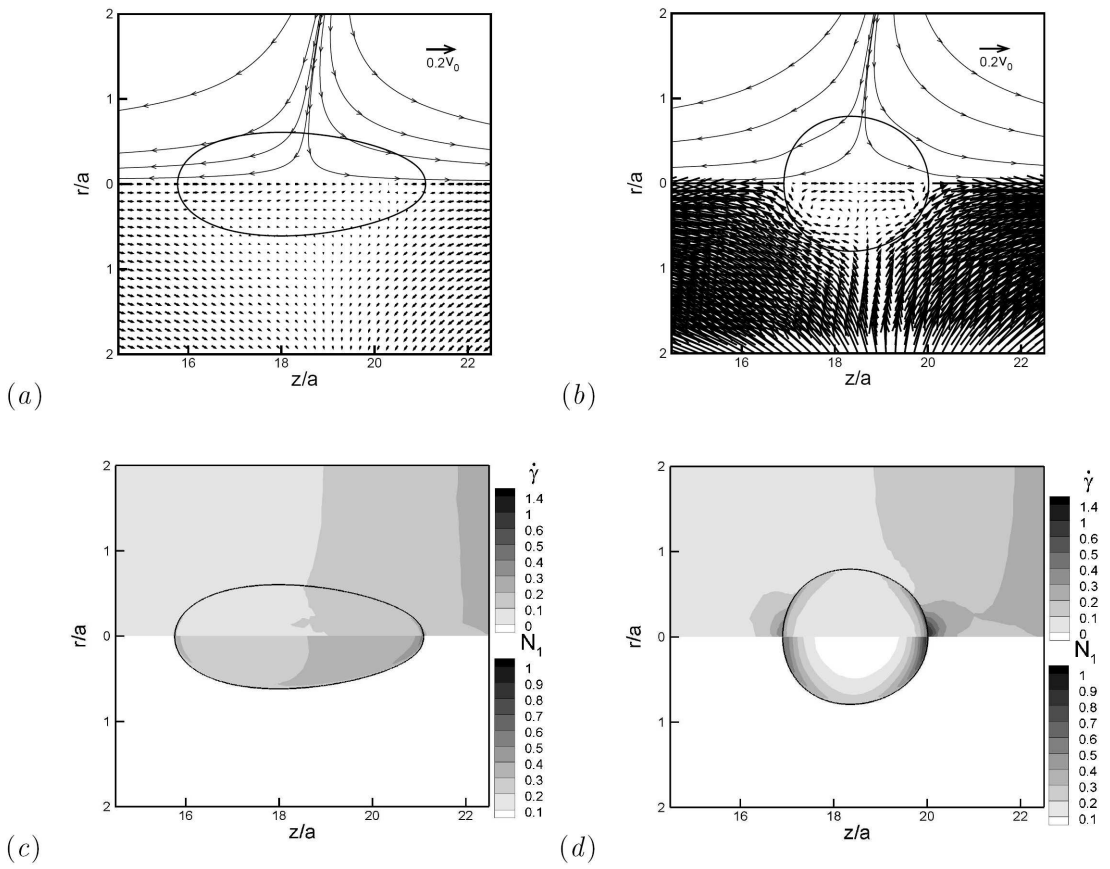

Figure 2.8: Snapshots of the flow and stress fields near the Giesekus drop when $D_m = 2.5$. $\beta = 0.5$ and $k = 0.2$. (a) $Ca = 2.9$. The top shows streamlines in the reference frame of the drops's centroid, while the bottom plots the velocity vector field $\boldsymbol{v} - S\boldsymbol{v}_m$ (see text). (b) The same plots for $Ca = 0.29$. The reference vector in (a) and (b) is $0.2v_0$. (c) $Ca = 2.9$. The top and bottom respectively plot contours of the strain rate $\dot{\gamma}$ and the normal stress difference N_1. (d) The same plots for $Ca = 0.29$.

Our simulations are complicated by two additional factors. First, the flow inside the drop is not uniformly elongational but comprises regions of varying flow type and strain rate. Second, the Lagrangian unsteadiness experienced by the drop imposes a more complex deformation history than sudden startup. However, the main idea of Fig. 2.7 carries over: depending on how fast the polymer stress develops, the drop may have an effective viscosity that is lower or higher than its Newtonian counterpart, which would make it deform faster or slower. In the following, we will first analyze two such scenarios for $\beta = 0.5$ and $Ca = 0.29$ and 2.9.

In both cases, the streamlines (top of Fig. 2.8*a* and *b*) have the same asymmetric hyperbolic pattern. However, the contours of the strain rate differ (top of Fig. 2.8*c* and *d*). In the highly elongated drop at $Ca = 2.9$, $\dot{\gamma}$ is fairly uniform inside the drop, with a weak maximum near the front tip. In the less deformed drop at $Ca = 0.29$, $\dot{\gamma}$ is small in the middle of the drop but attains relatively large magnitudes near the front and the back, with a maximum at the front tip. Contours of the normal stress $N_1 = \tau_{zz} - \tau_{rr}$ in the bottom halves of Fig. 2.8(c) and (d) show similar patterns.

To explain this difference, it is convenient to think of the straining inside the drop as from two possible origins: primary flow due to elongation of the drop and secondary flow (e.g., recirculating eddies) due to confinement of the interface. For a drop that deforms affinely with the matrix, the internal straining is entirely due to the first. For a drop that has attained steady shape in an elongational flow, it is entirely due to the second. As our drop stretches at a rate that is S times that of the matrix, we may take $S\boldsymbol{v}_m$ to be the primary flow inside the drop, $\boldsymbol{v}_m$ being the "background" velocity of the matrix in the absence of the drop. Then the remainder $\boldsymbol{v} - S\boldsymbol{v}_m$ represents the secondary flow. For $Ca = 2.9$, the drop elongates almost affinely as $S \approx 1$ in Fig. 2.5(a). Thus, the flow field inside the drop is as if the interface did not exist, and the secondary flow due to the interface, plotted in the bottom of Fig. 2.8*a*, is almost nil. For $Ca = 0.29$, in contrast, the drop deforms much more slowly than the matrix (cf. Fig. 2.5*b*). The secondary flow exhibits the familiar recirculating eddies in the bottom of Fig. 2.8(b). This pattern produces strong uniaxial extension and long residence times near the front and back stagnation points and consequently the $\dot{\gamma}$ and N_1 contours in Fig. 2.8(c) and (d), in much the same way as inside a drop that has reached steady-state deformation in steady uniaxial elongation [41].

The above analysis has two implications to interpreting the viscoelastic effects on drop deformation. First, since the bulk of the drop experiences much lower stress than the maximum N_1 at the front, it is reasonable to use this maximum N_1^{max} as an indication of the drop's internal stress and hence its resistance to deformation. Second, the magnitude of $\dot{\gamma}$ in Fig. 2.8 possibly puts the $Ca = 0.29$ case (with an average strain rate $\dot{\gamma}_{av} = 0.045$) in the strong regime of Fig. 2.7 but $Ca = 2.9$ ($\dot{\gamma}_{av} = 0.09$) in the weak regime, with different dependence on the Deborah number.

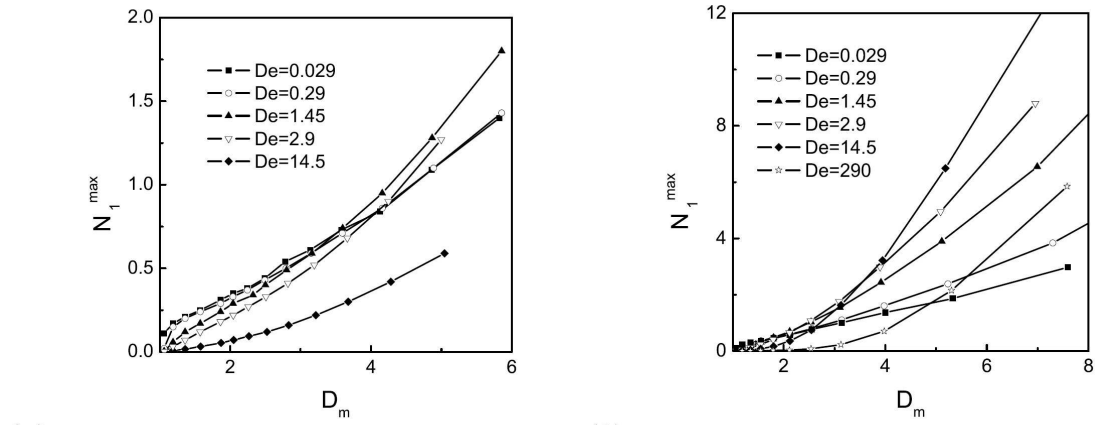

(a) (b)

Figure 2.9: History of stress growth at the front tip of the Giesekus drop for a range of De. (a) $Ca = 2.9$; (b) $Ca = 0.29$. For all curves $\beta = 0.5$ and $k = 0.2$.

This is confirmed by comparing the history of stress growth at the front tip of the drop for a range of De (Fig. 2.9). For $Ca = 0.29$, the maximum stress N_1^{max} increases as De increases from 0.029 to 2.9. This is the *strong-regime* behavior, with the effective viscosity of the drop increasing with De. Referring to Fig. 2.4, a zero-shear viscosity ratio of $\beta = 0.5$ means that we are in the range where drop deformation decreases with drop viscosity. Thus, D decreases with De in this range in Fig. 2.6(b). As De increases further to 14.5 and 290, the polymer stress grows more slowly, and N_1^{max} starts to decrease with De for the initial part of the drop's trajectory. This explains the subsequent increase of D with De in Fig. 2.6(b). The non-monotonic dependence of D on De for $Ca = 0.29$, therefore, reflects the polymer stress inside the drop undergoing a transition from the strong to the weak regime. This is essentially the *intermediate regime* in Fig. 2.7 in which the elongational viscosity at a fixed time first increases with De and then declines. In contrast, the polymer stress for $Ca = 2.9$ remains mostly in the weak regime because the strain rate $\dot{\gamma}$ is lower in the drop and the stress grows more slowly. This is evident in Fig. 2.9(a) and explains the monotonic increase of D with De in Fig. 2.6(a).

We have performed the same analysis on the two curves in Fig. 2.6 for $\beta = 0.1$. The quantitative difference is that $\dot{\gamma}$ inside the drop is now higher. This is easy to understand since with decreasing drop viscosity, the interfacial mobility increases. The larger $\dot{\gamma}$ amounts

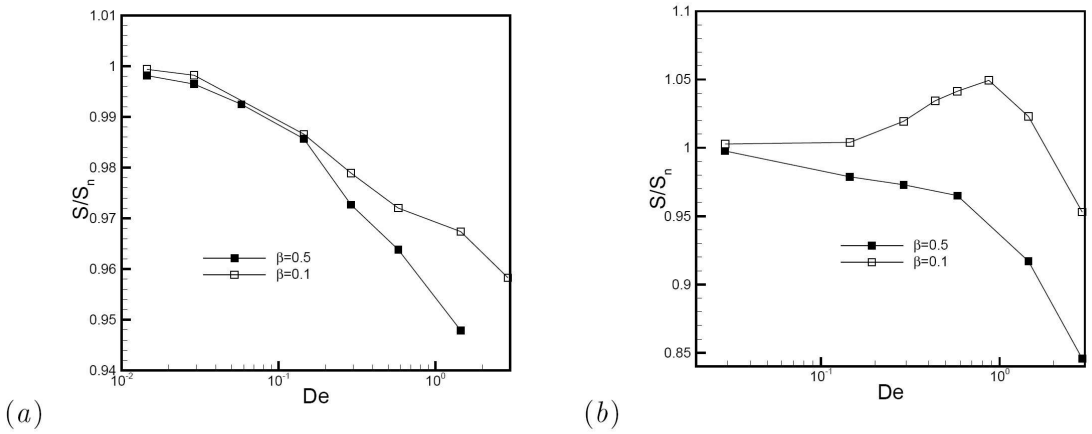

Figure 2.10: Viscoelastic effects on the deformation of a Newtonian drop in a Giesekus matrix at (a) $Ca = 2.9$, (b) $Ca = 0.29$. The drop deformation is represented by the slope S scaled by the corresponding Newtonian slope S_n. For all cases, $k = 0.7$.

to shifting the dimensionless time in Fig. 2.7 to the right, thereby the weak regime for $\beta = 0.5$ to the intermediate regime for $\beta = 0.1$ in Fig. 2.6(a). Conceivably, the drop will still exhibit entirely weak behavior (S increasing monotonically with De) at sufficiently large Ca.

To summarize, the viscoelastic effect on drop deformation is rooted in the polymer stress in the drop, but manifested through a sort of "spatial integration" over extensional and rotational regions inside the drop as well as a "temporal integration" over the Lagrangian-unsteady trajectory of the drop. As in the simple picture of Fig. 2.7, here the polymer stress grows according to the polymer relaxation time and the local strain rate. Thus one may be tempted to relate the polymer stress to a local Deborah number. But we did not attempt to identify the local instantaneous $\dot{\gamma}$ and De to force a quantitative connection with the weak and strong regimes in Fig. 2.7. This is because the spatial and temporal variations make it impossible to define an effective De for the entire drop and pinpoint the time for the transition from the weak to the intermediate regime. The connection between Fig. 2.7 and Fig. 2.6 is subtler than can be thus quantified.

2.5.3 Newtonian drops in Giesekus matrix

Deformation of Newtonian drops in a Giesekus matrix also displays the linear growth with matrix deformation after an initial transient, similar to the inverse case of the last subsection

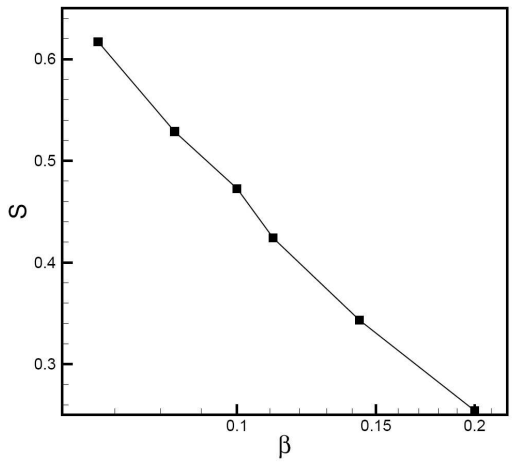

Figure 2.11: The slope S as a function of the viscosity ratio β for a Newtonian drop in a Newtonian matrix with the capillary number based on the drop viscosity fixed at $Ca_d = 0.029$.

(Fig. 2.3). This is again in agreement with the experimental observations of Mighri *et al.* [53]. Thus, we continue to use the slope S of the growth curve as a yardstick to measure the effect of matrix viscoelasticity on drop deformation. Figure 2.10 plots the variation of S with the Deborah number De for two capillary numbers and two viscosity ratios. For $\beta = 0.5$, drop deformation is seen to decrease monotonically with De for both Ca. For $\beta = 0.1$, however, two different behaviors may appear. For $Ca = 0.29$, S first increases with De, peaks around $De = 0.9$ and then decreases for higher De to values below the Newtonian deformation. For $Ca = 2.9$, S declines monotonically with increasing De.

The two trends can be explained in terms of the transient polymer stress in a similar fashion to the last subsection. A minor complication is that in the Newtonian curves of Fig. 2.3, Ca is defined using the matrix viscosity μ_m. While changing the drop viscosity μ_d only affects β, changing μ_m would change the capillary number as well, and the resultant change in D or S cannot be read directly off Fig. 2.4. If we define a capillary number Ca_d using μ_d, then the effect of changing μ_m (and thus β) with Ca_d fixed is very simple: the drop deformation decreases with β for all values of Ca_d tested. An example is shown in Fig. 2.11 for $Ca_d = 0.029$. There is no longer the interplay between initial transient and final steady state seen in Fig. 2.3. Based on Fig. 2.11, the effect of matrix viscoelasticity can be easily

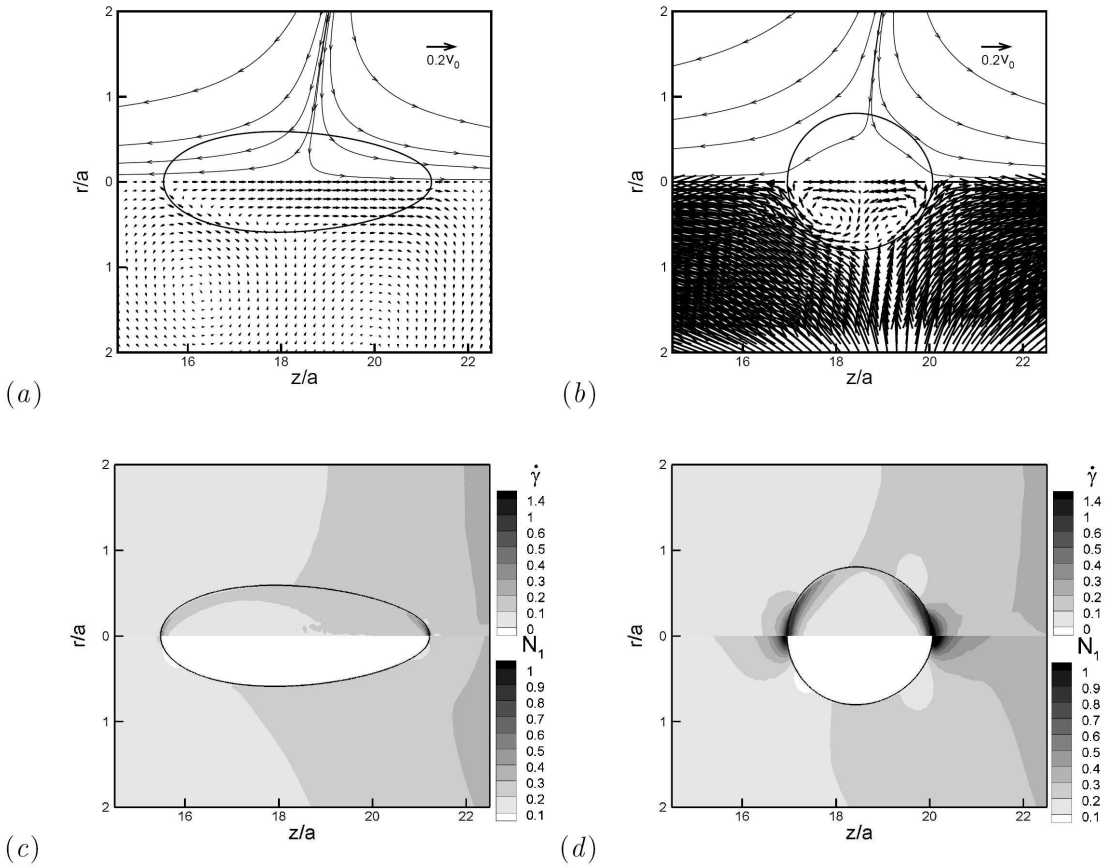

Figure 2.12: Flow and stress fields near a Newtonian drop in a Giesekus matrix at $D_m = 2.5$. $\beta = 0.1$, $k = 0.7$. The streamlines, velocity vectors and contours for $\dot{\gamma}$ and N_1 are plotted in the same way as in Fig. 2.8. $Ca = 2.9$ for (a) and (c) and $Ca = 0.29$ for (b) and (d). The reference vector in (a) and (b) is for the velocity vector plots.

interpreted through the idea that the growing polymer stress amounts to a changing effective viscosity for the matrix.

We will first explain the differing trends seen for $\beta = 0.1$. The flow and stress fields near the drop, plotted in Fig. 2.12, show a certain similarity to those in the last subsection. Our focus, of course, now falls on the Giesekus matrix fluid surrounding the drop. Note that for the less deformed drop at $Ca = 0.29$, $\dot{\gamma}$ and N_1 are much larger than the drop at $Ca = 2.9$, and their maxima occur just outside the front tip of the drop. Therefore, the drop at $Ca = 0.29$ may experience the *strong regime* while the latter the *weak regime*. This is borne out by the stress growth curves for a range of De at each Ca (Fig. 2.13).

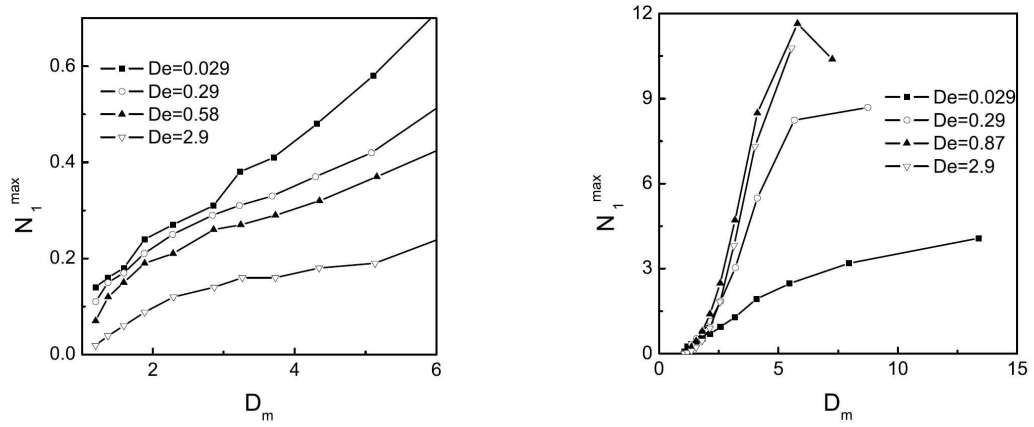

(a) (b)

Figure 2.13: History of stress growth outside the front tip of the Newtonian drop in the Giesekus matrix for a range of De. (a) $Ca = 2.9$; (b) $Ca = 0.29$. $\beta = 0.1$ and $k = 0.7$ for all curves.

For $Ca = 2.9$, the polymer stress decreases monotonically with De, showing weak regime behavior. For $Ca = 0.29$, on the other hand, N_1 increases with De until $De = 0.87$, and then declines with greater De. There is a transition from the strong regime for smaller De to the weak regime for larger ones. If the polymer stress amounts to, in an average sense, an effective viscosity of the viscoelastic matrix, then in view of Fig. 2.11, we can rationalize the monotonic decrease of S with D in Fig. 2.10(a) and the non-monotonic variation in Fig. 2.10(b).

For $\beta = 0.5$, the strain rates and polymer stresses are both lower, since the higher drop viscosity reduces the interfacial mobility. Qualitatively this corresponds to shifting the dimensionless time in Fig. 2.7 to smaller times. Consequently the weak regime prevails for both Ca values. We omit a detailed analysis for brevity.

Based on the analysis of the last two subsections, the commonality between Fig. 2.6 and Fig. 2.10 becomes apparent. No matter whether the viscoelasticity occurs in the drop or the matrix, its effect on drop deformation may fall in the weak regime or the intermediate regime (i.e., the transition from the strong to the weak regime). The key determinant is the magnitude of $\dot{\gamma}$ inside the viscoelastic component relative to the externally imposed strain rate. A smaller Ca or β causes a higher $\dot{\gamma}$ and favors the strong regime. Generally, we may expect the De range corresponding to the strong regime to widen for decreasing Ca and/or β, and to narrow and even disappear for increasing Ca and/or β.

2.6 Comparison with prior studies

The results reported in the last section may seem inconsistent with the conventional thinking that polymer in the drop reduces its deformation while polymer in the matrix increases deformation. That notion is based on the heuristic argument that the *steady-state* drop shape is the result of a balance among the hydrodynamic forces inside and outside the drop and the interfacial tension [49]. In steady uniform elongational flows, the predictions are indeed confirmed by experiments and calculations [40–42, 72]. The converging flow geometry produces a continuously increasing strain rate along the centerline, which keeps the polymer stress, be it in the drop or the matrix, in a perpetual transient. As a result, the drop deformation exhibits a more varied behavior than in steady elongational flow.

The experiment of Mighri *et al.* [53] and the computation of Khayat [54] provide the most comprehensive data in the literature on drop deformation in a conical flow geometry. Mighri *et al.* reported a linear relationship between drop deformation D and matrix deformation D_m for all Newtonian and Boger-fluid drops and matrices tested. Our predictions are consistent with these findings except that the linearity becomes established only after the influence of the initial condition dies out in the numerical simulations. For all their experimental runs, Mighri *et al.* found that viscoelasticity in the drop decreases drop deformation while that in the matrix increases it. These correspond to our strong-regime behavior. In contrast, Khayat's simulations, based on a linear Oldroyd-B model, predict purely weak-regime behavior; the drop deformation increases monotonically with De if the polymer is in the drop but decreases monotonically if in the matrix. The contradiction between these two studies can be reconciled by examining the flow and material parameters.

Using the material and experimental parameters of Mighri *et al.*'s experiment, we have determined the range of dimensionless groups as defined here: $9 \times 10^{-3} \leq Ca \leq 9 \times 10^{-2}$, $0.28 \leq \beta \leq 1.1$ and $4 \times 10^{-3} \leq De \leq 0.14$. Comparing these parameters with Fig. 2.6 and Fig. 2.10, it is reasonable to assume that the small Ca and small De have put all the experiments within the strong regime. Khayat [54] did not report the matrix viscosity used in his computations. If we take $\mu_m \sim 50$ Pa·s from the experiment of Bourry *et al.* [51], which Khayat [54] aimed to simulate, then Khayat's Ca is estimated to be around 800. The viscosity ratio is also relatively large: $\beta = 3$, and the Deborah number De ranges from 0.016

to 0.16. The large Ca and β imply that his simulations are well within the weak regime. Therefore, Mighri *et al.*'s experiment and Khayat's simulation fall on opposite ends of the parametric spectrum; the former is entirely in the strong regime while the latter in the weak regime.

The strong-regime behavior is more familiar because most prior experiments have measured *steady-state* drop deformation. The only exception may be the experiment of Delaby *et al.* [75], in which deformation of polymer inclusions in a polymer matrix is measured following startup of stretching. They reported that the drop deforms more (or less) than in a comparable Newtonian/Newtonian system if its relaxation time is longer (or shorter) than that of the matrix polymer. This trend corresponds to our weak regime. The authors invoked the linear viscoelastic theory of Palierne to explain the observations, even though the total strain is on the order of 5. A quantitative comparison with our calculations is difficult because the experiment employed uniform elongation. A further complication arises from the use of polymer melts, whose stretching may implicate both deformation-dependent viscosity and elasticity, and it is impossible to separate the two. Additional hints of weak-regime behavior come from the computational results of Hooper *et al.* [76]. In startup of uniaxial elongation at a fixed strain rate, viscoelasticity in the drop causes a faster initial drop deformation than a Newtonian drop of the same viscosity, and a Newtonian drop deforms more slowly in a viscoelastic matrix.

To verify the weak-regime drop deformation predicted here, experiments should be designed to have low strain rates but fast transients in the Lagrange sense, with polymers of long relaxation times. This way, the polymer stress is kept in an "undeveloped stage", far from equilibrating with the local instantaneous strain rate. In the past, the strong-regime picture was long held for shear flows as well [77, 78], until the careful low-strain-rate measurements of Guido *et al.* [79] suggested the existence of weak-regime deformation for small De. Computational confirmation came afterwards [45]. In inhomogeneous elongational flows, our predictions of weak and intermediate-regime drop deformation await similar experiments.

Finally, the idea of comparing the polymer relaxation time λ_H and the emulsion time t_{em} has proved useful in analyzing certain viscoelastic interfacial flows [25, 80]. For instance, Grillet *et al.* [25] found the so-called elasticity parameter $\frac{De}{Ca}$ an important determinant of interfacial instability in coating flows involving a viscoelastic liquid. The idea does not apply to our problem, however. A long t_{em} implies a long transient in drop deformation, and a long λ_H indicates slow growth of polymer stress. Both conspire, rather than compete, in bringing about weak-regime behavior.

2.7 Conclusion

In this study, we have investigated the influence of viscoelasticity on drop deformation in converging pipe flows in a conical geometry. Three series of simulations have been carried out, with Newtonian drops in a Newtonian matrix, Giesekus drops in a Newtonian matrix and Newtonian drops in a Giesekus matrix. Viscoelastic effect on drop deformation turns out to be rather subtle, and may enhance or suppress drop deformation depending on the flow and material parameters.

With the viscoelastic component in the drop or the matrix, the dependence of drop deformation on the Deborah number may be either monotonic or non-monotonic. The former is attributable to the initial "weak regime" in the development of the polymer stress upon startup of elongation, where the instantaneous elongational viscosity is lower for larger De. The latter corresponds to a transition from a "strong regime" to the weak regime, with the instantaneous stress first increasing with De and then declining. In the weak regime, a polymer drop deforms more readily than a comparable Newtonian one, and a polymer matrix is less able to deform a drop than a Newtonian matrix of the same viscosity. In the strong regime, the trend is reversed. Which behavior prevails in a conical flow channel depends on the capillary number Ca, the viscosity ratio β as well as the range of the Deborah number De. A smaller Ca and a smaller β are conducive to larger local strain rates and hence faster polymer growth, whereas a larger Ca or β favors the weak regime.

This scheme reconciles contradictory results in the literature as opposite limits in the parameter space. Thus, it provides a more or less complete picture for viscoelastic effects on drop deformation in transient elongational flows. To verify this picture experimentally, carefully designed experiments should explore low strain rates and fast transients.

Chapter 3

Experiments on selective withdrawal

3.1 Introduction

The term "selective withdrawal" originated from drawing a fluid from a container holding stratified layers of immiscible fluids. In more recent literature, it refers to the flow in the neighborhood of a liquid-liquid or liquid-gas interface induced by suction through a tube. Figure 3.1 shows photographs of the steady-state interface when the suction tube sits at a fixed distance above the undisturbed interface. With increasing suction flow rate, the interface deforms more and eventually the lower fluid may be withdrawn together with the upper fluid in the form of a thin thread.

From the early 1900's, people have applied selective withdrawal to remove poor quality water at the base of dams through scour valves [81]. By the early 1960's, several studies have been done [82–84] to develop a fundamental understanding of this phenomenon. Because selective withdrawal was motivated by applications in water quality control, most studies from that period treated the fluids as inviscid on account of the low viscosity of water. More recently, several groups are still pursuing inviscid models for selective withdrawal along with experiments [85–92]. In the 1980's, igneous geology motivated several studies on the viscous selective withdrawal of magma from the chamber during the process of a volcanic eruption [93, 94]. However, the numerical work of Spera [93] did not include the effect of density difference and the calculations of Blake & Ivey [94] did not include the

effect of interfacial tension. Lister [95] published a theoretical and numerical analysis which showed that both buoyancy and surface tension are important for an accurate description of viscous selective withdrawal. In his work, the suction is represented by a point sink.

Since then, physicists became interested in this phenomenon as a scientific problem of interfacial flow. There have been several experimental and numerical studies on well-controlled Newtonian liquid-liquid systems [5, 96–98] and gas-liquid systems [6, 99, 100]. For liquid-liquid systems, the flow behavior is classified into three regimes: subcritical, critical and supercritical. In the subcritical regime, the interface is deformed into a steady hump and one only withdraws one fluid from the tube. In the supercritical state, the interface forms

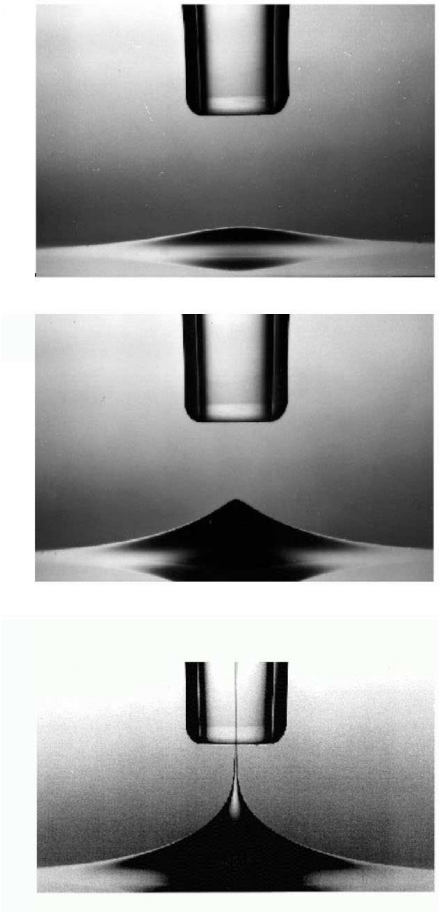

Figure 3.1: The steady-state interface in a selective withdrawal experiment. From top to bottom, the flow rate Q increases and the system is in the subcritical, critical and supercritical regimes. Adapted from Cohen [5] with permission, ©2004 American Physical Society. (http://prola.aps.org/abstract/PRE/v70/i2/e026302)

a spout into the tube and both fluid components are withdrawn. The critical state is the threshold for the uptake of the interface. The hump height in the subcritical regime, i.e. the depth of the interfacial depression at the tip, and the critical flow rate have been measured and computed. It turns out that the appearance of the supercritical regime depends on the viscosity ratio of the components, and in a gas-liquid system, it depends on whether the suction tube sits in the gas or the liquid. If the fluid containing the tube is the gas, then the flow undergoes the same three regimes as liquid-liquid systems. On the other hand, if the ambient fluid is the liquid, only the subcritical state obtains. The free surface always attains a smooth steady-state shape, and no gas can be drawn into the tube regardless of the flow rate. Gas-liquid behavior is of more interest to us since our experiment and computation will concern the deformation of an air-liquid free surface. To sum up this brief review of the literature, for Newtonian systems there is a more or less clear understanding of the interfacial behavior in selective withdrawal.

Meanwhile, new applications have been suggested for selective withdrawal, such as coating of microparticles [101,102] and fabrication of thin glass fibers [103,104]. In such applications, the fluids are usually *non-Newtonian* and exhibit large elastic stresses. But non-Newtonian rheology has so far not been investigated in selective withdrawal. The initial motivation of our work was to study this phenomenon in viscoelastic systems and produce a clear picture about the elastic effect on selective withdrawal. Since the flow near the interface has a strong extensional component, one expects strong manifestation of the viscoelastic stresses. In particular, the coupling between polymer stretching and interfacial deformation will be a focus of our attention. Thus, selective withdrawal is an attractive flow situation in which to explore the interaction between bulk rheology and interfacial deformation, and in this sense is a scientifically significant problem.

Moreover, selective withdrawal in the subcritical state offers a balance between hydrodynamic forces and interfacial tension. After some preliminary numerical simulations of selective withdrawal in viscoelastic system, we have realized a new dimension of this problem: the setup, operated in the subcritical state, may potentially be used as an extensional rheometer to measure the elongational viscosity of the component being withdrawn. On the one hand, the flow near the tip of the interface is very close to homogeneous uniaxial extension. We could obtain the local strain rate near the tip from control parameters such

as flow rate and the geometric setup. On the other hand, the force balance at the interface allows us to calculate the first normal stress difference from the interfacial tension. Between the two, we could calculate the extensional viscosity of the fluid. The significance of such measurements lies in the well-known and long-standing difficulty in measuring elongational viscosity for low-viscosity non-Newtonian liquids [8, 58], especially at lower strain rates. For selective withdrawal to be used as an extensional rheometer, however, several uncertainties have to be resolved first. For example, to what extent is the flow "homogeneous elongation"? Can we obtain the extensional rate accurately? How to back out the elongational stress from the surface tension? Our experimental and computational investigation have led to a degree of success of this strategy. Since these issues have more to do with the computational work than the experimental, we defer detailed discussion to the next chapter.

3.2 Experimental setup and flow control

The experimental setup, shown in Fig. 3.2(a), is modelled after that of du Pont and Eggers [6] in their experiment with Newtonian fluid. It consists of a test tank connected to a control tank by a tube. The test tank has a 3 cm $\times$ 3 cm square cross section and a height of 21 cm. The control tank is much wider and shallower, with a rectangular cross section of 20 cm $\times$ 30 cm and a height of 5 cm. These two tanks are connected by a tube of 0.95 cm inner diameter. In the test tank, there is a vertical circular tube of inner diameter 0.95 cm and outer diameter 1.27 cm. The top of the tube, which is 12 cm above the bottom of the test tank, is sealed by a thin circular disk having a 1 mm hole at the center (Fig. 3.2b). Through this hole, the liquid in the test tank drains down into a reservoir, driven by gravity, and the flow rate is controlled by a valve. Lowering of the free surface in the test tank induces a flow from the control tank through the connecting tube, which to a degree synchronizes the free surface in both tanks. Thus, the control tank serves to increase effectively the cross sectional area of the test tank, without enlarging the viewing depth for the camera.

Two things are important for the flow-control scheme. Because the cross section of the control tank is large and the liquid flow rate is low (below 0.01 ml/s), the liquid level in both tanks changes very slowly during the experiment such that the flow can be considered quasi-steady at all times. Thus, at any moment, the interface and flow field correspond

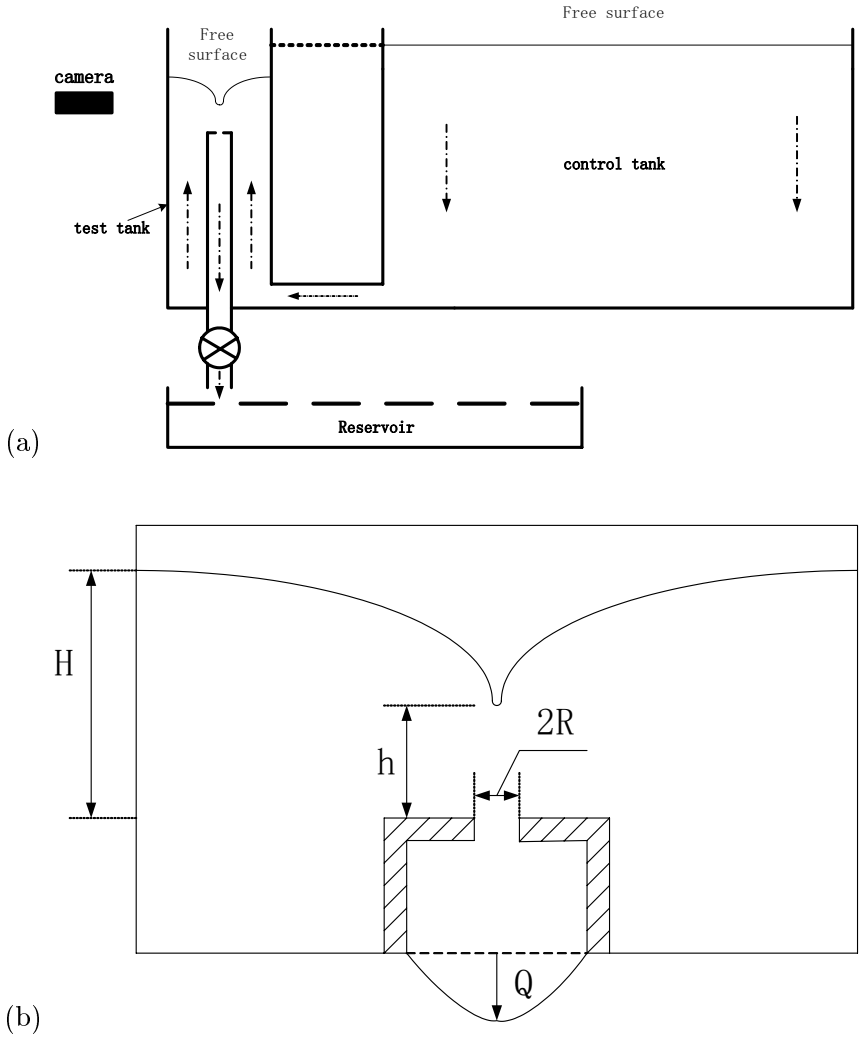

Figure 3.2: Schematic of the experimental setup. Plot (a) shows the whole setup of the experiment, with the arrows showing the direction of flow. Plot (b) magnifies the central portion of the test tank and defines the geometric quantities H, h and R.

to the steady-state situation at the instantaneous flow rate and water level. This way, the experimental results may be compared with steady-state computations in the next chapter. Second, the flow rate Q is essentially constant during the experiment. Q is determined by the opening of the valve and the pressure head from the free surface down to the valve, a vertical height of approximately 50 cm. Since the free surface in the test tank lowers at most 5 mm during an experiment, this has little effect on Q as long as the valve is left at a fixed position. Between experiments, of course, we adjust the valve to achieve different Q values.

Therefore, the control parameters for our experiment are the flow rate Q and the liquid level indicated by the position of the free surface in the test tank H. At the beginning of each experiment, we fill up both tanks to an initial $H \sim 1$ cm. Then the valve at the bottom is opened to a certain position and the flow rate Q is measured by a stopwatch and balance every 10 minutes until it reaches a steady state. A digital camera mounted orthogonal to the plane of the page in Fig. 3.2 monitors the slow decline of H in time. When H lowers to a certain point (on the order of 5 mm but fluid-specific), the interface starts to deform toward the suction tube. The position of the interface is recorded by a CCD camera (Watec WAT-902B or Pixelink PL-B959U) mounted on a horizontal translation stage, which could move in two directions at a step size of 0.01 mm and a maximum range of 5 mm in each direction. The camera is kept roughly level with the tip of the interface and captures the location of the tip, indicated by h, as well as the interfacial shape from which the curvature κ at the tip can be computed. Because the small range of h (0.5 – 1 mm) and relatively long distance between the tip and the camera ($\sim$ 30 mm), little error is introduced by the small change in viewing angle ($\sim 2^\circ$) as the interface lowers relative to the camera. The flow loop and cameras are mounted on an optic table and all experiments are done in an air-conditioned laboratory with room temperature fixed at 21°C. A typical experiment lasts 30 minutes.

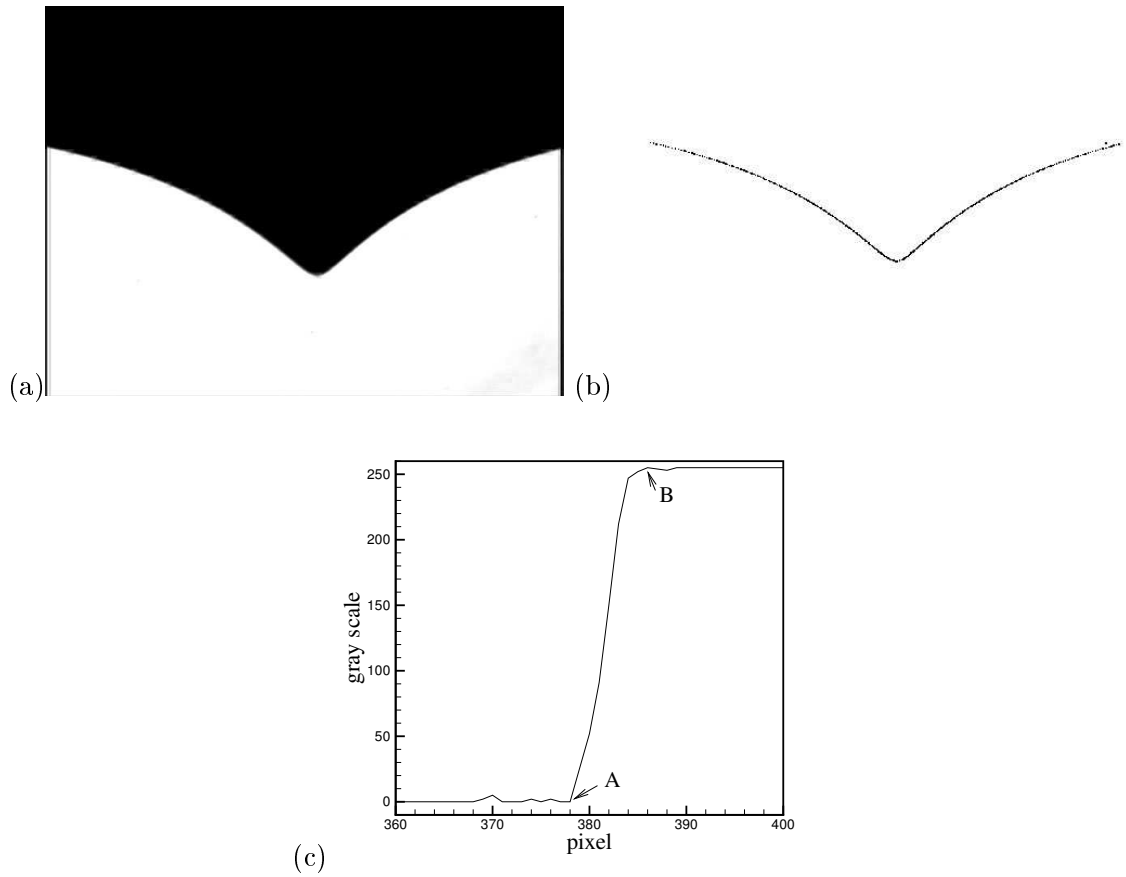

Figure 3.3: Edge detection for locating the interface. (a) The original grayscale image from the experiment. The sharp contrast was obtained by backlighting . (b) The interface determined by MATLAB. (c) A typical light-intensity profile along a horizontal line from (a).

3.3 Image processing and data analysis

The direct outcome of the experiment is grayscale video recorded by the CCD camera, at 16 frames per second and 480×640 pixels. Next we use Windows Movie Maker to extract still pictures from the video. To determine the location of the interface from such pictures, we use MATLAB to compute the spatial gradient of the light intensity in the images. Generally, such "edge-detection" is accomplished by using one of two methods, gradient and Laplacian [43]. The gradient method detects the edge by finding the maximum in the first derivative of the light intensity in the image. The Laplacian method relies on zeros of the second derivative. In MATLAB, the Canny filter uses a gradient method to determine the edge in the picture. As an example, Fig. 3.3 shows the result of the Canny edge detector

in MATLAB. The interface is smooth and sufficiently clearly defined for our data analysis. Figure 3.3(c) shows a typical horizontal profile of light intensity for edge detection. The maximum error in locating the edge is half of the distance between A and B. For most cases, this is round 5 pixels.

After the free surface is determined by MATLAB, h and κ are calculated from it. The point with the lowest position (or the "tip") is located and its two neighbors are also marked. h is the distance between the tip and the orifice of the tube. A second-order polynomial is used to fit the three points and calculate the tip curvature κ. The error in determining the curvature stems from that in locating the edge. The uncertainty in the edge location is 5 pixels and the horizontal distance between the tip and its neighbor is typically 80 pixels. Thus, the error of curvature is around 12.5%.

3.4 Test fluids: composition and rheology

In the experiments we have used silicone oil as a Newtonian fluid and polymer solutions of polyisobutene (PIB, with molecular weight $M_W \sim 2\times10^6$, Oppanol B, BASF) in polybutene (PB-H35, $M_W \sim 700$, INDOPOL H-35; PB-H50, $M_W \sim 800$, INDOPOL H-50; PB-H100, $M_W \sim 910$, INDOPOL H-100, all from BP Amoco) and heptane as viscoelastic fluids. All materials are used as received with no further processing or refinement. The silicone oil is from "The Chemistry Store.com" with a density of 760 kg/m^3 and a shear viscosity of 9.5 Pa·s. We have mainly used two polymer solutions, termed "strongly elastic" (SE) and "weakly elastic" (WE), with compositions given in Table 3.1.

Solution	PIB	heptane	PB-H35	PB-H50	PB-H100
SE fluid	0.17%	4.3%	52.3%	21.7%	21.5%
WE fluid	0.034%	1.03%	0	99%	0

Table 3.1: The composition of the polymer solutions. PB-H35, PB-H50 and PB-H100 are three types of PB with molecular weight of 700, 800 and 910.

Because the PIB is a rubbery solid that does not dissolve directly in PB, we first dissolve the PIB in heptane and then mix the solution into PB of various grades to produce the working solutions for the experiment. The polymer solutions are prepared according to the following protocol.

(a) Measure prescribed amounts of PIB and heptane by a balance (Ohaus Scout Pro, 200±0.01 g);

(b) Dissolve PIB in heptane by using a magnetic stirrer for about 1 week at 21°C in an air-conditioned room;

(c) Measure a prescribed amount of PB by the balance;

(d) Mix the PIB-heptane solution into the PB using a large stirrer for 2-3 days at 21°C.

We have measured the surface tension σ of the liquids at 21°C using the ring method (Cole-Parmer, Surface Tensiomat Model 21), and obtained the following values: $\sigma = 21.3$ mN/m for silicone oil, 27.3 mN/m for the SE fluid and 32.1 mN/m for the WE fluid. During the experiment, surface adsorption of contaminants is possible. But our Newtonian experimental results match very well with du Pont and Eggers' work [6] as well as our own computations (see Chapter 4). This indicates that any effect of surfactants on our experiment is negligible. Thus, we have not used any surface-cleaning procedure during the experiments.

Comparing the PIB molecular weight and the concentration of our polymer solutions with those in the literature, we expect them to be dilute Boger fluids [105–111]. Their shear rheology measured on a Bohlin CVO-R rheometer largely bears this out (Fig 3.4). For both fluids, the shear viscosity μ remains essentially constant for $0.1\ \mathrm{s}^{-1} < \dot{\gamma}_1 < 30\ \mathrm{s}^{-1}$. For higher shear rates, shear thinning becomes appreciable. Below $0.1\ \mathrm{s}^{-1}$, the data are noisy and unreliable; this is near the lower limit of the testing range for the transducer used. Data for first normal stress difference N_1 are reliable for $\dot{\gamma}_1 > 1\ \mathrm{s}^{-1}$, above which N_1 scales with $\dot{\gamma}_1^2$ as expected for Boger fluids. At higher shear rates, the $N_1(\dot{\gamma}_1)$ dependence becomes milder, consistent with the onset of shear-thinning in μ. The minimum shear rates for reliable μ and N_1 are consistent with earlier reports in literature [53]. Both μ and N_1 decrease with temperature, as expected [18]. As mentioned before, all selective withdrawal experiments will be carried out at 21°C.

We have also used the Capillary Breakup Extensional Rheometer (CaBER, ThermoHaake) to measure the elongational viscosity of the polymer solutions, and the results are shown

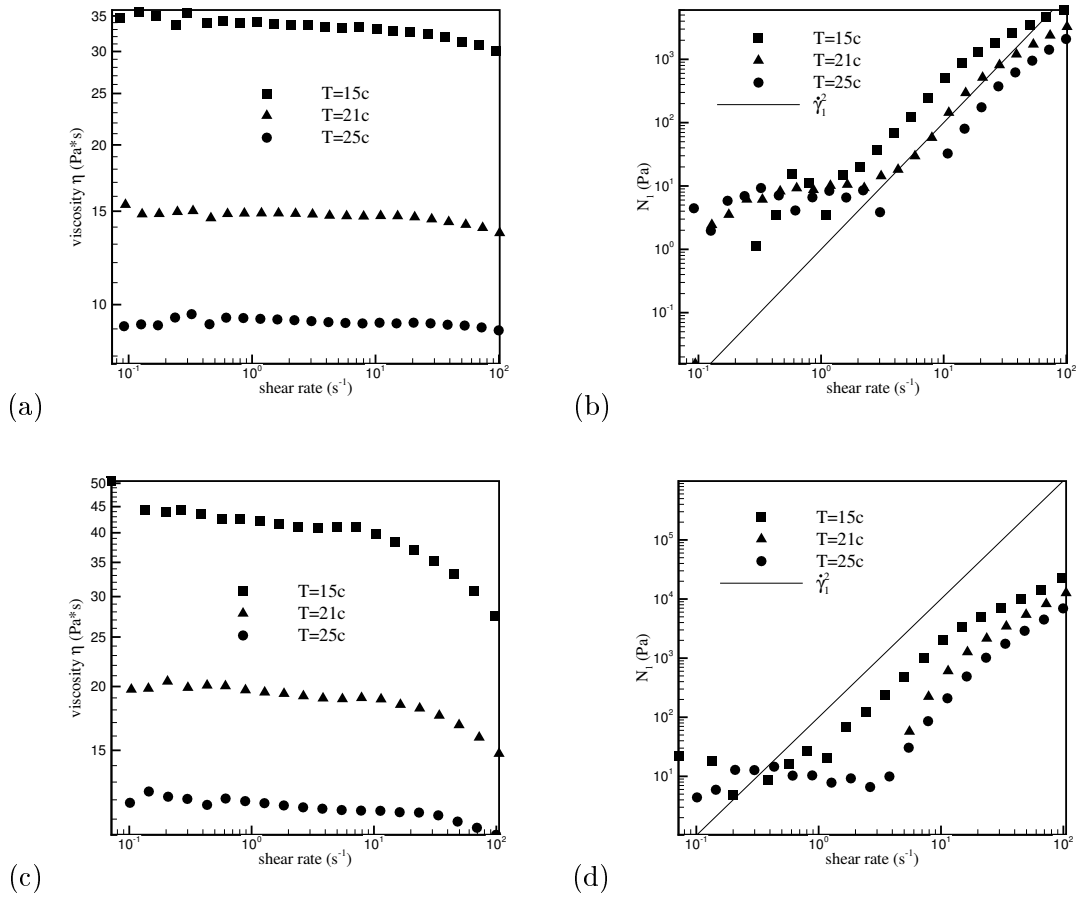

Figure 3.4: Shear rheology of our polymer solutions at three temperatures. (a) and (b) show the shear viscosity and first normal stress difference for the WE fluid, while (c) and (d) are for the SE fluid. The straight line in (d) indicates the slope for a $N_1 \propto \dot{\gamma}_1^2$ scaling on the log-log scale.

in Fig 3.5. CaBER records the capillary thinning of the polymer thread, which is governed by the balance between the capillary force and the elongational stress. Unlike the filament stretching device, the elongational rate during this process is not constant but undergoes a rather complex temporal variation. As the result, CaBER cannot provide the steady-state elongational stress under a constant elongational rate, but yields an "elongational stress growth viscosity" $\bar{\eta}^+$ [18], as a function of time or strain. Figure 3.5(b) shows that as the polymer chains get stretched, they contribute to a steep increase in $\bar{\eta}^+$ commonly known as *strain hardening*. Toward the end of the filament thinning, $\bar{\eta}^+$ appears to level off. The data become noisy due to the uncertainty in resolving the diminishing filament diameter.

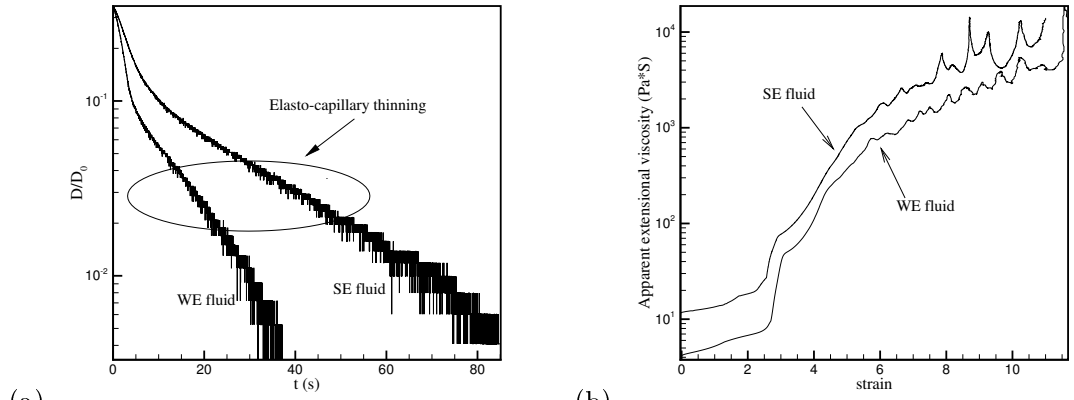

(a) (b)

Figure 3.5: CaBER measurements of (a) the dimensionless diameter of the fiber and (b) the apparent extensional viscosity of SE and WE fluids at 21°C.

But it appears safe to assume that steady-state stretching has not been achieved. Our data are consistent with CaBER measurements in the literature [112].

Another important quantity measurable by CaBER is the relaxation time λ_H. For dilute polymer solutions, there is an "elasto-capillary thinning" regime [112] during which the filament diameter decreases exponentially with time and the elongational rate is approximately constant. Subject to such strain, the Giesekus model predicts an "elongational stress growth viscosity" $\bar{\eta}^+$ that increases exponentially with time or strain [113]. In Fig 3.5(a), we also find this "elasto-capillary thinning" regime for our fluids. Curve fitting the Giesekus model then gives us the relaxation time of the fluids: $\lambda = 8.50$ s for the SE fluid and 3.77 s for the WE fluid.

Since the experimental project lasted months, we were concerned about aging and degradation of the polymer solutions due to heptane evaporation and polymer chain scission. To check such effects, we measured the shear as well as elongational rheology of the solutions at the beginning and end of the project. There are no significant differences that would indicate aging and degradation. For the SE fluid, the relaxation time decreases from 8.63 s to 8.5 s. Since selective withdrawal subjects the polymer chains to elongation, the chain scission is reasonable and very small. The heptane concentration is very low, and does not contribute much to the rheology in any event. So it is expected that solvent evaporation not be a major factor.

3.5 Results for Newtonian fluid

To reprise, our experimental procedure consists in fixing the flow rate Q and following the evolution of the interface as the free surface position H gradually lowers. Using the radius of the suction hole R as the characteristic length, and Q/R^2 as the characteristic velocity, we construct a capillary number:

$$Ca = \frac{\mu Q}{\sigma R^2}, \tag{3.1}$$

where σ is the surface tension and μ is the viscosity of the Newtonian fluid. For the polymer solutions to be studied in the next section, Ca is similarly constructed using the constant viscosity μ at moderate shear rates (cf. Fig. 3.4). In addition, there are length ratios H/R, h/R and κR, and we have found it convenient to use $\chi = (H - h)/R$ in data reduction.

Figure 3.6 shows a typical example of the interfacial deformation for Newtonian fluid at a fixed flow rate corresponding to $Ca = 10.22$. We started with an initial $H = h = 6.5$ mm. In the first 1000 s, the interface shows no visible deformation so H remains equal to h. As both decrease to ~ 4.5 mm, at time $t \sim 1200$ s, the interface forms a gentle downward protrusion, which becomes more pronounced as H and h further lowers (Fig. 3.6a–c). Now h falls below H and $H - h$ gives the depth of the depression at the center of the interface, which will also be called the "hump height". Also note that the tip of the protrusion becomes more pointed as the interface gets nearer to the suction tube and the viscous force of the flow becomes stronger. Toward the end, the tip seems quite pointed, and eventually enters the opening of the suction tube (Fig. 3.6g,h). Generally speaking, the evolution of the interfacial shape is gradual and the process lasts more than 30 minutes. The lack of abrupt changes contrasts the behavior of polymer solutions, as we will see in the next section.

What is conspicuously lacking in the above process is the subcritical-to-supercritical transition depicted in Fig. 3.1 for liquid-liquid selective withdrawal. In the experiments of Cohen *et al.* [5, 96], various liquid pairs were used to cover a viscosity ratio $\nu = 10^{-3} - 2$. Here ν is defined as the ratio between the liquid on the opposite side of the nozzle to the liquid containing the nozzle. In all cases, there is a critical condition, reached by increasing Q or decreasing h, where the tip ruptures into a jet. They also found the critical Q to be independent of ν, an observation that was later confirmed by the numerical computations

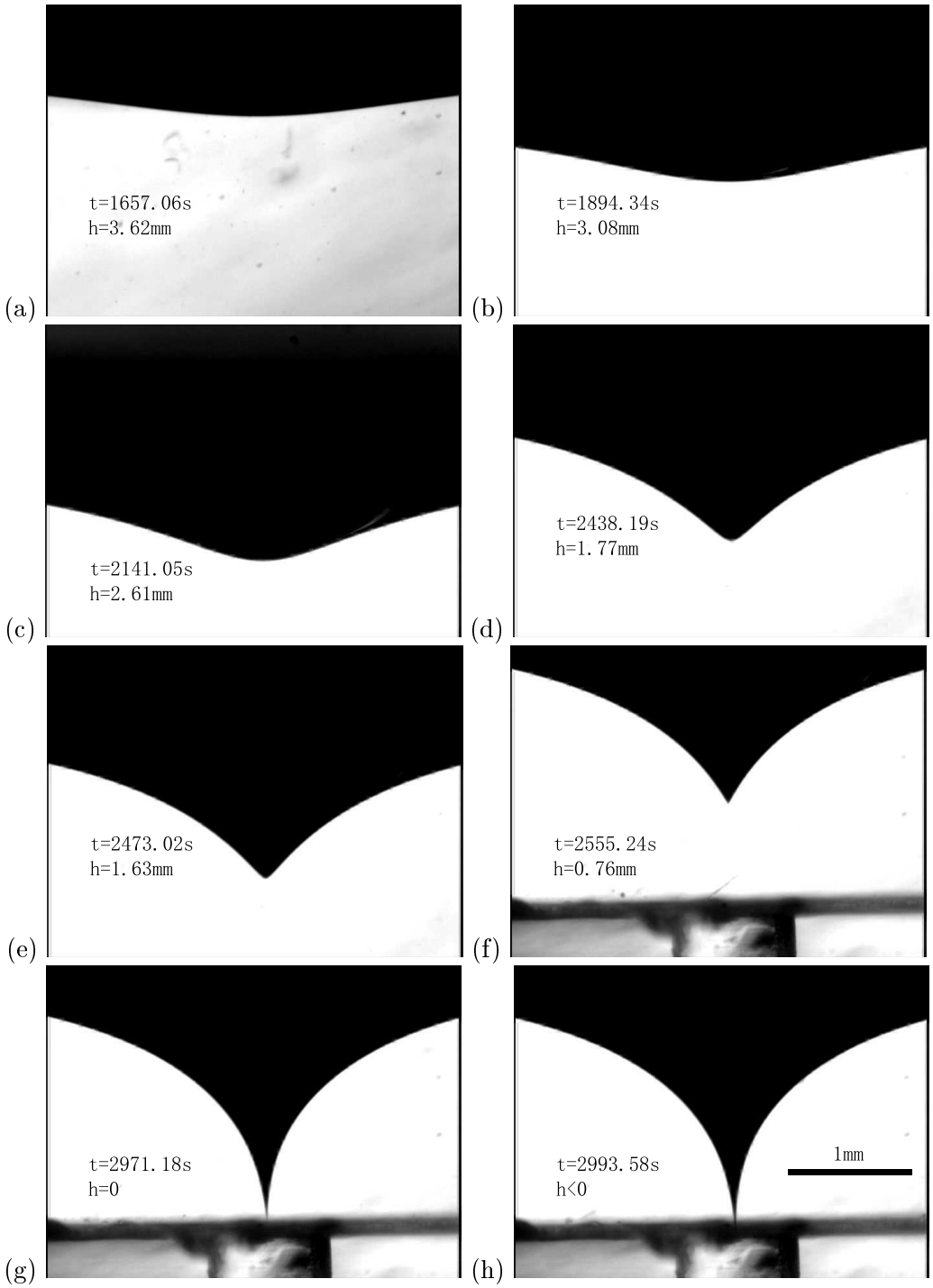

Figure 3.6: Evolution of the free surface for Newtonian fluid at a fixed flow rate corresponding to $Ca = 10.22$. Note the duration of the experiment and the length scale. The last three images show the opening of the suction tube.

of Blanchette *et al.* [114]. This critical condition is also consistent with the computational result of Lister [95] for equal-viscosity fluids. Finally, Jeong and Moffat's analytical and experimental study on cusp formation [115] reports a critical condition for an interface perturbed by two counter-rotating rolls generating a flow orthogonal to and away from the interface.

With an air-liquid system, du Pont and Eggers [6,99] explored the existence of a critical state with increasing Q and decreasing distance h. In their system, as in ours, the viscosity ratio ν is around 10^{-6}. From their experimental data for the subcritical state (partially depicted in Fig. 3.7), they initially suggested that the tip curvature should diverge as $\kappa \sim (h - h^*)^{-3}$, h^* being the critical position of the tip when it becomes a cusp [6]. No jet was found. Later, boundary-integral computations allowed them to explore higher κ than in the experiments, and they found that the power-law scaling fails for larger κ; instead of diverging, it seems to approach a finite limit as h decreases [99]. Based on this, du Pont and Eggers concluded that no critical state exists for the air-liquid system.

This conclusion seems consistent with our findings. First, we never observed the formation of a spout or jet. Even as the tip descends into the tube, the evolution is smooth and gradual. Second, we never observed a cusp, and the tip always appears to be round in this process, despite the appearance of Fig. 3.6(f–h), if viewed under sufficient magnification. Of course, finite optical resolution limits the magnitude of the curvature that we can confidently calculate from the image. But the highest curvature we have seen is around $\kappa R = 23.5$, for which the interface is still adequately resolved. Thus, our experiment supports du Pont and Eggers' conclusion that no critical condition exists for air-liquid systems having a small ν.

To reconcile this with the liquid-liquid result that the critical flow rate is independent of ν [5, 96, 114], we speculate that when ν becomes sufficiently small, the critical flow rate will increase without bound. The critical condition in selective withdrawal can also be likened to the loss of steady shape of a drop or bubble in extensional flow [39]. If the drop-to-matrix viscosity ratio ν is larger than 1, the critical Ca for the burst of the drop is largely independent of ν. When ν decreases below 1, the critical Ca increases, apparently following a power-law and without an upper bound.

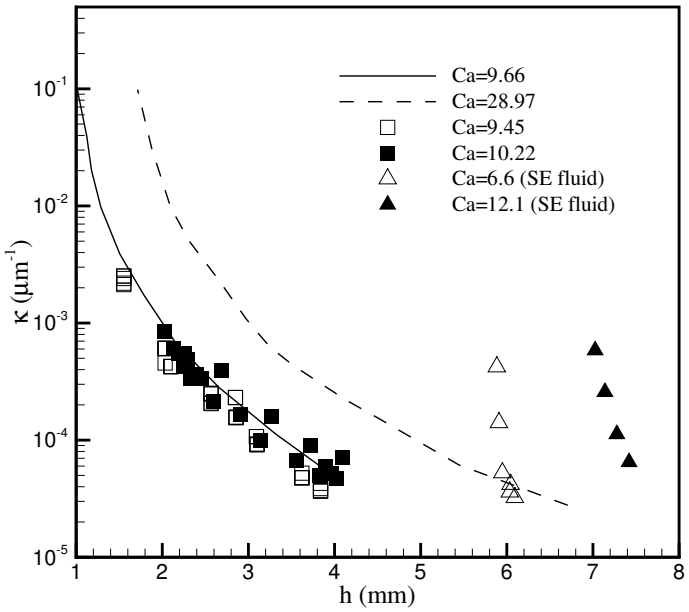

Figure 3.7: The tip curvature κ increases as the interface moves down toward the suction tube during the process depicted in Fig. 3.6. The two lines represent the data of du Pont and Eggers [6] and all the symbols are our experimental data. The two sets of data marked SE fluid are for viscoelastic polymer solutions, and they will be discussed in the following section.

For a more quantitative comparison between our experiment and that of du Pont and Eggers [6], we plot in Fig. 3.7 the steady-state tip curvature κ as a function of the tip location h, with the flow rate fixed at several values of Ca. In both experiments, κ increases with decreasing h for a fixed Ca, and increases with Ca for a fixed h. We have attempted to tune our flow rates toward $Ca = 9.66$ of du Pont and Eggers' experiment; our data sets for $Ca = 9.45$ and 10.22 closely hug their data. Thus, we are satisfied that our experiments with Newtonian fluids agree closely with theirs.

3.6 Viscoelastic fluid

The strength of elastic effects is typically represented by the Deborah number [18]:

$$De = \frac{\lambda_H Q}{R^3}. \tag{3.2}$$

In this definition, as for Ca before, the nominal velocity at the suction tube $V = Q/R^2$ is taken to be the characteristic velocity. Since both De and Ca are proportional to V, it seems reasonable to use the ratio

$$E = \frac{De}{Ca} = \frac{\lambda_H \sigma}{\mu R} \tag{3.3}$$

to indicate an "intrinsic" strength of elasticity. We will call this the *elasticity number* following Grillet *et al.* [25]. Except for the length scale R, E is essentially a material constant. For the experimental setup used here, $E = 22.1$ for the SE fluid and 15.1 for the WE fluid.

Figure 3.8 depicts the evolution of the free surface of the polymer solution SE. We start with $H = h = 4.37$ mm. In the initial period of the experiment, the free surface is flat, with no visible deformation or curvature. Then, at the time of the first picture in the series ($t = 480$ s), the deformation of the free surface becomes visible. In a short duration of little more than 30 seconds, the deformation very quickly becomes more pronounced. By $t = 509$ s and $h = 3.49$ mm, the surface becomes unstable, and the system approaches the critical state. First, the tip apparently becomes a sharp cusp. Then quickly the cusp extends downward, and a thin air jet is ejected from the tip, which remains stable as h continues to decrease. Now the system is in the supercritical state ($t = 517$ s, $h = 3.44$ mm). To keep the free surface sharp, we had to use lighting from the back of the test tank in recording the video. In this arrangement, the air jet is not visible in the pictures. But it is in Fig. 3.9, taken with lighting from the top. Note that in comparison with the Newtonian picture (Fig. 3.6), the surface deformation remains modest even in the supercritical state. At later times, the free surface continues to move down, and the "cone" at the base of the air jet gradually becomes more pointed. The very prominent cone of Fig. 3.9, comparable to the Newtonian one, was achieved at a much higher flow rate and Ca.

This is an overview of the whole deformation process for viscoelastic liquids. For the weakly elastic (WE) solution, the qualitative features are the same. But the onset of deformation and the critical state all occur at smaller h than in Fig. 3.8, even though the experiment was at a higher flow rate ($Ca = 7.59$ and $De = 115$). In the following, we will discuss the subcritical, critical and supercritical regimes in turn.

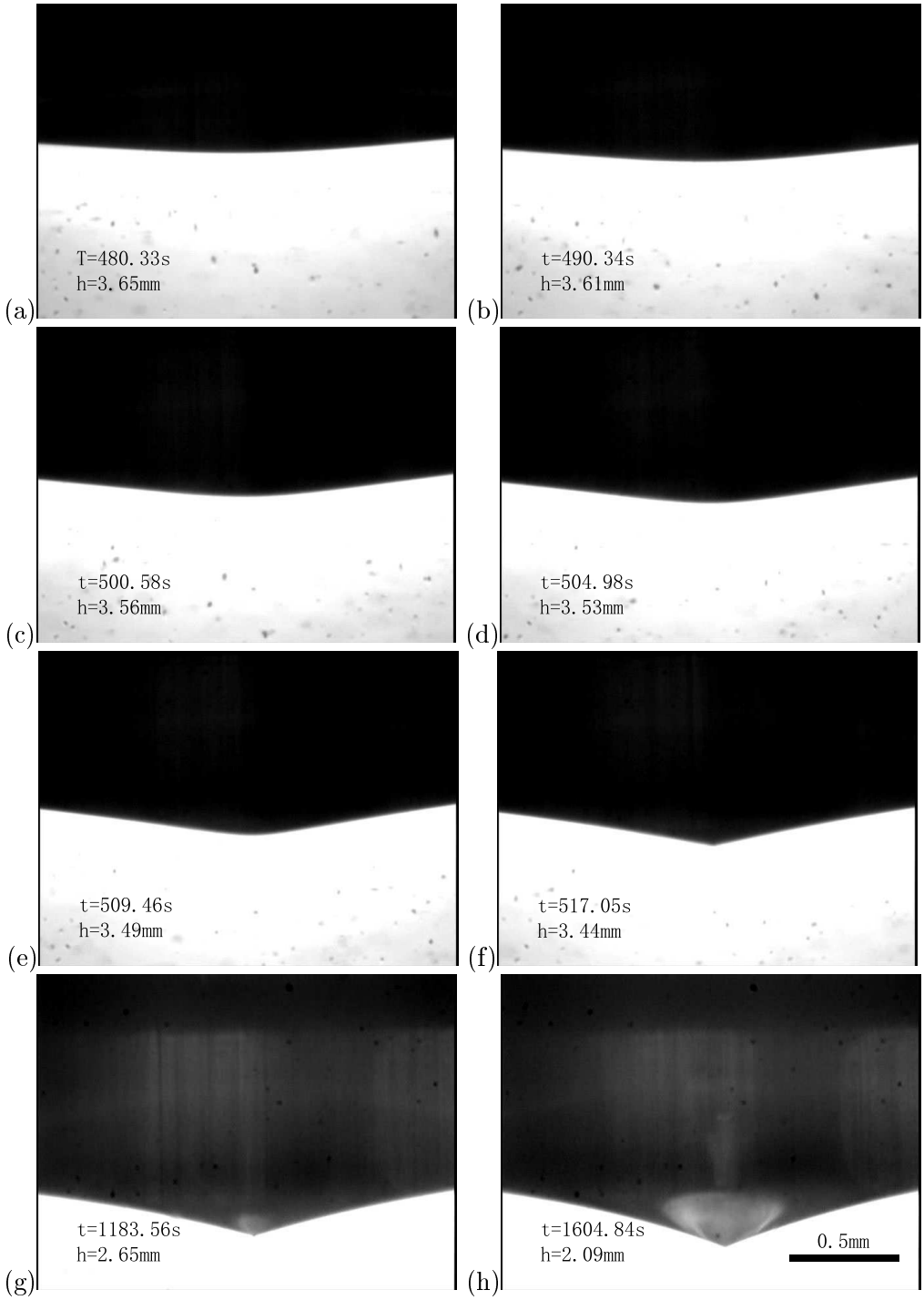

Figure 3.8: Evolution of the free surface of the polymer solution SE at $Ca = 2.5$ and $De = 55.3$. The system is subcritical until $t = 509.46$ s and is supercritical thereafter.

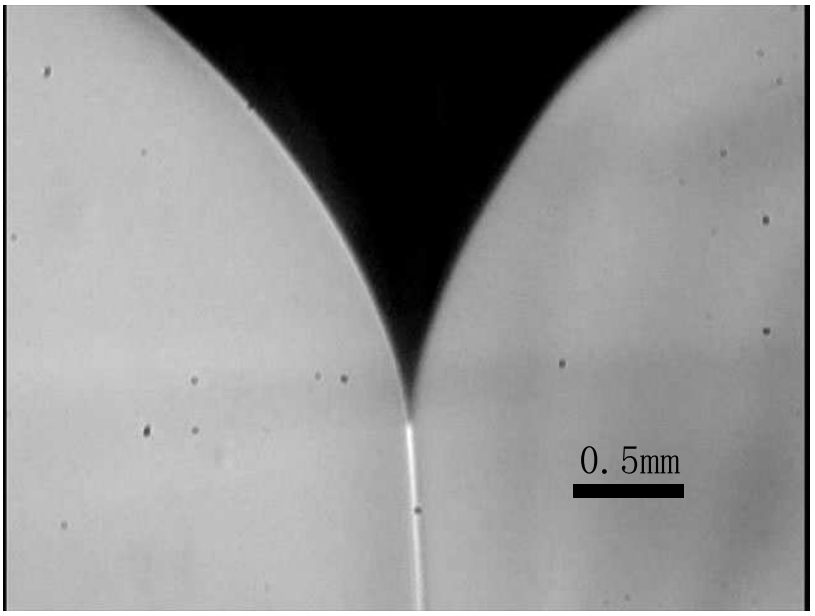

Figure 3.9: Snapshot of the air jet in the supercritical regime for the viscoelastic fluid SE. $Ca = 9.5$, $De = 231$ and $h = 2.1$ mm.

3.6.1 Subcritical regime

Since the Newtonian experiments of the last section consist of only subcritical deformation, this is the only regime comparable between Newtonian and viscoelastic liquids. This regime of interfacial deformation is quite different between the two types of fluids. First, for the same values of Ca and h, the free surface deforms much more in viscoelastic fluids than in Newtonian fluids, producing a much larger tip curvature. Typically, the free surface of viscoelastic fluids begins to deform visibly at an H value far greater than that for the Newtonian free surface. That is to say, given the same Ca, the viscoelastic free surface feels the flow effect at a much larger distance from the suction tube. This is apparent from Fig 3.7, where for the Newtonian fluid at $Ca = 9.45$, detectable deformation of free surface occurs after h falls to $h \approx 4$ mm. For the viscoelastic SE fluid, on the other hand, the free surface starts to deform visibly at $h \approx 6$ mm even though the Capillary number($Ca = 6.02$) is lower. By $h \approx 5.8$ mm, the system has entered critical state with $k \to \infty$. The obvious explanation for the difference is that the viscoelastic fluid produces additional normal stress that pulls the interface downward. As the flow near the tip is mostly elongational, another way of

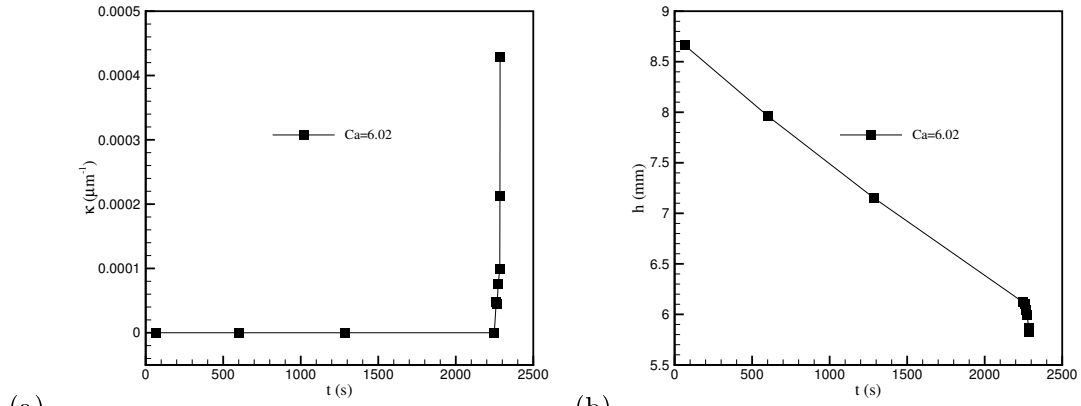

Figure 3.10: Temporal evolution of (a) the tip curvature κ and (b) the tip position h for SE at $Ca = 6.02$ and $De = 146$.

expressing the same idea is that the polymer solutions exhibit much larger elongational viscosity.

Second, the interfacial evolution is slow and smooth for Newtonian fluids (around 30 min in Fig. 3.6), but much more abrupt for viscoelastic fluids. This may be discerned from contrasting Figs. 3.6 and 3.8, and is more quantitatively shown in Fig. 3.10 plotting the temporal change of the tip curvature κ and position h for a viscoelastic fluid. The subcritical regime prevails until $t = 2261$ s. During most of this time, the interface is hardly deformed at all. Thus, κ remains near zero and h declines roughly linearly. Then in a very short time ($2261s < t < 2285s$), the interface undergoes the transition to the supercritical regime. This is manifested by the sharp upturn of κ and downturn of h, both going without bounds as the air jet emanates from the tip. This difference can again be traced to the additional polymer stress during elongation. As the interface lowers toward the suction tube, the elongation near the tip increases and the fluid experiences greater strain. While the elongational viscosity η_n of a Newtonian fluid remains constant at 3μ, that of viscoelastic liquids is known to increase sharply with the amount of strain in an effect known as strain hardening [18]. This greatly increases the pulling force of the liquid on the interface, which quickly destabilizes the interface and precipitates the system into the supercritical state.

The relatively rapid evolution of the interface raises the question of whether the evolution of the viscoelastic free surface can still be considered quasi-steady. This is important

since in the next chapter we will compare these data to steady-state computations. The question can be answered by comparing the transient acceleration term with the viscous term in the Navier-Stokes equation, thereby producing a "transient Reynolds number" $Re_t = \rho R^2/(\mu T)$, where T is the time scale for the transient. Using $T = 20$ s, we have $Re_t = 5 \times 10^{-3} \ll 1$. Thus, the transient acceleration $\rho \frac{\partial V}{\partial t}$ is much smaller than the viscous force, and the process can be assumed quasi-steady throughout.

Finally, the interfacial deformation tends to be much more localized for the viscoelastic liquids. In other words, compared with a Newtonian hump bearing the same tip curvature, the viscoelastic hump is much narrower. This probably reflects a localization of the polymer stress, which is in turn another manifestation of strain hardening. The polymer stress depends not only on the local strain rate but also on cumulative strain. The fact that it remains small away from the tip of the interface and then rises sharply at the tip reflects not only the larger strain rate there, but also the larger cumulative strain attained. As a consequence, the viscoelastic hump is narrower than a comparable Newtonian one.

3.6.2 Critical state

The critical state is the boundary between subcritical and supercritical regimes. As mentioned in section 3.5, an air-Newtonian-liquid system exhibits only subcritical behavior; the critical and supercritical states do not exist. The viscoelastic liquids considered in this section do exhibit critical and supercritical behavior. The free surface forms a pointed cusp, from which a thin air jet is drawn out. This process can be compared with the rise of bubbles in a viscoelastic liquid [2, 22, 116–118]. When the rise speed is sufficiently fast, the downstream surface of the bubble forms a cusp. In some cases, a thin filament forms at the cusp (Fig. 1.2). Another related phenomenon is tip-streaming. Subject to extensional flows, surfactant-laden bubbles and drops deform into spindle shapes with pointed ends, and then emit a train of tiny bubbles or droplets from these points [119–123]. In all these scenarios, the underlying physics seems to be large extensional stress overcoming the interfacial tension to rupture the interface. With surfactant-covered drops and bubbles, tip-streaming is facilitated by the interfacial tension being locally suppressed by surfactant accumulation.

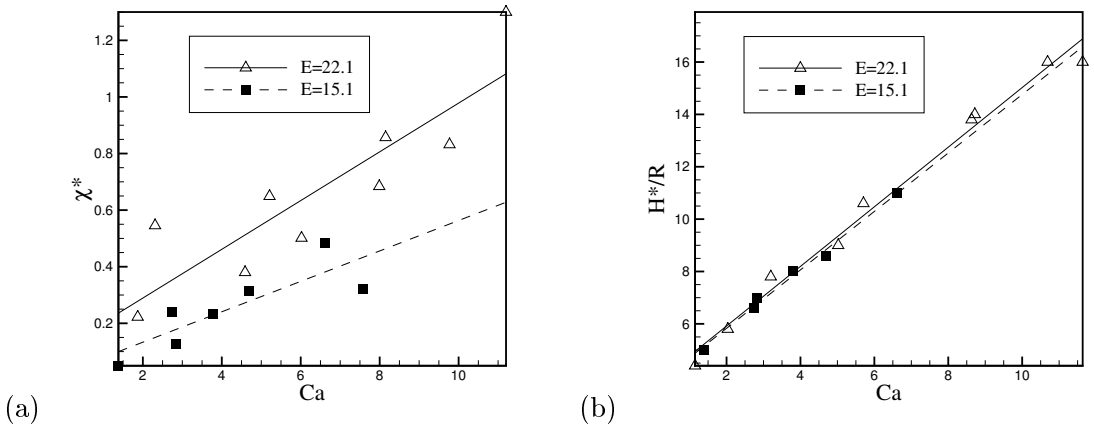

Figure 3.11: The critical condition indicated by (a) the hump height χ^* and (b) the liquid level H^*/R as functions of Ca for the SE ($E = 22.1$) and WE ($E = 15.1$) solutions.

With viscoelastic fluids, extension of the polymer chains produces extraordinary elongational stresses that draws a cusp or filament from the interface. Such seems to be the case with the critical transition in viscoelastic selective withdrawal.

(a) Effect of viscoelasticity on critical condition

Our typical experimental protocol consists of draining the liquid out at a fixed flow rate Q or capillary number Ca, and recording the evolving interfacial shape. As such, the critical condition is most easily recorded as a critical liquid level H^* in the test tank since H is one of our control parameters. Of course, there is also a critical tip position h^*, which can be obtained from image analysis. From this we can define a critical value for the dimensionless hump height

$$\chi^* = \frac{H^* - h^*}{R}. \tag{3.4}$$

Note also that a different critical liquid level is obtained for the *reverse* transition from supercritical to subcritical regimes. This hysteresis will be discussed separately below.

Figure 3.11 depicts the critical condition over a range of Ca for the two polymer solutions. The critical hump height χ^* increases both with Ca and E. The critical H^* behaves similarly, although the dependence on E is less pronounced. This trend can be rationalized as follows. Since E scales with the polymer relaxation time, it represents the capacity of the polymer chains to stretch and generate elongational viscosity [18]. On the other hand,

Ca is proportional to the flow rate Q, and thus also proportional to the strain rate at the interface. Consequently, an increase in either E or Ca results in greater polymer stress pulling on the interface. The interface reacts by forming a deeper depression toward the nozzle so as to increase the buoyancy force to balance the polymer stress. This explains the increase in χ^*. Besides, with increasing polymer stress, the interface "feels" the same amount of pull at a larger distance H from the nozzle. Hence H^* increases with Ca and E as well.

(b) *Hysteresis*

A hysteresis exists when the critical condition is approached by a decreasing H or increasing H. The former is the dominant protocol for our experiment; we fix the position of the control tank and the position of the valve, and let the liquid drain out at a constant Q. To increase H, on the other hand, we start with the supercritical state and then elevate the control tank in small increments. Enough time (5-10 minutes) is allowed between the increments for the flow to reach steady state. Although we have not tested this, we expect a similar hysteresis with increasing or decreasing Ca.

Figure 3.12 shows the hysteresis in terms of H^* achieved by increasing or decreasing H. The data divide the H–Ca plane of control parameters into three regions. In the top region, a smooth free surface is always stable and remains in the subcritical regime. In the bottom region, the cone-jet configuration of the free surface is always stable and the system remains in the supercritical regime. The middle region between these two is *transitional* in the sense that the state of the free surface depends on the deformation history; it is the same as the previous state as one traverses the three regions along vertical lines, by increasing or decreasing H.

Similar hysteresis has been found in selective withdrawal of Newtonian liquid-liquid systems [96, 98]. But in gas-fluid systems, all previous work dealt with Newtonian fluids, which do not exhibit a critical state. Therefore, this is the first time hysteresis is reported for gas-liquid systems.

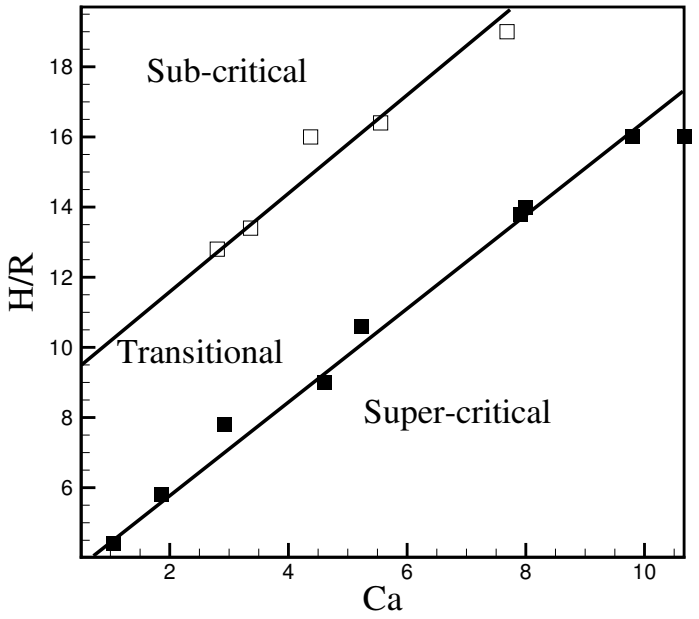

Figure 3.12: Hysteresis of the critical state for the SE fluid. The subcritical-to-supercritical transition is achieved by lowering H, while the reverse is achieved by increasing H.

3.6.3 Supercritical regime

The most striking feature of the supercritical regime is the air jet that emanates from the cusp of the interface and extends toward the suction tube (Fig 3.9). It has a diameter D_a on the order of 10 μm, and as such requires high magnification of the video camera to be viewed and recorded. Using the magnification of Fig 3.9 (1 pixel $\approx 7\mu m$), the air jet is visible for about 1 cm below the cusp. Below that, it apparently disappears and may have broken up into tiny bubbles. In our video image, the edges of the jet are not completely steady, but appear to fluctuate slightly in time. The reason for this fluctuation is not clear at present. Because of the small size of the jet, it is conceivably very sensitive to external disturbances, which may come, say, from minute variations in the flow rate or the passing of nearby particulate contaminants suspended in the fluid. Note also the slight slant of the air jet in Fig 3.9 to the right. This may reflect a small geometric misalignment.

Considering this temporal variation and the limited spatial resolution, we put the maximum uncertainty in measuring D_a at 15%. In the experiment, D_a is measured from video images

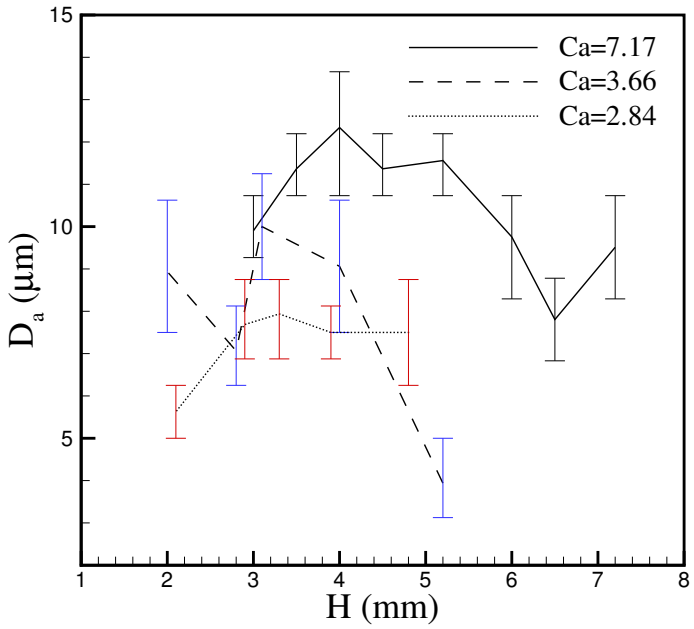

Figure 3.13: The diameter of the air jet D_a as a function of H for 3 values of Ca. All the results are for the SE fluid with $De/Ca = 22.1$. The error bars represent the degree of uncertainty in measuring D_a due to finite optical resolution and apparent fluctuation of the edge of the air jet.

captured by a high resolution (1 pixel $\approx 1\mu m$) CCD camera. The air jet typically covers 10-15 pixels on the screen. An uncertainty of half of pixel at the edges then leads to roughly a 5% error. A second source of error is the small fluctuations of the edges of the jet. For each H value, we take three pictures of the air jet and average the D_a values from them. The difference in D_a among the pictures ranges from 5% to 10%.

Figure 3.13 plots D_a as a function of the control parameter H at 3 fixed Ca values. The amount of scatter makes it hard to discern definite trends. But D_a seems to increase with Ca, all other factors being the same. This would be reasonable considering that a higher flow rate draws more air into the jet. Besides, D_a appears to increase with H first, and then decreases. As present, we do not have an explanation for this non-monotonic behavior. A more definite understanding of D_a awaits future observations at greater image resolution.

Previous work on Newtonian liquid-liquid selective withdraw has documented similar liquid jets in the supercritical state. Cohen *et al.* [5,96] observed such jets for viscosity ratio μ down

to 10^{-3}, but did not report the jet diameter. The later study of Case and Nagel [98] shows liquid jets of diameter around 20 μm for a viscosity ratio $\mu = 0.005$. This is comparable to our data, although our μ is on the order of 10^{-6}.

3.7 Conclusion

The main findings of this chapter can be summarized as follows.

(a) The free surface of a polymeric liquid exhibits a supercritical regime, in contrast to Newtonian liquids.

(b) The subcritical-supercritical transition shows a hysteresis in terms of the critical liquid level. With increasing elasticity, the transition occurs at lower flow rates or higher liquid levels.

(c) In the subcritical regime, the free surface of polymer solution deforms much more than the Newtonian one under similar conditions. The deformation also tends to be localized to the tip, with a narrower region being disturbed.

All can be rationalized by the elongational stress due to the polymer that tends to pull the interface downward toward the suction tube. In particular, the strain-hardening behavior, i.e. the rapid increase of the elongational viscosity with cumulative strain, plays an important role. A possibility alluded to before is that the selective withdrawal process, in the subcritical regime, may be used to measure the elongational viscosity of polymeric liquids. This idea will be further developed in the next chapter.

Chapter 4

Numerical simulation of selective withdrawal

4.1 Introduction

The experimental observations reported in the last chapter indicate that viscoelastic polymer solutions behave markedly differently from viscous Newtonian fluids in selective withdrawal. We have speculated that these differences arise from the viscoelastic stresses near the tip of the interface, where the polymer solution experiences elongational flow. We even further speculated that this device can be used as an elongational rheometer if operated in the subcritical state. The force balance, between the elongational stress and the capillary force, may allow one to back out the former from the surface curvature and known interfacial tension. The general goal of the present chapter is to substantiate these proposals by quantitative computation.

4.1.1 Computational strategy

Aside from the non-Newtonian rheology, we have to surmount a second obstacle—interfacial deformation—in order to successfully compute the selective withdrawal. This is a generic problems for flows involving free surfaces or interfaces. Mathematically, the surface needs to be treated as a boundary on which boundary conditions are imposed. However, the surface also moves and deforms according to the flow and forces in the bulk fluids. Therefore,

its location is not known before hand. Typically this requires an iterative procedure for coupling the Navier-Stokes flow in the bulk and the interfacial motion.

In Chapter 2, we described the diffuse-interface model and our AMPHI package for computing interfacial flows. At the beginning of the current project, we did attempt to apply AMPHI to the selective withdrawal problem, but encountered problems with numerical resolution. The diffuse-interface model relies on an accurate resolution of the interface, and on the assumption that the interfacial profile remains more or less at the equilibrium state such that the interfacial tension remains a constant [34]. However, when subject to strong flows, the diffuse interface is liable to being spread and distorted. In the present problem, the flow near the tip is highly elongational and induces strong distortions to the diffuse interface. We found that to capture the local curvature accurately would require an exceedingly thin interface and a prohibitive number of grid points. Thus, the diffuse-interface approach was unfeasible for the current problem.

Thus, we have turned to a sharp-interface formulation that deploys grid points directly on the interface, and tracks their motion as a result of the fluid flow and stresses. Our numerical code is based on an Arbitrary Lagrangian-Eulerian (ALE) scheme previously developed for simulating bubble growth in polymer foaming [124]. Detailed formulation of the method will be given in Section 4.2 below.

4.1.2 Extensional rheometry

We have hinted at the potential use of the selective withdrawal process to measure elongational viscosity of non-Newtonian fluids. The impetus for such an endeavor lies in the difficulty of such measurements using existing procedures. In this subsection we will give a brief background on extensional rheometry, which will serve as the backdrop for the results to be reported later in this chapter.

Compared with the shear viscosity, the extensional viscosity is very difficult to measure in the lab, because it is very difficult to produce a purely extensional flow with a constant extensional rate. Here, we will discuss three important types of extensional rheometers, filament stretching extensional rheometer (FiSER), capillary breakup (CaBER) extensional rheometer and the opposed-nozzle device. All of them generate a flow very close to purely

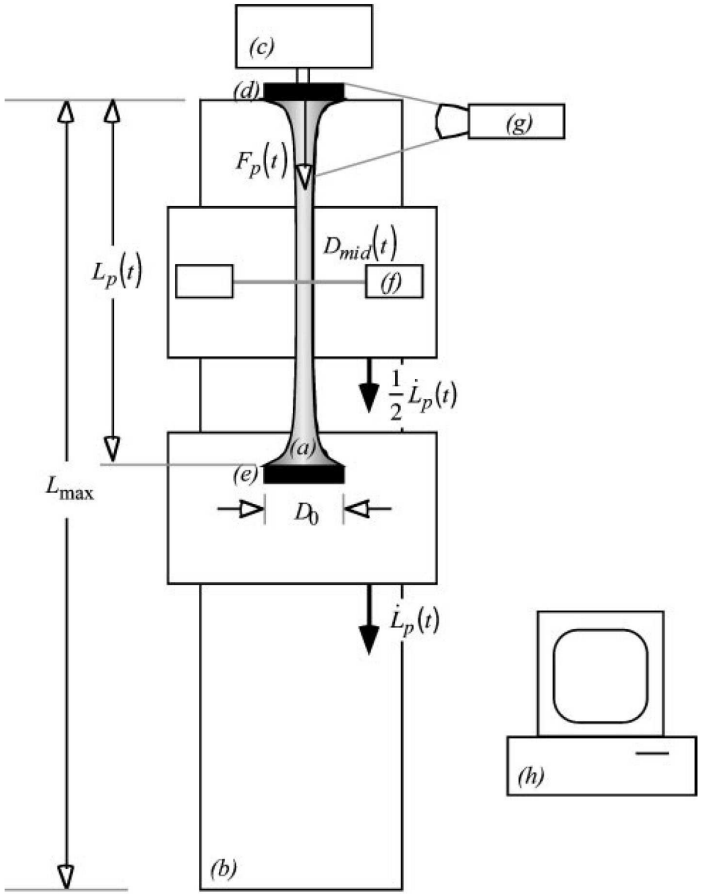

Figure 4.1: Schematic of the filament stretching extensional rheometer (FiSER). (Reproduced from Anna et al. 2001 [7]) a) fluid filament, b) linear motor with one or two moving plates, c) force transducer, d) top endplate, e) bottom endplate, f) diameter sensor, g) optional camera for observing profile near endplate, and h) computer system for control and data acquisition.

extensional flow in a limited region. Figure 4.1 shows the setup of the filament stretching device [7]. A fluid cylinder is placed between two end plates. When the end plates move apart exponentially, the fluid experiences straining in the middle of the filament which is approximately uniaxial elongation at a constant rate. The force balance on the fluid gives:

$$\langle \tau_{zz} - \tau_{rr} \rangle + \frac{1}{2}\langle \tau_{rr} - \tau_{\theta\theta} \rangle + \frac{1}{2}\langle r\tau_{rz} \rangle' = \frac{F}{\pi R^2} - \frac{\rho g V_0}{2\pi R^2} - \frac{\sigma}{R}(1 + RR'') - f, \tag{4.1}$$

with the 4 terms on the right-hand-side being due to the force on the end plate, gravity, surface tension and inertia:

$$f = \rho \left[\frac{1}{R^2}\frac{d^2}{dt^2}\int_0^{L/2} zR^2 dz - \frac{R\ddot{R}}{4} \right]. \tag{4.2}$$

In these two equation, V_0 is the initial volume of the liquid filament and $V_0 = \pi R_0^2 L_0$. Assuming uniaxial elongation, both the second and third terms on the left side of Eq. (4.1) are negligible. Also, under a constant strain rate, the second part of the inertia term is 0 [125]. Now we have:

$$\bar{\eta}^+ \dot{\epsilon}_0 = \langle \tau_{zz} - \tau_{rr} \rangle = \frac{F}{\pi R^2} - \frac{\rho g V_0}{2\pi R^2} - \frac{\sigma}{R}(1 + RR'') - \rho \left[\frac{1}{R^2} \frac{d^2}{dt^2} \int_0^{L/2} z R^2 dz \right]. \qquad (4.3)$$

With the end plates moving apart at a prescribed velocity, the extensional rate of the flow will be approximately constant, and can be measured from the thinning diameter of the fluid cylinder. This, together with the force on the end plate, allows one to calculate the extensional viscosity. The FiSER is a very useful extensional rheometer, but with limitations. One is that the liquid has to be sufficiently viscous as to form a smooth and stable filament when stretched. Typically this requires the zero-shear viscosity to be from 10 to 10^3 Pa·s. Another issue is the disturbance of the end plates. The flow is not elongational near the plates, and there is a de-adhesion instability at large stretching rates [126].

The CaBER is similar to FiSER in that a fluid cylinder is formed between two end plates. However, in this case it is formed by the two plates separating abruptly to a prescribed distance. Then the capillary thinning of the fluid cylinder is recorded until breakup under the combined action of surface tension and extensional force. From the balance between these forces, one can back up the extensional viscosity from the temporal change of the cylinder diameter [127, 128]. Compared with FiSER, CaBER can handle fluids with relatively low viscosity. But both measure an "elongational stress growth viscosity" [18], which is the instantaneous elongational viscosity as a function of time or strain. Normally, it is difficult to reach steady-state stretching in terms of the stress growth.

Figure 4.2 shows the setup of the opposed-nozzle device. Two opposed nozzles are aligned in the fluid and suck it out at the same rate. This creates a roughly extensional flow area between the nozzles. The elongational rate is estimated from the flow rate, and the stress from the torque on one of the nozzles. Then the elongational viscosity can be estimated. Note, however, that the flow is not truly homogeneous; In the central part near the stagnation point, the fluid experiences higher strain than farther away from it. Typically, a nominal extensional rate $\dot{\epsilon}_a$ is defined from the flow-rate of suction Q:

$$\dot{\epsilon}_a = \frac{2Q}{\pi R^2 d}, \qquad (4.4)$$

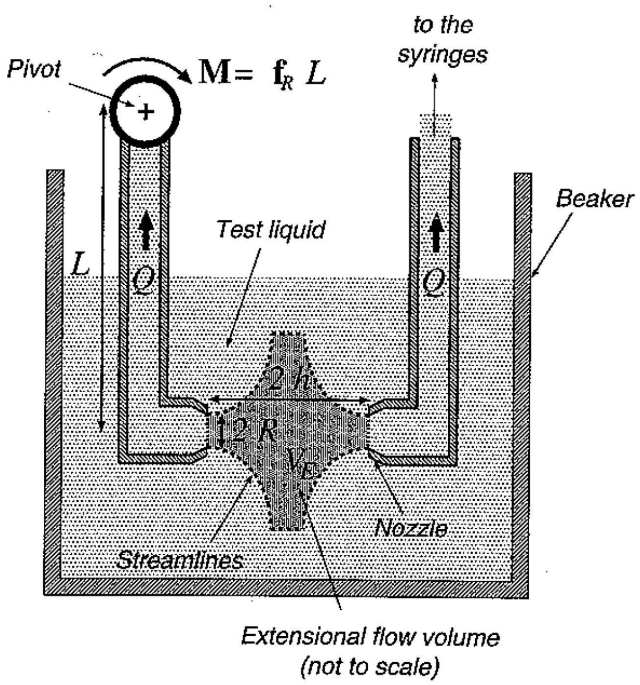

Figure 4.2: The opposed-nozzle extensional rheometer. The shaded region between the nozzles is where the flow is approximately extensional. [8]©Springer Berlin / Heidelberg

where d is the separation between the nozzles. Assuming that the torque M is due to the normal stress difference at the nozzles, we write

$$\tau_{11} - \tau_{22} = \frac{M}{L\pi R^2}. \tag{4.5}$$

Now an apparent extensional viscosity can be obtained:

$$\bar{\eta}_a = \frac{\tau_{11} - \tau_{22}}{\dot{\epsilon}_a} = \frac{Md}{2LQ}. \tag{4.6}$$

The advantage of the opposed-nozzle device is that it applies to low-viscosity fluids such as dilute polymer solutions. The disadvantage is that the flow field is relatively complex, and we have to use a nominal, rather than local, strain rate. Besides, the different streamlines entering the nozzles have different strain histories, and it is not clear whether the measured $\bar{\eta}_a$ can be taken as that corresponding to the steady-state stretching at the nominal $\dot{\epsilon}_a$. These introduce uncertainties into the final result and compromise the accuracy. Even for Newtonian fluids, the opposite nozzle device can give a Trouton ratio that deviates much

from 3 [8, 58]; typical values range from 2–4 [129] to order 10 [130] and even 100 [131]. Contraction flow is another method for measuring $\bar{\eta}$ for low-viscosity liquids. But the flow field is even more complex than in the opposed nozzle setup and deviates more from pure and homogeneous extension. The interpretation of the result is accordingly more uncertain [132]

To sum up, we can measure the extensional viscosity of highly viscous liquids with relative ease and high accuracy using filament stretching. For low-viscosity fluids, on the other hand, an equally satisfactory method does not seem to be available yet. There is a need for exploring novel flow setups for measuring the extensional viscosity of low-viscosity liquids. It is against this backdrop that we consider the potential of selective withdrawal as a process that may be developed into an extensional rheometer.

4.2 Numerical methodology

For our simulations, we have adapted an Arbitrary Lagrangian-Eulerian (ALE) scheme developed for simulating bubble growth in polymer foaming [124]. We use a sharp-interface algorithm to simulate the process of selective withdrawal. In this algorithm, the governing equations are solved in a 3D axisymmetric geometry with triangular mesh, which moves and deforms by the arbitrary Lagrangian-Eulerian scheme. We use the standard Galerkin formalism to discretize the governing equation.

4.2.1 Arbitrary Lagrangian-Eulerian scheme

In the arbitrary Lagrangian-Eulerian (ALE) scheme, we employ two coordinates. One is the Eulerian coordinate ($\boldsymbol{x}$) and the other is a quasi-Lagrangian coordinate ($\boldsymbol{X}$) fixed on the moving mesh. On boundaries, including the free surface, the mesh velocity conforms to that of the boundary with an optional slip in the tangential direction. As the boundary nodes move, the mesh in the interior deforms smoothly according to a Laplace equation:

$$\nabla \cdot (k^e \nabla \boldsymbol{v}_m) = 0, \tag{4.7}$$

where k^e is the inverse of the local element volume [67, 133]. Because we also have

$$\boldsymbol{v}_m(\boldsymbol{x}, t) = \frac{\partial \boldsymbol{x}(\boldsymbol{X}, t)}{\partial t}, \tag{4.8}$$

we can update the mesh position every time step. As all the variables are defined at the moving grid, the Lagrangian derivatives need to be computed as

$$\frac{d}{dt} = \frac{\partial}{\partial t} + \boldsymbol{v} \cdot \nabla = \frac{\delta}{\delta t} + (\boldsymbol{v} - \boldsymbol{v}_m) \cdot \nabla, \tag{4.9}$$

where $\frac{\delta}{\delta t}$ is the referential time derivatives defined on the moving grid point: $\frac{\delta}{\delta t} = \frac{\partial}{\partial t}|_{\boldsymbol{X}\text{fixed}}$.

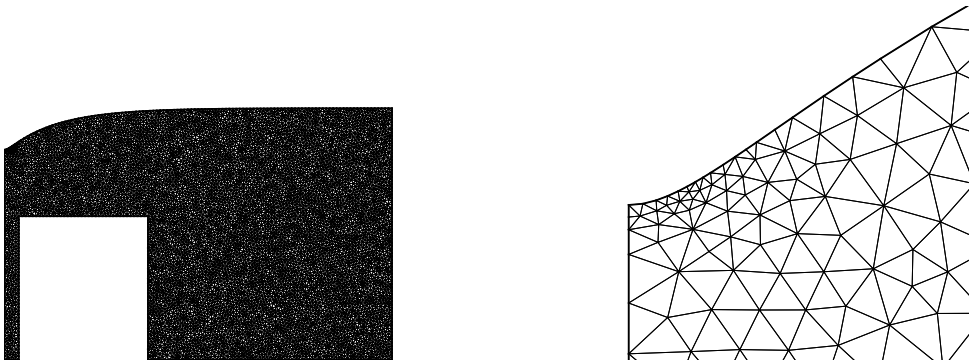

(a) (b)

Figure 4.3: A typical mesh used in our simulation. (a) The entire computational domain. (b) Magnified view of the mesh near the free surface. Note that the interface is marked by grid points, and the resolution is refined near the tip of the interface.

4.2.2 Finite element method

We use the finite element method to solve the governing equation. Initially, the outer boundary is divided into segments of size h_0. Then we use Delaunay triangulation to generate a uniform bulk mesh. In the simulation, mesh refinement is needed because the deformation of free surface. We use the curvature as the criteria to determine the refinement. We will refine the mesh at large curvature and coarsen it at small curvature. As the result of this, each boundary segment subtends to roughly the same center angle. In time, the moving boundary tends to distort the mesh and compromise its quality. We design a quality criterion based on the aspect ratio of the elements, and will re-mesh the computational domain when the criterion is met. A typical mesh is shown in Fig. 4.3.

In the standard Galerkin formalism, we seek the weak solution $(\boldsymbol{v}, p, \boldsymbol{\tau})$ using the test functions $(\tilde{\boldsymbol{v}}, \tilde{p}, \tilde{\boldsymbol{\tau}})$, and in their weak form the governing equations become:

$$\int_\Omega \left\{ \left[\rho \left(\frac{\delta \boldsymbol{v}}{\delta t} + (\boldsymbol{v} - \boldsymbol{v}_m) \cdot \nabla \boldsymbol{v} - \boldsymbol{g} \right) \right] \cdot \tilde{\boldsymbol{v}} + (-p\boldsymbol{I} + \boldsymbol{\tau}) \cdot \nabla \tilde{\boldsymbol{v}} \right\} x \, d\Omega - S = 0, \quad (4.10)$$

$$\int_\Omega -(\nabla \cdot \boldsymbol{v}) \, \tilde{p} \, x \, d\Omega = 0, \quad (4.11)$$

$$\int_\Omega \left\{ \boldsymbol{\tau}_p + \lambda_H \left[\frac{\delta \boldsymbol{\tau}_p}{\delta t} + (\boldsymbol{v} - \boldsymbol{v}_m) \cdot \nabla \boldsymbol{\tau}_p - \boldsymbol{\tau}_p \cdot (\nabla \boldsymbol{v}) - (\nabla \boldsymbol{v})^{\mathrm{T}} \cdot \boldsymbol{\tau}_p \right] - \mu_p \left[\nabla \boldsymbol{v} + (\nabla \boldsymbol{v})^{\mathrm{T}} \right] \right\} \cdot \tilde{\boldsymbol{\tau}} x \, d\Omega = 0, \quad (4.12)$$

where x is the radial coordinate in the axisymmetric geometry and S is the surface integral of the stress boundary condition:

$$S = \int_{\partial\Omega} \boldsymbol{n}\cdot(-p\boldsymbol{I}+\boldsymbol{\tau})\cdot\tilde{\boldsymbol{v}}\, x\, dS = \int_{\partial\Omega_i} (-p_a+\kappa\sigma)\boldsymbol{n}\cdot\tilde{\boldsymbol{v}}\, x\, dS + \int_{\partial\Omega_\tau} \boldsymbol{n}\cdot(-p\boldsymbol{I}+\boldsymbol{\tau})\cdot\tilde{\boldsymbol{v}}\, x\, dS, \quad (4.13)$$

where $\partial\Omega_i$ is the free surface subject to ambient pressure p_a and $\partial\Omega_\tau$ is part of the boundary of the computational domain on which stress boundary condition are given. In addition, we also have the weak form of the Laplace equation for the mesh velocity:

$$\int_\Omega k^e \nabla \boldsymbol{v}_m \cdot \nabla\tilde{\boldsymbol{v}}_m\, d\Omega = 0. \quad (4.14)$$

The resulting nonlinear algebraic equations are solved by Newton's method with delayed updating of the Jacobian. Within each Newton iteration, the linear system is solved by iterative methods such as the preconditioned generalized minimum residual (GMRES) scheme or the biconjugate gradient stabilized (BICG-STAB) algorithm. More details of the algorithm and validation with mesh refinement may be found in Yue *et al.* [124]. Following their mesh setup, we use a uniform initial mesh with the mesh size $0.2R$. Subsequent refinement takes place automatically in high-curvature regions at the interface. Prior numerical tests show that this level of mesh size controls the discretization errors under 0.1%.

As for most viscoelastic flow simulations, our computation is limited by the "high-Weissenberg number problem", i.e., the difficulty in achieving convergence at high Weissenberg numbers (or Deborah number De in our nomenclature). This is typically because sharp gradients of the polymer stresses arise that cannot be adequately resolved numerically. Algorithmically, large errors in the polymer stress gradients make the iteration very difficult to converge. As a result, the code blows up. In our computations, such gradients tend to appear at the lips of the suction tube, where the shear-rate is high and varies rapidly in space. To alleviate this problem, we introduced a rounding of the inner corner of the lip, with a radius of 1% of the tube radius. This allows us to improve the maximum De from 4.1 to 50.2. This is still below the experimental values of the last chapter, and will pose some inconvenience in comparing the two.

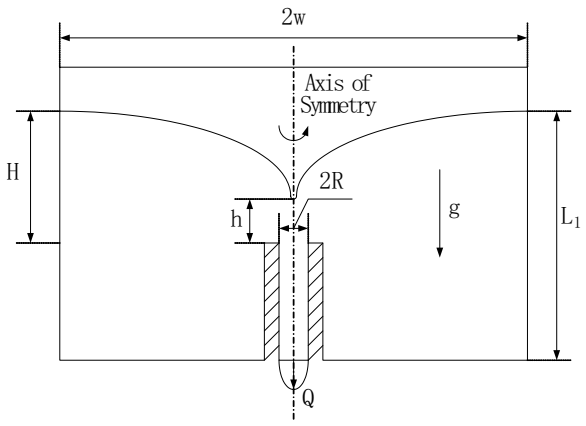

Figure 4.4: Schematic of the flow geometry. The computational domain is the right half of the meridian plane shown.

4.3 Setup of the computational problem

Figure 4.4 shows the axisymmetric geometry of our computational domain. The air-liquid interface is assumed to be a free surface subject to a constant atmospheric pressure. Upon start of the suction, the free surface dips in the center. Fluid enters from the bottom of the domain, where zero-stress boundary condition is imposed. If the flow rate Q is not too large, a steady state is reached (subcritical regime). On the side walls, no-slip boundary condition is used. We have the following physical parameters: flow rate Q, interfacial tension σ, liquid viscosity μ, density ρ and the gravitational acceleration g. The geometric parameters are the tube radius R, radius of the tank w, and the two heights L_1 and H specifying the position of the free surface at the side wall relative to the tip of the tube and the bottom of the tank. We will choose large values for w and L_1 such that upon start of the flow, the liquid surface at the side wall changes little. Then H and Q are control parameters that can be prescribed. However, the position of the tip, measured by h, is a "dependent variable", as is the surface curvature κ at the tip.

If the liquid is viscoelastic, we use the Giesekus model to represent its rheology, which strikes a balance between relative simplicity and realistic rheological prediction. For some computations we have also used the simpler Oldroyd-B model. Further information on these models can be found in textbooks [18]. The Giesekus model adds 3 more parameters:

the relaxation time λ_H, the mobility factor α, and the solvent viscosity ratio μ_s. Thus, in addition to the length ratios H/R, L/R and W/R, we have six dimensionless groups:

$$Ca = \frac{Q\mu}{\sigma R^2} \quad \text{(Capillary number)}, \tag{4.15}$$

$$Bo = \frac{\rho g R^2}{\sigma} \quad \text{(Bond number)}, \tag{4.16}$$

$$Re = \frac{\rho Q}{\mu R} \quad \text{(Reynolds number)}, \tag{4.17}$$

$$k = \frac{\mu_s}{\mu} \quad \text{(viscosity ratio)}, \tag{4.18}$$

$$De = \frac{\lambda_H Q}{R^3} \quad \text{(Deborah number)}, \tag{4.19}$$

$$\alpha \quad \text{(mobility factor)}, \tag{4.20}$$

where $\mu = \mu_p + \mu_s$. In the experiments, the flow Reynolds number is typically very small. In our simulation, therefore, we keep Re below 10^{-3} so that the flow is essentially inertialess. In addition, w and L will be large enough so as to avoid any influence from the boundary conditions on the side wall and the bottom of the domain. Thus, we have only one important length scale H/R and a total of six dimensionless parameters in our system. These may be varied, say, by changing Q, H, g, λ_H, μ_s and α.

As the critical state is approached, the interface deforms into a cusp with the local curvature increasing without bound. This causes the local length scale to decrease toward zero. In our code, the mesh generator reacts to the increasing curvature by refining the local grid. But eventually the mesh fails to accurately represent the small length scales near the tip. The surface near the tip becomes jagged and the value of curvature becomes very large or negative. Then the code diverges and the simulation aborts. Therefore we cannot simulate the transition from subcritical to supercritical state. In its stead, we employ an artificial criterion for determining the critical point in the numerical simulation. With moderately large H, the solution is subcritical and a steady-state free surface shape is reached. With decreasing H and a fixed Q, the steady-state surface becomes more and more deformed, until at one point, no steady solution can be obtained, and the code blows up. This is taken to be the critical H^* corresponding to the Q value. From experimental observations, the tip curvature increases precipitously toward the critical condition. Thus, the fact that the numerically computable maximum tip curvature depends on mesh resolution and is in some sense "arbitrary" does not appreciably affect the critical H^* value.

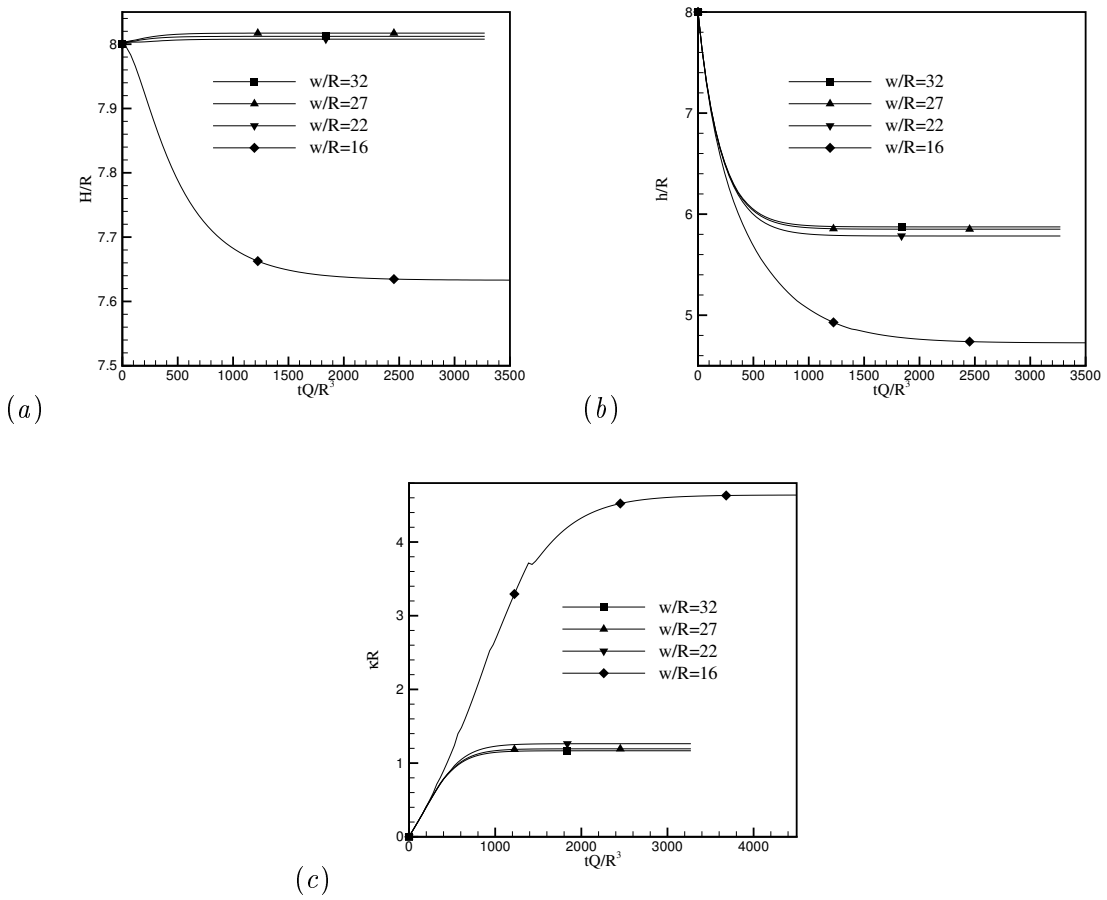

Figure 4.5: The side-wall effect in the simulation. (a) Variation of the water level at the side wall after the flow starts for 4 values of the tank radius w. (b) The position of the tip of the interface indicated by the vertical distance h from the tube. (c) Variation of the tip curvature. The wiggle on the curve for $w = 16R$ is a numerical artifact due to remeshing.

4.4 Newtonian results: benchmarking by experiments

The experiment of du Pont and Eggers [6] on air-oil selective withdrawal provides an ideal benchmark for our numerical algorithm. Thus, before going to viscoelastic simulations, we compare our predictions for Newtonian fluids with the experimental measurements as a validation of the former. du Pont and Eggers [6] used a tank of square cross-section, with the side $w = 27R$ being wide enough so the results are unaffected by the side walls. Similarly, we want to ensure that our domain is wide enough for the wall effects to be negligible. For this purpose, we have tested 4 values of the tank radius w, and Fig. 4.5 plots the temporal

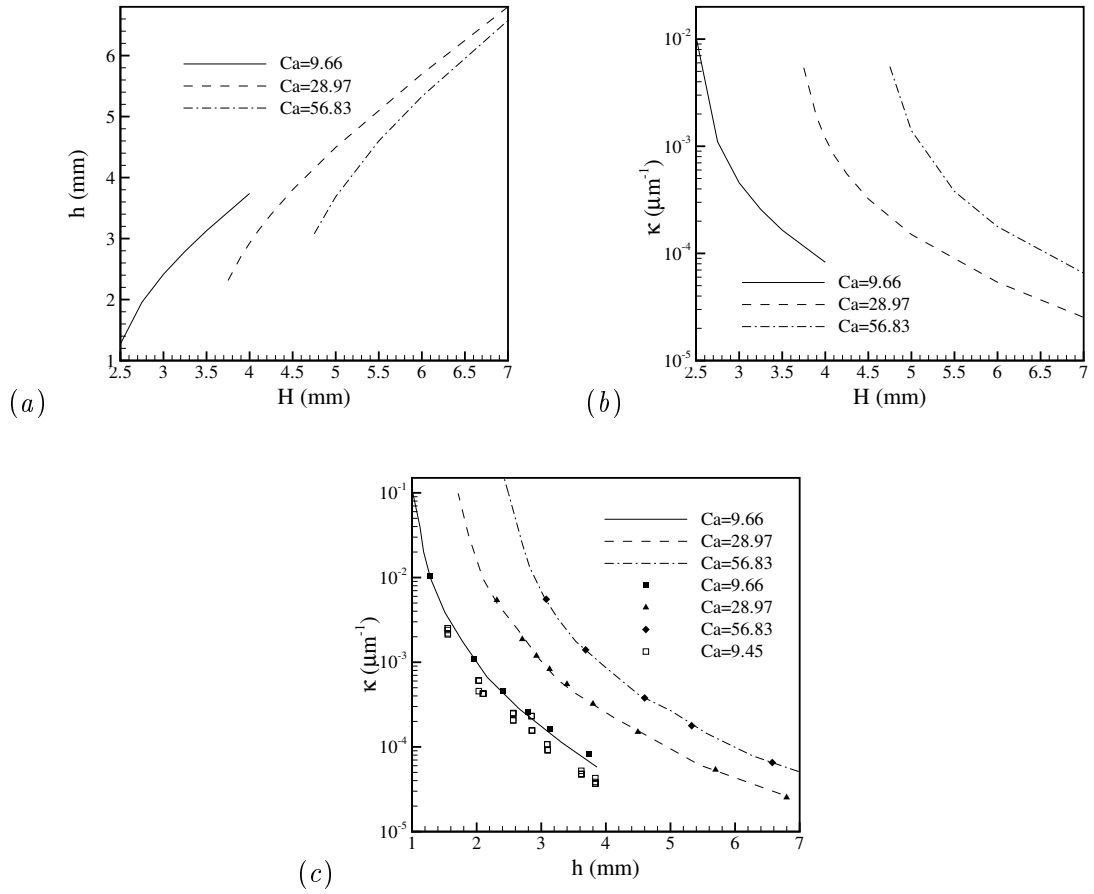

Figure 4.6: Steady-state solutions for Newtonian fluids at three Ca values. (a) The tip position h as a function of H. For larger H values, the interface hardly deforms and $h = H$. (b) The tip curvature κ. (c) Comparison between our calculations (filled symbols), our experiment (open symbols) and the experiment of du Pont and Eggers [6] (lines). The capillary number Ca is varied through Q. The Bond number is fixed at $Bo = 0.112$.

variation of the water level at the side wall and the position and the curvature at the tip of the interface for each w value. When the width is large enough ($w \geq 27R$), the change of the height H is only about 0.1% of the initial height. So we could neglect this change and assume the fluid level at the side wall does not change during the interfacial evolution. Moreover, Fig. 4.5(b) and (c) tell us that the side wall exerts little effect on the interface at the center when w is large enough. So we have chosen to use $w = 27R$ for all subsequent computations.

Figure 4.6 shows our simulation results for Newtonian fluids and compares them with the experimental data for the air-oil system of du Pont and Eggers [6] and our own experiment

described in the last chapter. All material parameters are matched between the three studies. Each point in Fig. 4.6 represents a steady state, and the curves are generated by varying H for a fixed flow rate Q (or Ca value). First, there is nearly perfect agreement between our simulation and the experiments. Note that we tuned our computations to match $Ca = 9.66$ in [6]. But our experimental control is such that we reached a slightly lower $Ca = 9.45$. Accordingly the tip curvature is slightly below the others in Fig. 4.6(c). Second, a higher H leads to less deformation at the tip, with a smaller κ, simply because the interface is farther from the tube opening. Finally, a larger flow rate draws the interface closer to the tube (smaller h) with a more pointed tip (greater κ). In the parameter ranges tested, the numerical and experimental data seem to suggest a critical condition of $\kappa \to \infty$ at a finite h value. But this is actually unattainable for the low air-liquid viscosity ratio considered [99]. This has been discussed at length in Chapter 3. To sum up this section, the ALE algorithm and computer program have been validated by the agreement with experiments, and thus we are ready to turn to the viscoelastic problem.

4.5 Viscoelastic results

4.5.1 Interfacial deformation in subcritical regime

Figure 4.7(a) shows the steady-state free surface computed for the Giesekus fluid at a fixed $Ca = 28.97$ and different H values. As expected, the interface becomes more deformed with lowering H. The lowest curve for $H/R = 8$ is the near the critical condition. For a smaller H, the steady state is lost; the tip of the surface continues to extend and the simulation becomes non-convergent. As a comparison, we include in Fig. 4.7(b) the steady-state surfaces for Newtonian fluids. The surface shape is qualitatively similar in both cases. However, for the same H values the surface is more deformed for the Giesekus fluid. This is thanks to the viscoelastic elongational stress. Also notable is the fact that the Newtonian surface apparently deforms to a greater extent in terms of the hump height $H - h$. Lacking a true physical critical state, the Newtonian computation breaks down when the tip curvature becomes too large to be resolved numerically. Thus, more deformed steady states may be obtained for the Newtonian fluid in Fig. 4.7(b). The lowest curve at $H/R = 7.3$ marks the limit of numerical convergence. In contrast, the lowest curve for the Giesekus fluid, at

(a) (b)

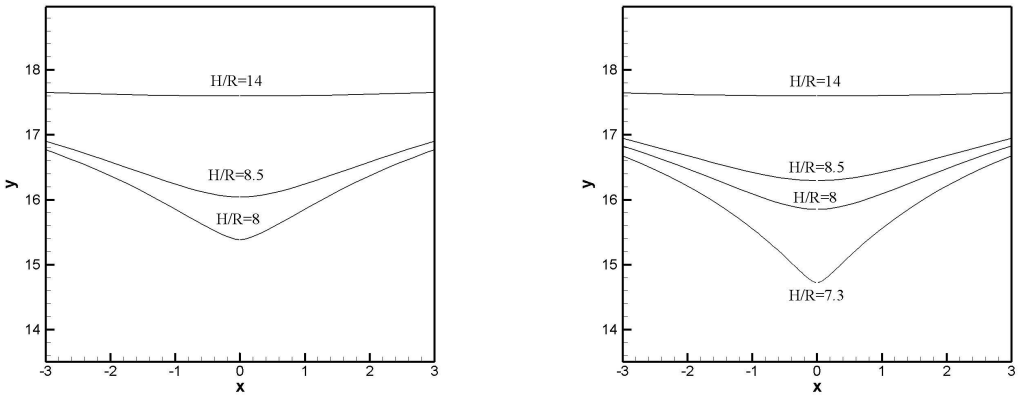

Figure 4.7: The steady-state interface profiles in the subcritical regime at several values of the liquid level H. (a) The Giesekus fluid with mobility factor $\alpha = 0.1$, viscosity ratio $k = 0.7$ and Deborah number $De = 12.29$. (b) A Newtonian fluid.

(a) (b)

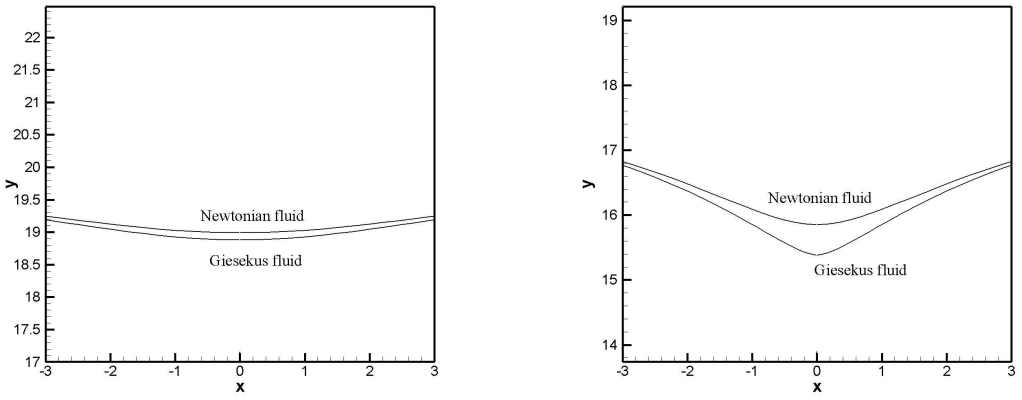

Figure 4.8: Comparison between Newtonian and Giesekus interfaces at the same flow conditions. $Ca = 28.97$. For the Giesekus fluid, $\alpha = 0.1$, $k = 0.7$ and $De = 12.29$. (a) $H/R = 10$; (b) $H/R = 8$.

$H/R = 8$, represents the closest steady-state solution to the critical condition that we have simulated.

Figure 4.8 shows more explicitly that the viscoelasticity enhances interfacial deformation, reducing h and increasing κ at the same H and Ca. For $H/R = 10$, the free surface is relatively flat and the deformation is mild. More pronounced deformation obtains for $H/R = 8$, where the Giesekus surface develops a rather pointed tip; it is very close to the critical state. In both plots, the free surface does not differ much between the Newtonian and Giesekus fluids away from the tip. At the tip, the Giesekus surface deforms more because of a local concentration of additional elongational stress.

Figure 4.9 shows contours of the polymer stresses near the free surface for the Giesekus fluid at steady state. The tensile stress τ_{zz} dominates the other components, and is especially large in the region directly below the tip of the interface. That is where the flow is essentially uniaxial elongation. Note also the localization of the elongational stress. The distribution of polymer stresses underlies our understanding of the viscoelastic effect in this flow geometry, and confirms the explanation advanced in the above.

A more quantitative study of the viscoelastic effect is given in Fig. 4.10, which plots the tip position h and curvature κ as a function of the Deborah number De for Giesekus and Oldroyd-B fluids. For both models the results are qualitatively the same. As De increases, the tip moves progressively downward toward the suction tube and the hump height $H - h$ increases. Meanwhile, the tip curvature κ increases monotonically. Both indicate increasing elongational force in the liquid that pulls the interface down. For larger De, the tip curvature tends to increase without bound. Numerically, we observe breakdown of the computation before a steady interfacial profile can be established. As indicated before, this is taken to be the attainment of the critical state, to which we will return in the next subsection. For the parameters used, the largest De we have computed is $De = 4.1$ for Oldroyd-B fluid and 12.3 for the Giesekus fluid. As is well known, the nonlinear term softens the strength of elastic stresses in the Giesekus model. Consequently, the tip curvature is smaller than the Oldroyd-B result at the same De, as is the depth of the interfacial dip $H - h$. The critical state is also delayed to much higher De.

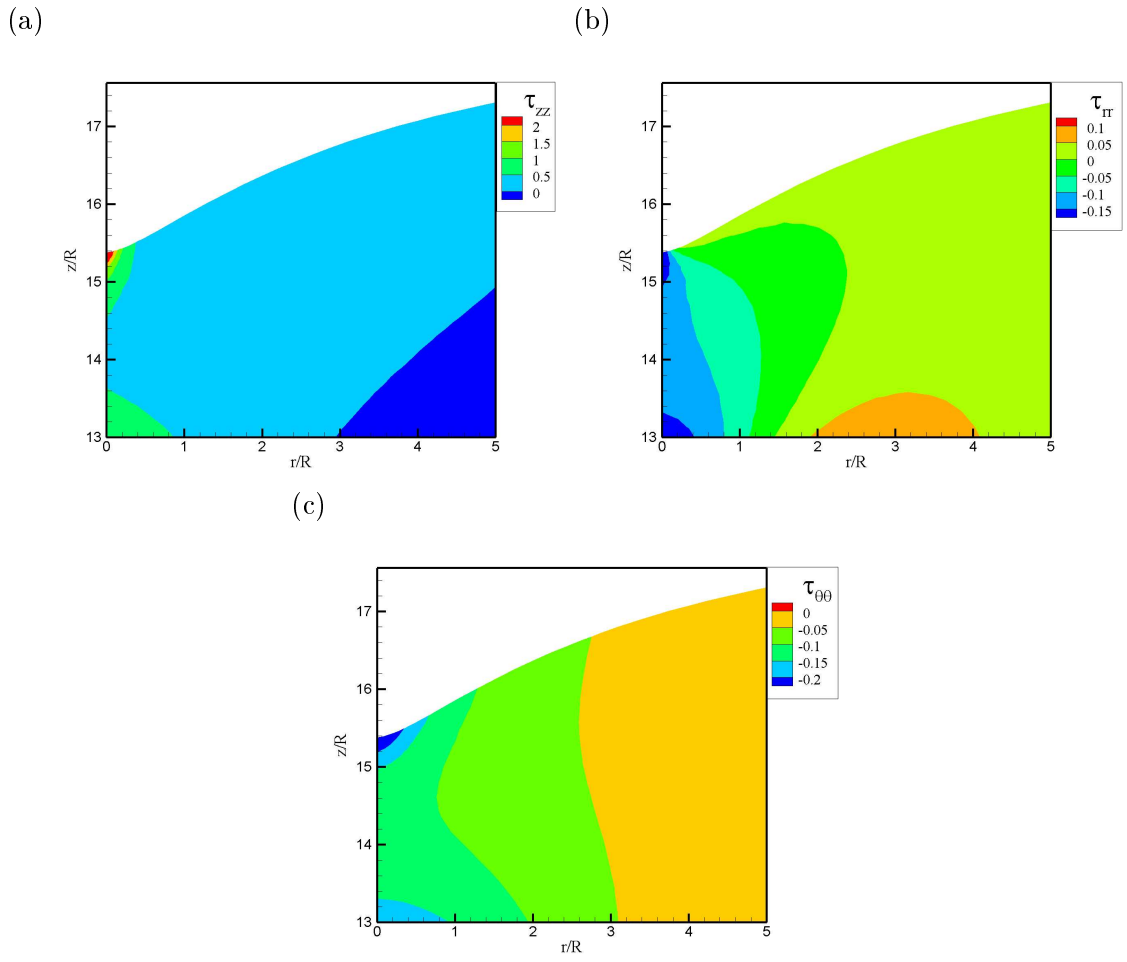

Figure 4.9: Contours of the polymer stress components τ_{zz}, τ_{rr} and $\tau_{\theta\theta}$ near the steady-state surface for $H/R = 8$ in the last figure. $Ca = 28.97$, and the fluid is Giesekus with $De = 12.29$, $k = 0.7$ and $\alpha = 0.1$.

Figure 4.11 compares the steady-state free surface between the numerical simulation and experiment. In this comparison, De of the simulation is slightly smaller than the experimental value; no higher De can be computed because of the stress boundary layer near the orifice of the tube. The experimental free surface is more deformed than the numerical prediction; it has a larger curvature on the tip and a smaller h. The difference of $\chi = \frac{H-h}{R}$ is roughly 10%. Moreover, the free surface deformation is more localized for the experiment than the numerical simulation. Possibly these differences stem from the higher De in the experiment. Another potential explanation is the Giesekus model not being able to reflect all aspects of the fluid's rheology.

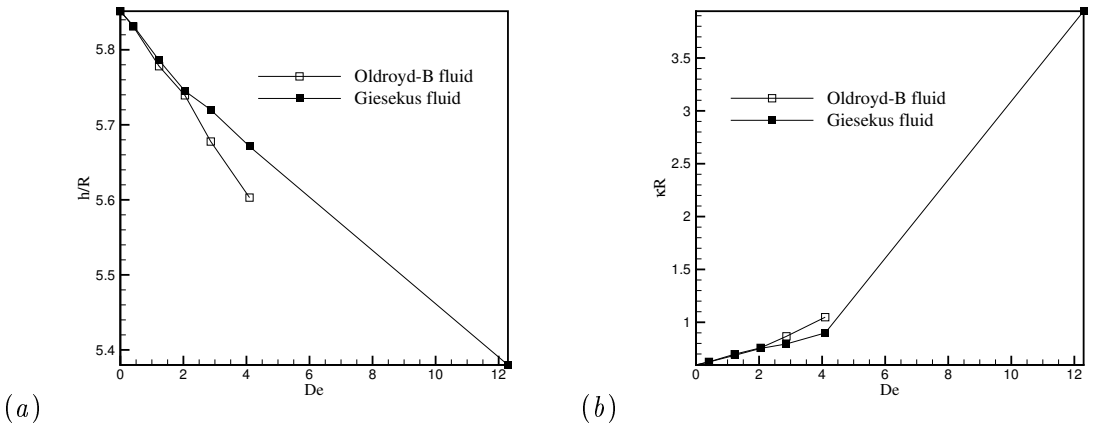

(a) (b)

Figure 4.10: The effect of viscoelasticity, measured by the Deborah number De, on (a) the tip position h and (b) the tip curvature κ, for Oldroyd-B and Giesekus fluids. The following parameters are fixed: $Ca = 28.97$, $Bo = 0.112$ and $H/R = 8$. For the Giesekus fluid, $\alpha = 0.1$ and $k = 0.7$.

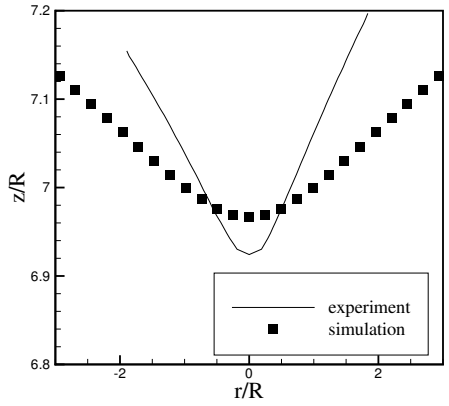

Figure 4.11: Comparison of the free surface between experiment and simulation. $Ca = 2.5$ and $H/R = 7.36$. For the experiment, SE fluid is used and $De = 55.25$. For the simulation, Giesekus model is used: $De = 50.2$, $k = 0.2$ and $\alpha = 0.2$.

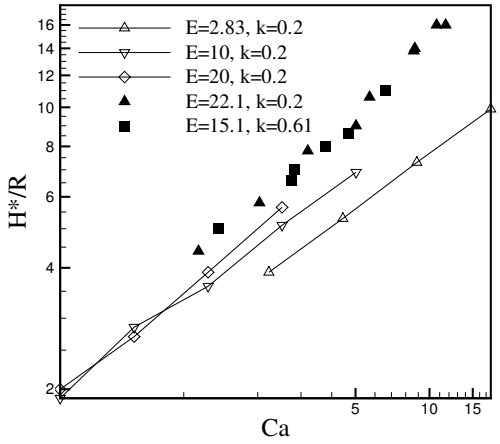

Figure 4.12: The critical liquid level H^* as a function of Ca at various E values for the Giesekus fluid. In the plot, the line with open symbols are the data from simulation and the black symbols are the data from experiment.

4.5.2 Critical conditions

As described before, computationally the critical condition is defined as the loss of convergent steady solution when the tip curvature becomes too large to be resolved. In practice, this is approached by computing the steady solution for a series of decreasing H values, with the other parameters—De, Ca and rheological parameters—fixed. Thus, the critical condition is most conveniently marked by a threshold H^*, which is the average between the smallest H that gives a steady solution and the next H that does not. Unlike in the experiments, it is difficult to determine the critical h^* since near the critical point, h varies steeply with H. Taking the h value for the last steady solution for h^* is likely to be a gross overestimation. Therefore, we will only discuss the critical condition in terms of H^*.

Figure 4.12 plots the critical liquid level H^* for a range of Ca and five values of the elasticity number $E = De/Ca$. Numerical results show that H^* increases with Ca and E, in qualitative agreement with experimental observations (cf. subsection 3.6.2). As suggested in the last chapter, these trends reflect the fact that increasing either Ca or E leads to larger elastic stresses pulling down the interface. Thus the critical condition can be achieved for interfaces that are farther from the nozzle.

A more quantitative comparison with experimental data is hampered by subtleties in matching the parameters. Because of limitations in resolving the polymer stress gradient at the lip of the suction tube, the highest De achievable in the simulations is about 50.2. In comparison, the largest experimental De is over 200. As plotting in Fig. 4.12, the numerical data range to large Ca values for weakly elastic fluids with small E. For large E, we are limited to small Ca. The numerical data overlap but does not encompass the experimental data range. In addition, there is a slight mismatch of the viscosity ratio k between experiments and computations. This is because the computations had been done prior to most of the experiments using a k value corresponding to an earlier less accurate measurement of the solvent viscosity.

Nevertheless, there seems to be rather good agreement between the experimental and numerical data. This is reflected by the similar trend in the $H^*(Ca)$ dependence, which approximates straight lines in the log-log plot. Thus, both experimental and numerical data exhibit a power-law dependence on Ca. The index increases with E, and consistently across most numerical and experimental data sets. The outlier to this trend is perhaps the experiment with $E = 15.1$ (for the weakly elastic liquid of Chapter 3), whose H^* value rises above the numerical data set for $E = 20$. This is most probably due to the much larger solvent viscosity for this polymer solution $k = 0.61$, which provides an additional contribution to the pulling force below the interface.

Finally, we cannot simulate the supercritical state nor the hysteresis. In the experiment, the stability of the air jet depends on its small but non-zero mass and viscosity. In our computational setup, the air-liquid interface is treated as a free surface, with the air contributing no force on the interface aside from a constant ambient pressure. When we attempted to start the simulation with an initial condition having a thin air jet, it collapses momentarily and the code breaks down.

4.6 Measuring the elongational viscosity

4.6.1 Underlying assumptions

As mentioned briefly in the last chapter, a secondary motivation for studying selective withdrawal is to explore the possibility of using the process to measure the elongational viscosity of the liquid. This relies on two assumptions. First, the flow near the tip is mostly elongational. Second, the steady-state subcritical condition of the surface is maintained by a balance among the surface tension, the pressure and the elongational stress below the tip. These will allow us to back out the elongational stress at the tip of the interface from the interfacial position and curvature. Besides, the local strain rate near the tip must be obtained from the control parameters of the process. These will be explored through numerical computations supplemented by the experimental data of the last chapter.

(*a*) *Flow type*

Following Leal and coworkers [134], we use the *flow type parameter* to indicate how much of the deformation consists of extension and rotation:

$$\psi = \frac{\|\boldsymbol{D}\| - \|\boldsymbol{W}\|}{\|\boldsymbol{D}\| + \|\boldsymbol{W}\|}, \tag{4.21}$$

where $\boldsymbol{D} = (\nabla \boldsymbol{v} + \nabla \boldsymbol{v}^{\mathrm{T}})/2$ is the strain-rate tensor of the flow, and $\boldsymbol{W}$ is a modified vorticity tensor to maintain frame-indifference [134, 135]:

$$\boldsymbol{W} = \boldsymbol{\Omega} - \boldsymbol{O}, \tag{4.22}$$

where $\boldsymbol{\Omega} = (\nabla \boldsymbol{v} - \nabla \boldsymbol{v}^{\mathrm{T}})/2$ and $\boldsymbol{O}$ is the local rotation of the strain-rate tensor defined by

$$D\boldsymbol{e}_i/Dt = \boldsymbol{O} \cdot \boldsymbol{e}_i, \tag{4.23}$$

D/Dt being the material derivative and $\boldsymbol{e}_i$ the eigen-vectors of $\boldsymbol{D}$. Under this definition, $\psi = 1$ for purely extensional flow, 0 for simple shear and -1 for solid-body rotation.

Figure 4.13 and Fig. 4.14 depict ψ contours in the computed flow fields for a Newtonian and a Giesekus fluid, respectively. The blowup pictures show that in both cases, the flow is indeed very close to pure extension in the area below the tip of the interface, and our first assumption is confirmed. In fact, for the Giesekus fluid, the extensional area is wider than

(a) (b)

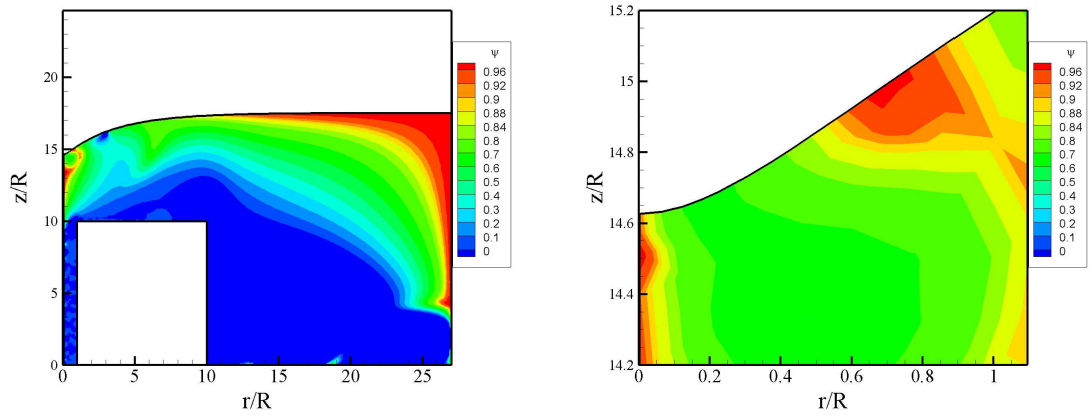

Figure 4.13: Contours of the flow type parameter ψ in the computed flow field for Newtonian fluid. Plot (b) shows details near the tip of the interface. In this case, $H/R = 7.5$, $Ca = 28.97$.

(a) (b)

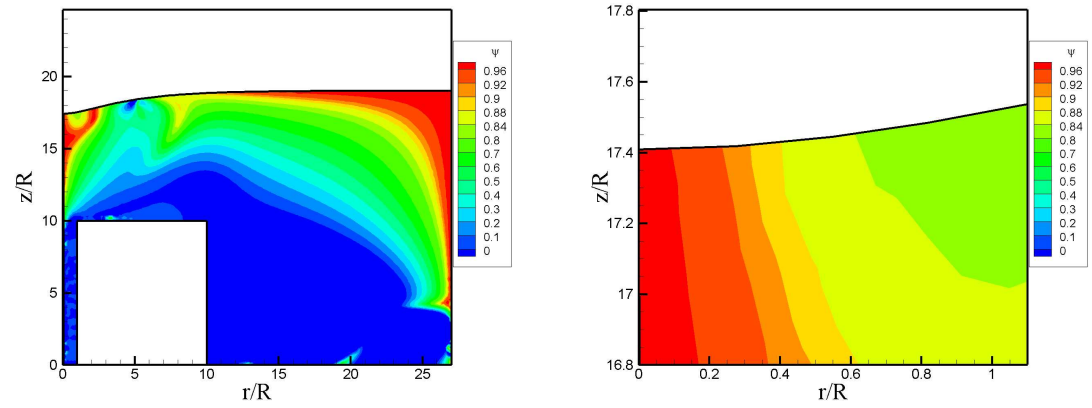

Figure 4.14: Contours of the flow type parameter ψ in the computed flow field for Giesekus fluid. Plot (b) shows details near the tip of the interface. In this case, $H/R = 9$, $Ca = 28.97$, $k = 0.7$ and $\alpha = 0.1$.

for the Newtonian fluid, probably due to the strong polymer stress akin to what produces tubeless siphon shown in Fig. 1.1.

(b) *Force balance*

Now let us consider the force balance on the free surface at the tip. On the air side, the normal stress is the atmospheric pressure p_a. On the liquid side, we have pressure p_1 and a

viscous or viscoelastic normal stress τ_{zz} in the vertical direction. Then there is the interfacial tension σ. Denoting the local curvature by κ, we modify the Laplace equation as such:

$$p_a = p_1 - \tau_{zz} + 2\sigma\kappa. \tag{4.24}$$

To determine p_1, we resort to the momentum equation in the horizontal (or radial in a cylindrical coordinate system) direction:

$$\rho\left(\frac{\partial v_r}{\partial t} + v_r\frac{\partial v_r}{\partial r} + \frac{v_\theta}{r}\frac{\partial v_r}{\partial \theta} - \frac{v_\theta^2}{r} + v_z\frac{\partial v_r}{\partial z}\right) = \left[\frac{1}{r}\frac{\partial(r\tau_{rr})}{\partial r} + \frac{\partial \tau_{\theta r}}{\partial \theta} + \frac{\partial \tau_{zr}}{\partial z} - \frac{\tau_{\theta\theta}}{r}\right] - \frac{\partial p}{\partial r}. \tag{4.25}$$

Because the flow is axisymmetric, $\tau_{\theta r}$ is zero. Neglecting the inertial terms for the moment, we have

$$\frac{\partial}{\partial r}(p - \tau_{rr}) = \frac{\tau_{rr} - \tau_{\theta\theta}}{r} + \frac{\partial \tau_{zr}}{\partial z}. \tag{4.26}$$

If the flow was uniform uniaxial elongation everywhere, τ_{rr} would equal $\tau_{\theta\theta}$ and τ_{zr} would be zero. Under this assumption we integrate from the tip ($r = 0$) radially outward to the wall ($r = w$):

$$p_1 - \tau_{rr}\mid_{r=0} = p_2 - \tau_{rr}\mid_{r=w}, \tag{4.27}$$

where p_2 is the pressure at the point on the wall that is level with the tip. Because the flow near the side wall is very weak, we assume $\tau_{rr}\mid_{r=w}$ is zero, and calculate p_2 from hydrostatics:

$$p_2 = p_a + \rho g(H - h). \tag{4.28}$$

From equations (4.24), (4.27),($\tau_{rr}\mid_{r=w} = 0$) and (4.28), we get the first normal stress difference as

$$N_1 = \tau_{zz} - \tau_{rr} = 2\sigma\kappa + \rho g(H - h). \tag{4.29}$$

If the local strain rate $\dot{\epsilon}$ is known, the extensional viscosity can be obtained as

$$\bar{\eta} = \frac{N_1}{\dot{\epsilon}} = \frac{2\sigma\kappa + \rho g(H - h)}{\dot{\epsilon}}. \tag{4.30}$$

The determination of $\dot{\epsilon}$ will be discussed below. Note that the derivation above applies equally to Newtonian and viscoelastic fluids.

This equation suffers from potential errors from three sources. The first is the neglect of the inertial terms. The second is the weak-flow assumption near the side wall in Eq. (4.27). And the third comes from setting $\tau_{rr} = \tau_{\theta\theta}$ and $\tau_{zr} = 0$ in Eq. (4.26) based on an assumption of

uniform uniaxial elongation. The first and second turn out to be insignificant; the Reynolds number is small ($10^{-4} \sim 10^{-3}$), and the shear and normal stresses at the side wall are indeed very small (0.1% of $\rho g(H-h)$). The third assumption is on less firm ground, and we will estimate the associated error in the following.

Integrating Eq. (4.26) without the assumption, we have

$$p_2 - (p_1 - \tau_{rr}) = \int_0^W (\frac{\tau_{rr} - \tau_{\theta\theta}}{r} + \frac{\partial \tau_{zr}}{\partial z}) dr. \tag{4.31}$$

Note that τ_{rr} is indeed equal to $\tau_{\theta\theta}$ on the axis of symmetry ($r = 0$) so that the integral does not diverge. Denoting $\tau_{ext} = \int_0^W (\frac{\tau_{rr}-\tau_{\theta\theta}}{r} + \frac{\partial \tau_{zr}}{\partial z}) dr$, we have the following in place of Eq. (4.30):

$$\bar{\eta} = \frac{N_1}{\dot{\epsilon}} = \frac{2\sigma\kappa + \rho g(H-h) - \tau_{ext}}{\dot{\epsilon}} \tag{4.32}$$

The magnitude of τ_{ext} should be dominated by the stress difference $\tau_{rr} - \tau_{\theta\theta}$ for small r. The τ_{zr} term should be insignificant because away from the centerline, where the flow contains considerable shear (cf. Fig. 4.13), the deformation rate dies out quickly. For a Newtonian fluid, $\tau_{rr} = 2\mu \frac{\partial v_r}{\partial r}$ and $\tau_{\theta\theta} = 2\mu \frac{v_r}{r}$. Toward the axis of symmetry, the $v_r(r)$ profile has to level to zero slope in a concave shape. Thus, we expect $\frac{\partial v_r}{\partial r} < \frac{v_r}{r} < 0$, $\tau_{rr} - \tau_{\theta\theta} < 0$ and $\tau_{ext} < 0$. Compared with Eq. (4.32), therefore, we expect Eq. (4.30) to underestimate the extensional viscosity. For viscoelastic fluids, the behavior of τ_{rr} and $\tau_{\theta\theta}$ depends on the specific constitutive equation, and it is difficult to anticipate the error of the simplied Eq. (4.30).

The amount of error can be quantified using numerical data for Newtonian and Giesekus fluids. After achieving a steady-state interfacial shape in simulations in the subcritical regime, the tip curvature κ, hump height $H - h$ and the local strain-rate $\dot{\epsilon}$ can all be extracted from the numerical solution. Then the "measured" $\bar{\eta}$ from Eq. (4.30) may be compared with the true elongational viscosity of the fluid. In particular, for Newtonian fluids, the elongational viscosity is simply $\eta_n = 3\mu$, and Fig. 4.15 illustrates the error of Eq. (4.30). Over the entire parameter space comprising Ca, Bo and H/R, the results confirm our estimation above that Eq. (4.30) *underestimates* the elongational viscosity. But the magnitude of the error is within 10% for the parameter ranges covered. Considering that

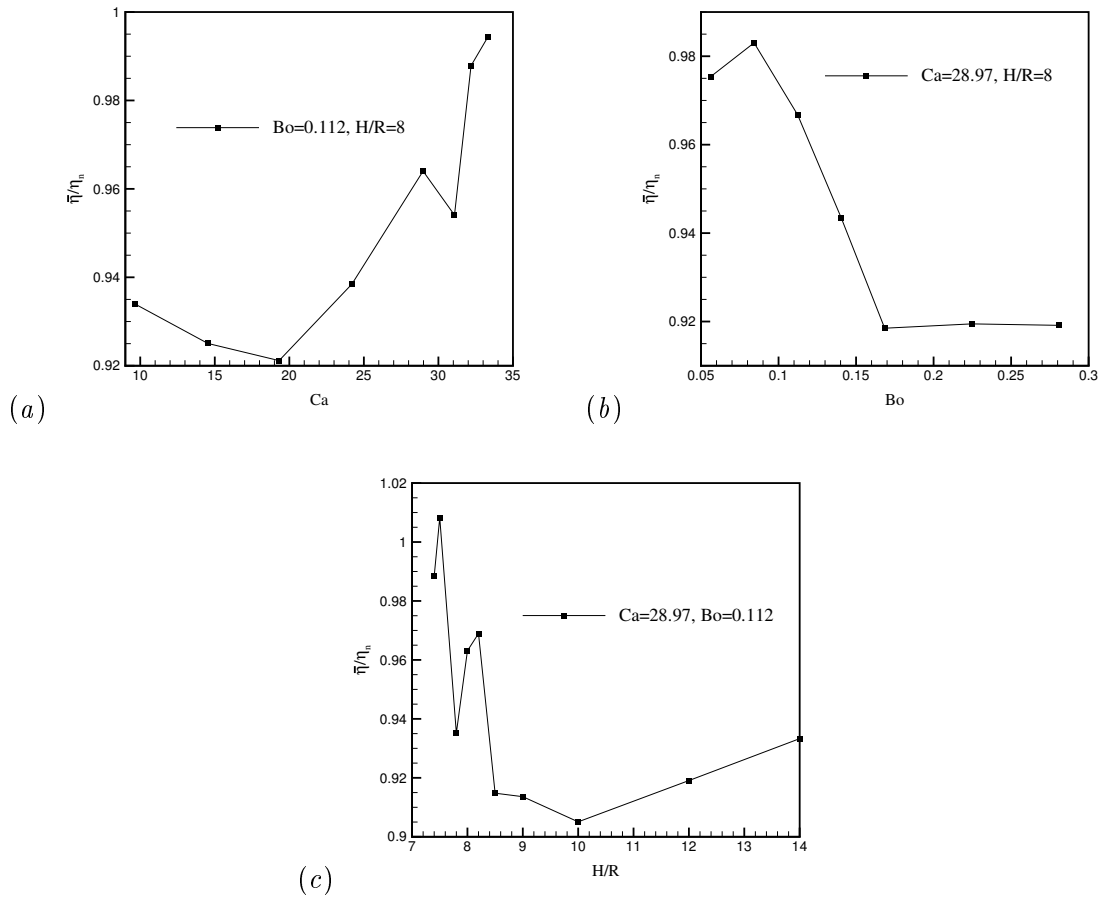

Figure 4.15: Testing our scheme of estimating the extensional viscosity for Newtonian fluids. The "measured" $\bar{\eta}$, scaled by the known η_n, is plotted against various parameters. (a) the plot between $\bar{\eta}/\eta_n$ and Ca. (b) the plot between $\bar{\eta}/\eta_n$ and Bo. (c) the plot between $\bar{\eta}/\eta_n$ and H/R.

the opposed-nozzle rheometer easily suffers from errors of 100% for Newtonian fluids [8], the results in Fig. 4.15 are very encouraging.

A similar exercise has been carried out for a Giesekus fluid (Fig. 4.16). In this comparison, η_G is the exact extensional viscosity at steady-state elongation for Giesekus fluid [18]. Note first that now $\bar{\eta}$ is *overestimated* by Eq. (4.30); the neglected τ_{ext} turns out to be positive for the Giesekus fluid. Possibly this is because of a shear component of the deformation away from the axis of the symmetry, which is predominantly horizontal and tends to increase τ_{rr} relative to $\tau_{\theta\theta}$. This is particularly true for smaller H/R values in Fig. 4.16(b); as the tip gets closer to the nozzle, the region of extensional flow shrinks under the tip. For the

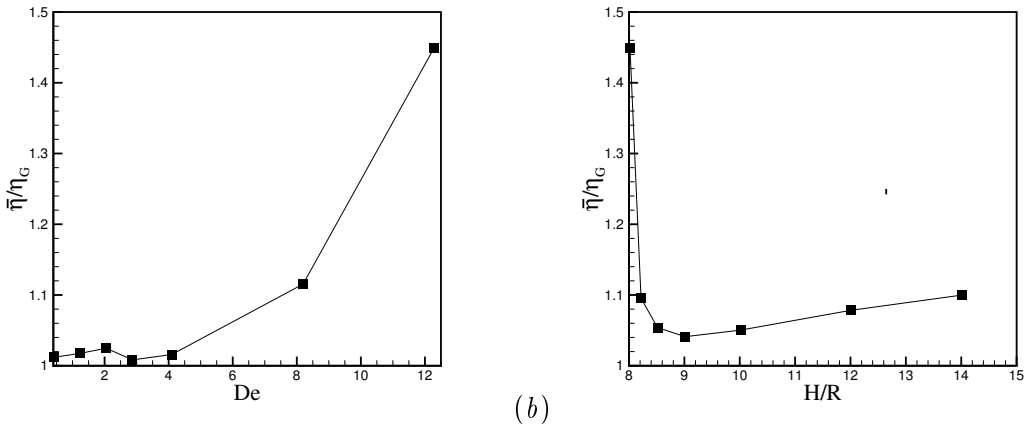

Figure 4.16: Testing our scheme of estimating the extensional viscosity for Giesekus fluids. The "measured" $\bar{\eta}$, scaled by the known η_G, is plotted against various parameters. (a) the plot between $\bar{\eta}/\eta_G$ and De. For all the cases in this plot, $H/R = 8$, $\alpha = 0.1$ and $k = 0.7$. (b) the plot between $\bar{\eta}/\eta_G$ and H/R. For all the cases in this plot, $De = 12.29$, $\alpha = 0.1$ and $k = 0.7$.

conditions shown, $H/R = 8$ is approaching the critical condition. Second, the magnitude of the error is again within 10% as long as the deformation is "not too strong", for a moderate $De < 6$ or $H/R > 17$. To sum up, the simplified force balance of Eq. (4.30) can be used with acceptable accuracy to back out the elongational viscosity from the surface force once the local strain rate is known.

(*c*) *Fully development of polymer stress*

In general, the polymer stress depends not only on the deformation rate but also on the stretching history of the polymer. An exception is when the polymer reaches steady-state stretching in an extensional flow at constant extensional rate. In our experiment, we assume that the polymer attains steady stretching at tip. Theoretically, this assumption is sound for all cases. The tip is a stagnation point in a pure extensional flow. The polymer will experience infinite residence time at that point. Experimentally, this is less certain because we calculate the curvature at the tip using the neighboring points. As the result of this, the extensional viscosity we get is the average value in that small region. The typical length of this region is $100\mu m$ as we mentioned before. With the numerical result, we could compute the total strain for the polymer going through this small domain. Of all the streamlines which go through this small region, the outermost through the corner

experiences the smallest strain. Fig. 4.17 shows the variation of flow pattern parameter ψ along this streamline. Generally, ψ increases along the stream line from the side wall to the center line. But there is one peak near the center line. Depending on the starting point for computing the strain, different values can be obtained at the corner of the small region. Fig. 4.18 shows the cumulative strain along the stream line with start points corresponding to different ψ values in Fig. 4.17. For all the case, the total strain is larger than 1. Thus, we assume steady stretching at the tip. In comparison the opposed nozzle device has a typical strain around 1.

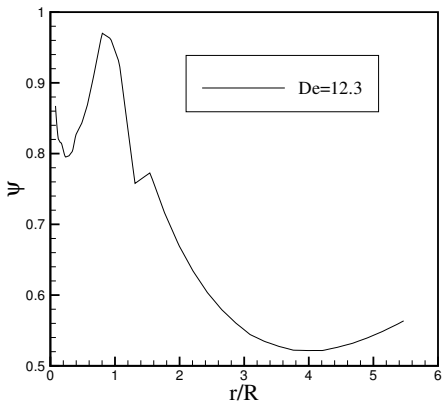

Figure 4.17: Flow pattern parameter ψ along the stream line. $Ca = 28.97$, $k = 0.7$,$\alpha = 0.1$ and $H/R = 8$.

4.6.2 Local strain rate

To calculate the extensional viscosity of a fluid from Eq. (4.30), we need to know the surface tension σ, the tip curvature κ, the depth of the dip $H - h$ and the local strain rate $\dot{\epsilon}$ near the tip of the interface. Of these, $\dot{\epsilon}$ is the most difficult to determine. In the experiment, there is no simple method to measure $\dot{\epsilon}$ directly. Here, we develop a correlation from the numerical results for $\dot{\epsilon}$ in terms of the material and control parameters of the system.

Consider the Giesekus fluid given by Eq. (2.6). Dimensional analysis shows the strain rate near the tip to be a function of the six dimensionless Π groups:

$$\xi = \frac{\dot{\epsilon} R^3}{Q} = f\left(Ca, Bo, \frac{H}{R}, k, De, \alpha\right). \tag{4.33}$$

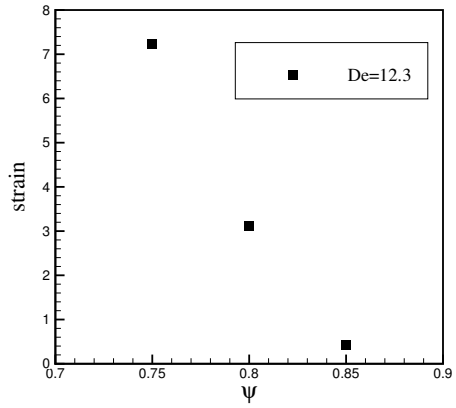

Figure 4.18: The strain along the stream line from different start point. $Ca = 28.97$, $k = 0.7$,$\alpha = 0.1$ and $H/R = 8$.

It would be very difficult to correlate ξ with all the parameters at once. Thus, we will first develop a correlation to Newtonian fluids, and then generalize that to the Giesekus fluid.

(a) Newtonian correlation

For a Newtonian system, Eq. (4.33) simplies to:

$$\xi = f\left(Ca, Bo, \frac{H}{R}\right). \tag{4.34}$$

Similarly, the position of the tip h/R can also be expressed in the same 3 Π groups. It turns out to be advantageous to rewrite Eq. (4.34) by using $\chi = (H - h)/R$ in place of H/R:

$$\xi = f\left(Ca, Bo, \chi\right). \tag{4.35}$$

As will be shown later, using χ facilitates generalization of the correlation to include viscoelastic effects.

Figure 4.19 plots ξ versus χ on a semi-log scale for a range of Ca and Bo values. All curves have the same gentle S shape, which we can represent linearly. The slope of the linear function is depend on the value of Ca and Bo. We use two steps to do the curve fitting. At first, a linear function $\log \xi = A + B\chi$ is used to fit the plot between $\log \xi$ and χ. As the result of this, for each pair of Ca and Bo, we will have a value of A and B. Then we do the curve fitting for A and B as functions of Ca and Bo. The dependence of A and B on

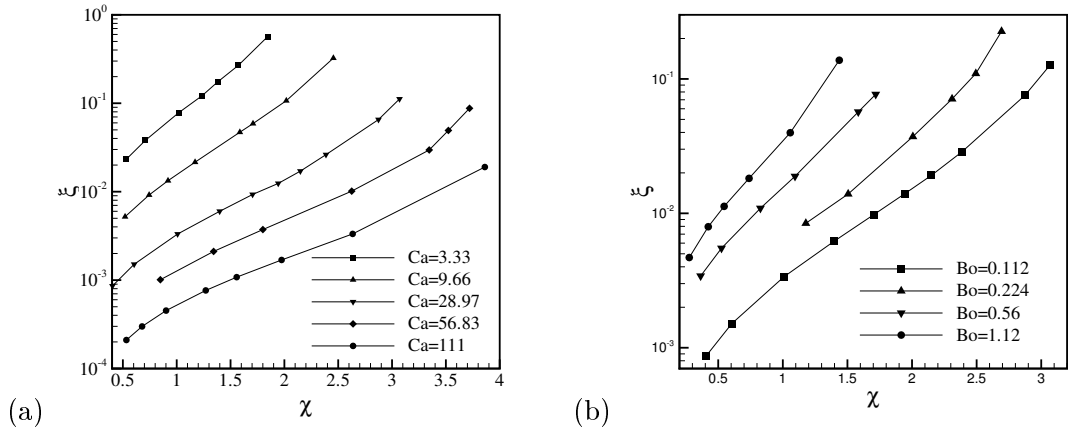

(a) (b)

Figure 4.19: The dimensionless strain rate ξ at the tip as a function of χ for a Newtonian fluid for (a) a fixed $Bo = 0.112$ and a range of Ca values; and (b) a fixed $Ca = 28.97$ and a range of Bo values.

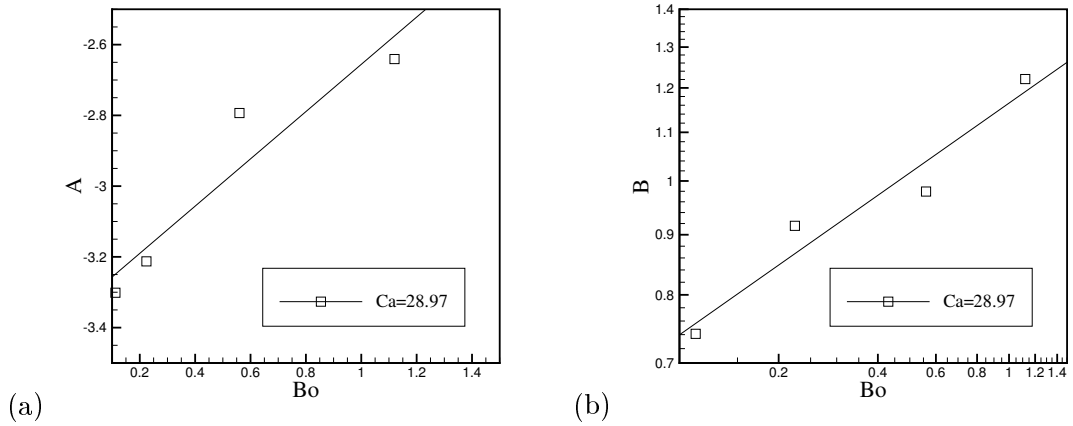

(a) (b)

Figure 4.20: The fitting parameters A and t as a function of Bo with $Ca = 28.97$.

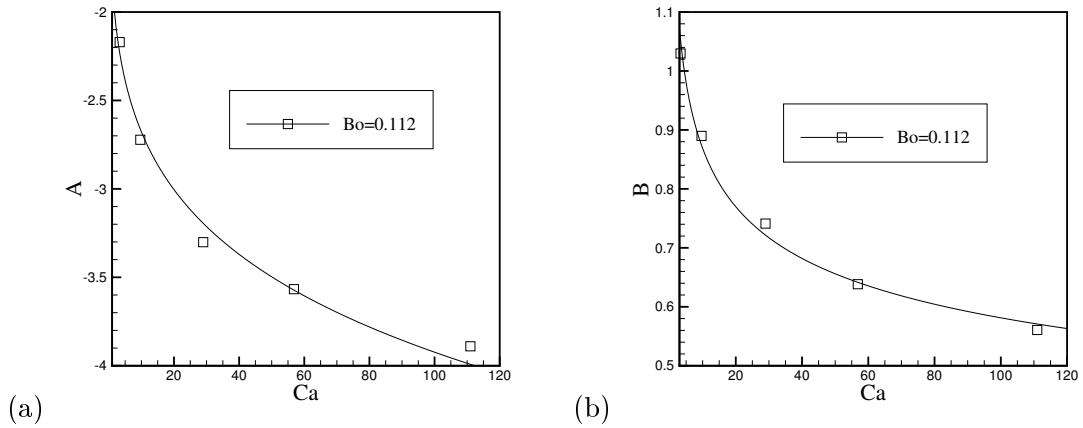

Figure 4.21: The fitting parameters A and t as a function of Ca with $Bo = 0.112$.

Ca and Bo is depicted in Fig. 4.20 and 4.21. Summarizing the plots, we come up with the following formulae:

$$\log \xi = A + B\chi, \tag{4.36}$$

$$B = (2.27 + 0.84 log Bo) Ca^{-0.2}, \tag{4.37}$$

$$A = (-2.01 + 0.41 Bo) Ca^{0.15}. \tag{4.38}$$

The accuracy of this correlation is examined in Fig. 4.22, where the y-axis is the ratio between the strain rate ξ_c given by the correlation Eq. (4.36) and the actual strain-rate ξ obtained in simulations at various Bo and Ca values. The same Bo and Ca values and the χ value of the simulation are used in computing ξ_c. Most of the data points fall between 0.7 and 1.3, giving a margin of error of 30%. This is quite accurate in view of the range of error of prior rheometers.

(b) Viscoelastic correlation

The last subsection has made it clear that viscoelasticity enhances interface deformation. Not surprisingly, it also affects the local strain rate at the tip. For example, Fig. 4.23 shows that for the same Bo, Ca and H/R, the dimensionless strain rate ξ at the tip increases with viscoelasticity. This is because the fluid near the tip is stretched by the flow, and yields greater force to pull it down toward the orifice.

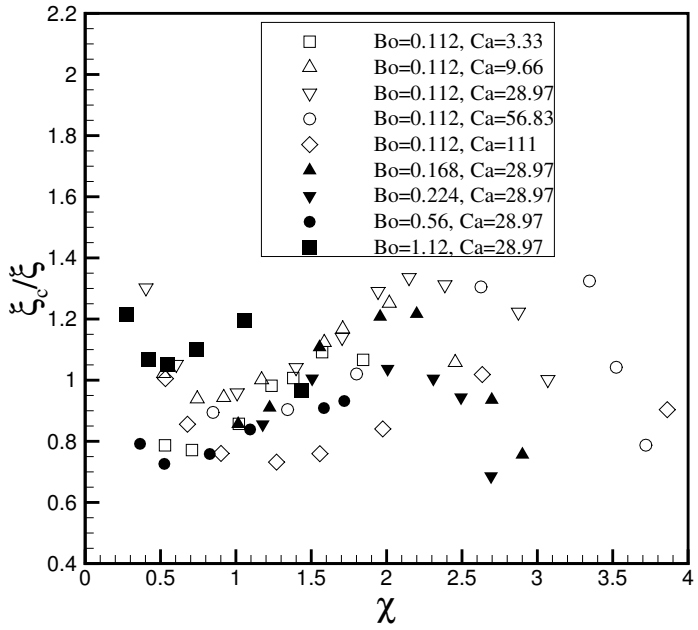

Figure 4.22: The error of the elongational rate estimation.

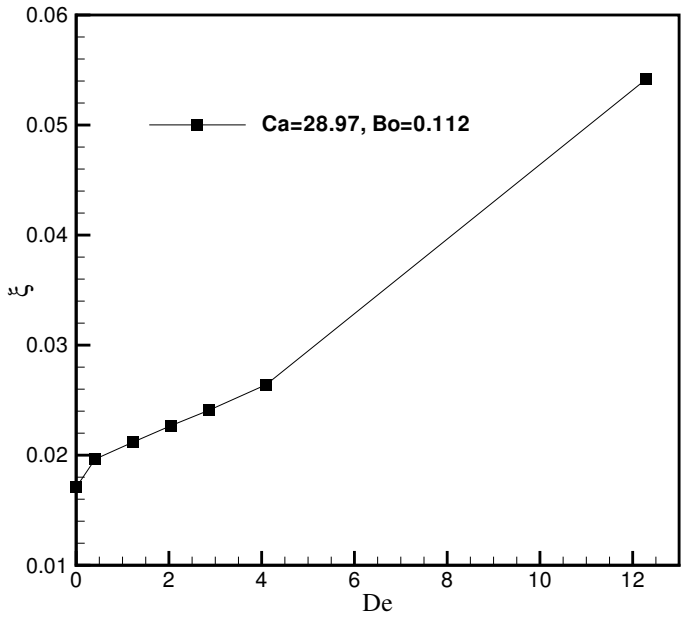

Figure 4.23: The effect of the polymer for the strain rate on the tip. $Ca = 28.97$ and $Bo = 0.112$ for all the cases. We use Giesekus model to represent the rheology in these cases. The H/R is fixed at 8 and relaxation time λ_H is changed in each case.

In coming up with the correlation of Eq. (4.33), we now have to deal with the rheological parameters. However, by a coincidence that we cannot yet explain, if we use $\chi = (H-h)/R$ in the correlation instead of H/R, *all the viscoelastic data collapse onto a single curve*, and the same Newtonian correlation, Eq. (4.36), accounts for the viscoelastic data as well! We have do far computed Giesekus and Oldroyd-B models, with the following range of rheological parameters: $0.41 < De < 12.3$ and $0.01 < \alpha < 0.1$. Fig. 4.24 depicts this collapsing; all the data fall on the same curve. As yet, we do not have a sound rationalization for this coincidence. It is clear that increasing the polymer stress in the fluid will increase the deformation of the free surface χ as well as the stain rate at the tip ξ. Meanwhile, increasing the viscous stress (or Ca) will have similar effects. Our result shows that the same relationship between χ and ξ holds, regardless of the agent—viscous or viscoelastic—that has prompted their change.

Figure 4.25 checks the error of the correlation Eq. (4.36) against numerical results for viscoelastic fluids. As in Fig. 4.22, The y-axis is the ratio ξ_c/ξ, with ξ being the actual local

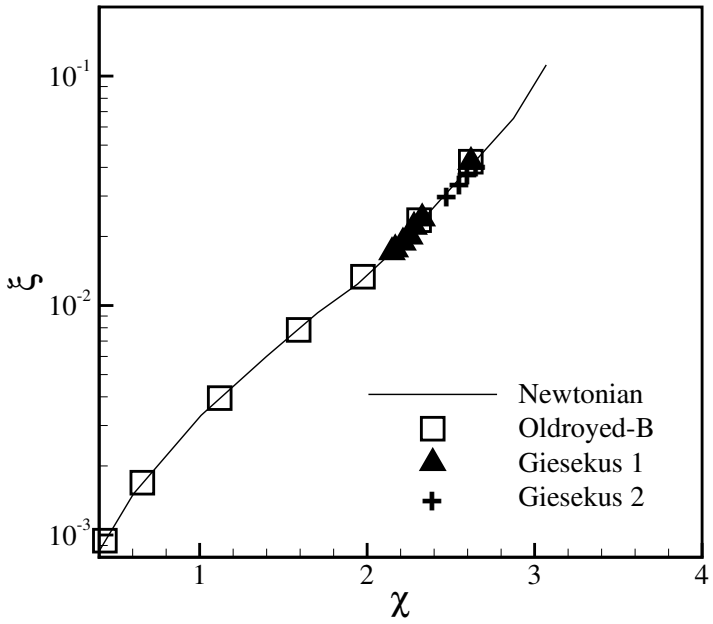

Figure 4.24: The local strain rate on the tip as the function of χ for Newtonian and viscoelastic fluids. $Ca = 28.97$ and $Bo = 0.112$ for all the cases. We have three series of data for viscoelastic fluids. For series Oldroyd-B, we use the Oldroyd-B model and fix $De = 2.05$. We change H for every case to change χ. For series Giesekus 1, we use the Giesekus model and fix $\alpha = 0.1$ and $k = 0.7$. We change De to realize different steady-state χ. For series Giesekus 2, we also use the Giesekus model but fix $De = 8.2$ and $k = 0.7$. We change α to realize different χ.

strain rate from simulations at different values between 0.1 and 10^{-3} and ξ_c is that given by the correlation at the same Ca, Bo and χ values. In all the cases, the value of ξ_c/ξ is between 1 and 1.4. Therefore, Eq. (4.36) applies equally well to Newtonian and viscoelastic fluids.

This has two astonishing implications: (a) The role of the polymer tensile stress in increasing the local $\dot{\epsilon}$ is fully accounted for by the degree at which the position of the tip is drawn toward the orifice. (b) For the extensional rheometer, the formulas of Eq. (4.30) and Eq. (4.36) can be used to obtain the elongational viscosity of Newtonian as well as viscoelastic liquids. The latter observation is quite convenient, but its accuracy remains to be confirmed by comparison with experimental data.

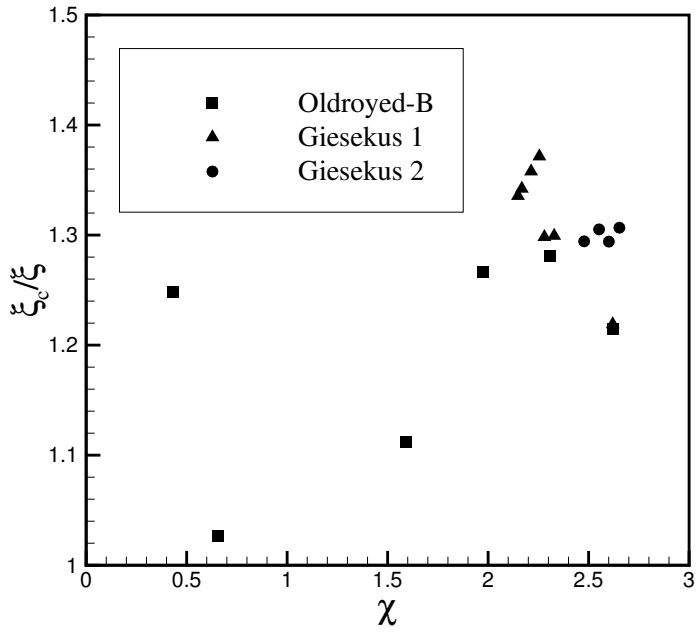

Figure 4.25: The error of the elongational rate estimation for viscoelastic fluids. In this plot, the series of Oldroyd-B, Giesekus 1 and Giesekus 2 are the same as Fig. 4.24.

4.6.3 Benchmarking by experimental data

To use a selective withdrawal device to measure the elongational viscosity of a liquid in the laboratory, one goes through the following steps. (i) Measure the density and surface tension of the fluid. (ii) Achieve a steady-state interface in the subcritical regime for a prescribed flow rate. (iii) Measure the interfacial position (in terms of h and H) and the tip curvature κ. (iv) Use Eq. (4.36) to estimate the local strain rate $\dot{\epsilon}$, and Eq. (4.30) to obtain the elongational viscosity $\bar{\eta}$.

To benchmark this scheme, one takes a liquid with known elongational viscosity, e.g. measured through other means, and perform the selective withdrawal experiment on it. In principle, the $\bar{\eta}$ estimated from the scheme can then be compared with the actual value. In reality, there are several subtleties to the benchmarking. First, there are no reliable methods to measure $\bar{\eta}$, especially for low-viscosity Boger liquids and at relatively low strain rates. Indeed, this was largely the motivation for exploring the selective withdrawal for this

purpose. Possible candidates are the filament stretching elongational rheometer (FiSER) and the capillary breakup elongational rheometer (CaBER). Second, it is unclear what strain the measured $\bar{\eta}$ corresponds to. FiSER and CaBER typically provides a transient, "elongational stress growth viscosity" $\bar{\eta}^+$ as a function of time or strain [18]. More often than not, no steady-state stretching is attained, and thus $\bar{\eta}^+$ never approaches an $\bar{\eta}$. In the selective withdrawal experiment, on the other hand, the fluid experiences a complex strain history that is not easily quantifiable. Even though the flow is steady in the Eulerian sense, the material points most probably cannot attain steady stretching in the rheological sense, and the total strain is not known. It is obviously not accurate to assume that the local elongational stress at the tip corresponds to the *steady-state* N_1 at the local $\dot{\epsilon}$. But there does not seem to be a more appropriate way of characterizing this situation. The same ambiguities exist for the opposed-nozzle device, for example.

Under these considerations, we have decided on a two-pronged approach for the benchmarking. On the one hand, we measure the rheological properties of the polymer solutions used in Chapter 3, and fit these into a Giesekus model. Then the *theoretical* elongational viscosity $\bar{\eta}$ is calculated, similar to that depicted in Fig. 7.3-8 of Bird *et al.* [18], and is used to benchmark the $\bar{\eta}$ measured from selective withdrawal. On the other hand, we take $\bar{\eta}^+$ data measured using FiSER[1] and compare them to our value.

(*a*) *Benchmarking against the Giesekus fluids*

Our experiment in Chapter 3 used two polymer solutions, a strongly elastic SE fluid and a weakly elastic WE fluid. The following uses only the SE fluid. Its relaxation time has been measured from CaBER to be $\lambda_H = 8.5$ s. The shear viscosity of the solution and the solvent were measured on a Bohlin rotational rheometer and the polymer and solvent viscosities, as appear in the Giesekus model, are $\mu_p = 16.75$ Pa·s, $\mu_s = 4.25$ Pa·s, with a viscosity ratio $k = 0.2$. The mobility factor α is obtained from fitting the shear-thinning at larger shear rates: $\alpha = 0.2$.

In the experiment, the surface tension σ and density ρ are measured, respectively, by a ring tensiometer (Cole-Parmer Surface Tensiomat Model 21) and a densitometer (Anton

[1] These measurements have been kindly performed by Professor David F. James for us at the University of Toronto.

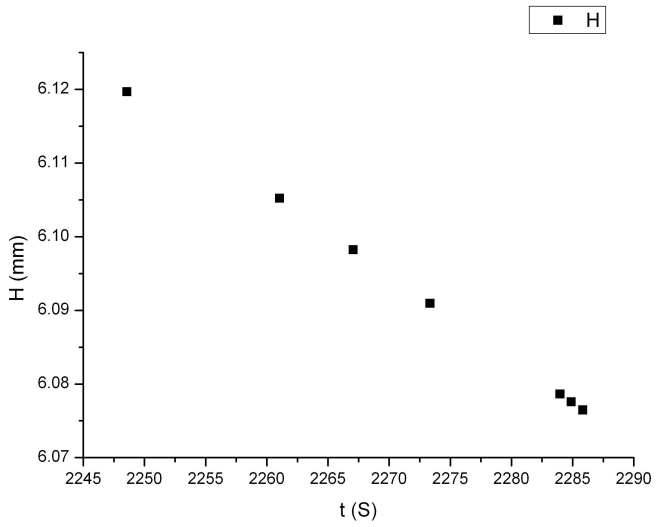

Figure 4.26: The liquid level H as the function of time during the deformation of surface.

Paar DMA 35N Portable Density Meter). From the video recording of surface deformation, we measure the value of κ, H and h. One minor complication is that while h is recorded continuously by video, H is only captured by snapshots on a still camera, and for the relatively rapid viscoelastic process, the temporal resolution is insufficient. Thus we use an indirect method to back out H from h. Figure 3.10 shows that for a long period after the start of the experiment ($t \leq 2250$ s), the curvature is zero and there is no deformation of the interface. Thus, $H(t) = h(t)$ in this period, and the constant speed of the lowering interface can be calculated from Fig. 3.10(b): $dH/dt = dh/dt = 0.00116$ mm/s. Assuming that this speed does not change later when the free surface is deforming, which is reasonable since the flow rate Q is fixed, we obtain the entire $H(t)$ history throughout the experiment (Fig. 4.26). Now $\chi = (H - h)/R$ can be calculated for any snapshot of the video. Using the scheme outlined above, $\bar{\eta}$ is obtained as a function of $\dot{\epsilon}$.

Figure 4.27 compares the "measured" $\bar{\eta}$ with that of the Giesekus fluid. Note first that the data for three Ca values more or less coincide. Thus, the measurement is intrinsic to the fluid rather than affected by the flow situations. This lends confidence to the validity of the scheme. Second, the measured $\bar{\eta}$ values are within a reasonable range of the theoretical values. The data fall below the Giesekus curve for $\dot{\epsilon} < 0.1$ s^{-1}, and overshoot it for higher

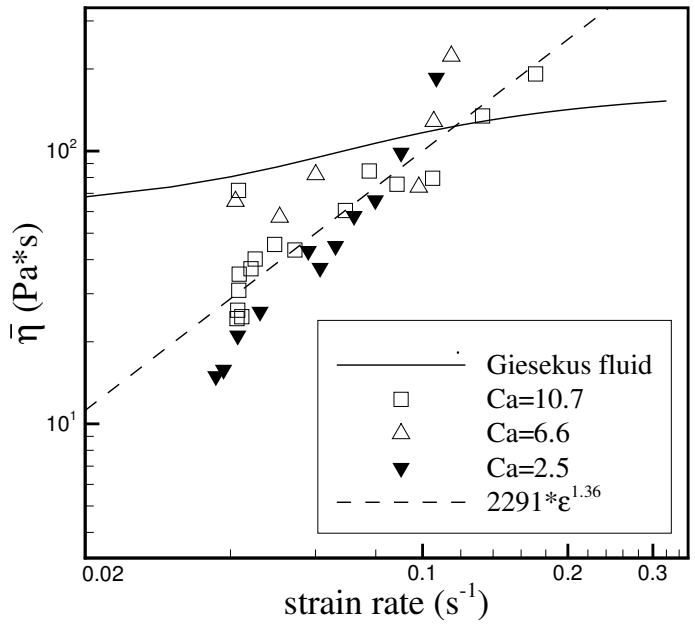

Figure 4.27: Comparison of the elongational viscosity between that measured by selective withdrawal and the theoretical value of the Giesekus model. H varies in each data set of fixed Ca, and differs among the 3 data sets.

strain rates. Over the entire range, the difference is within a factor of 3. If the Giesekus benchmark is taken to be the true elongational viscosity of the fluid, this margin of error is quite acceptable in view of the poor accuracy of existing methods [8]. The relatively close agreement between the experimental data and the theoretical curve also implies that in subcritical selective withdrawal, the polymer solution near the tip experiences nearly steady-state stretching. This is conceivable in view of the low velocity and elongational flow type in that region. Finally, the measured $\bar{\eta}$ increases with $\dot{\epsilon}$ as does the theoretical curve, albeit at a greater slope. A power-law $\bar{\eta} = 2291\dot{\epsilon}^{1.36}$ gives a reasonable fitting to the experimental data.

(*b*) *Benchmarking against filament stretching data*

Fig 4.28 shows the FiSER measurements of the SE and WE fluids used in our experiments. First, note that the FiSER returns the transient *elongational stress growth viscosity*, and apparently no steady stretching is approached in these tests. This is similar to the CaBER.

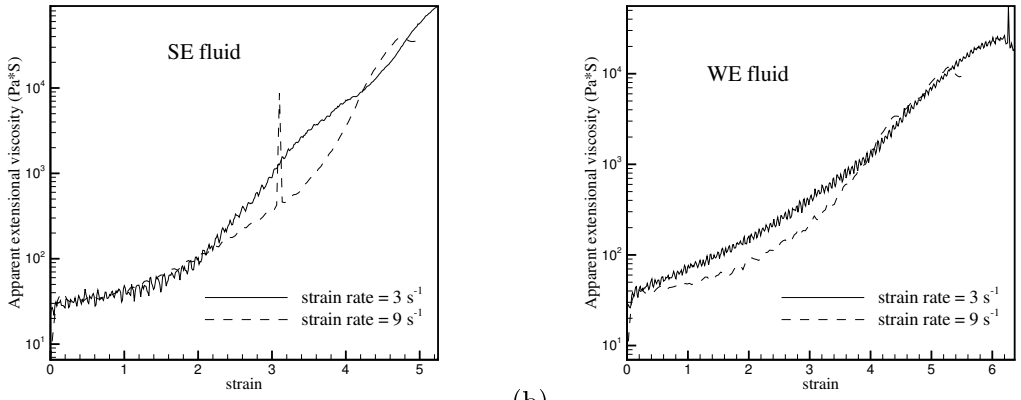

(a) (b)

Figure 4.28: The transient elongational stress growth viscosity of our experimental fluids SE (a) and WE (b) measured by a filament stretching device. Each plot has two curves corresponding to extension rates of 3 s^{-1} and 9 s^{-1}.

In fact, these results agree fairly closely with the CaBER data reported in the last chapter, with the SE fluid showing a larger $\bar{\eta}^+$ than the WE fluid. Second, the selective withdrawal flow setup can access strain rates much below those in filament stretching and even opposed-nozzle devices. This may be a potential advantage for our strategy in that it fills certain niche applications. Third, the FiSER data show little consistent dependence on the strain rate between the two values tested, while the selective withdrawal data of Figs. 4.27 show a power-law increase in a much lower $\dot{\epsilon}$ range. If we extrapolate the latter to $\dot{\epsilon} = 9$ s^{-1}, we have $\bar{\eta} = 4.55 \times 10^4$ Pa·s, quite close to the maximum transient elongational viscosity attained for the SE fluid in Fig. 4.28(a). This may be viewed as an indirect confirmation of the extensional viscosity measured by the selective withdrawal scheme.

4.7 Conclusion

The numerical computations of this chapter demonstrate the capability of the arbitrary Lagrangian-Eulerian (ALE) methodology in simulating free surface deformation of viscoelastic liquids. There are two main results from this effort:

(a) We have elucidated the effects of viscoelasticity on interfacial deformation during selective withdrawal, including the hump height and tip curvature in the subcritical regime and the critical condition for jet formation.

(b) We have explored the possibility of using selective withdrawal to measure the steady-state elongational viscosity of polymer solutions.

Regarding (a), the numerical computations show the correct trend in terms of increased deformation due to elastic stresses, and identified strain-hardening as the key mechanism at work. The limitations to this part of the results are the failure to reach Deborah number ranges of the experiment and to predict the interfacial rupture. The former is a common problem for viscoelastic computations, and newer schemes such as the logarithmic formalism offer hope of approaching higher Deborah numbers while maintaining the positive-definiteness of the polymer configuration tensor [136]. The latter problem is intrinsic to the sharp-interface formulation of the ALE method, and can only be remedied by alternative formulation of the interface, e.g., via diffuse-interface models [46, 66].

Regarding (b), we have examined the factors key to the success of this strategy, including the local flow type and the normal stress and strain rate at the tip, and compared the accuracy of the measurement with existing methods of extensional rheometry. Based on these, we have reached the preliminary conclusion that selective withdrawal can potentially be used as an extensional rheometer. Its maximum error of 47% for Newtonian fluids is superior to opposed-nozzle devices [8]. For polymer solutions, no definitive benchmark exists. But an estimated maximum error of about 300% compares favorably with opposed-nozzle and contraction flow devices [132, 137].

As an extensional rheometer, the selective withdrawal device has several unique advantages. Because the elongational stress and strain rate are sampled within a very small region surrounding the stagnation point, the procedure measures a *steady-stretching* elongational viscosity. None of the existing devices produces steady stretching as easily. Moreover, thanks to its transducer-free scheme for determining the elongational stress, selective withdrawal can test low-viscosity liquids, and access much lower strain rates than other devices. Finally, the device is relatively immune to complicating factors such as inertia, spatial inhomogeneity and filament sagging common to other devices [8, 127].

We must note that our work on (b) suffers from two limitations. First, we have no direct measurement of the local strain rate at the tip. Consequently, we have to resort to numerical data and exploit an apparent coincidence that allows us to represent the local strain rate

using a general correlation for both Newtonian and viscoelastic fluids. This should be remedied in the future by direct PIV measurements of the local flow field [138]. Second, there are no definitive benchmarks for polymer solutions to firmly establish the accuracy of the selective withdrawal protocol. Indeed, this is owing to the lack of a device capable of similar measurements, and speaks indirectly to the value of such a rheometer. Further investigation should aim to remove these uncertainties and optimize the design of the device.

Chapter 5

Conclusions and recommendations

The overarching theme of this dissertation is to examine how bulk non-Newtonian stresses affect interfacial motion and deformation. This is accomplished, in three somewhat related projects, using numerical computations and experimental observations. Based on this study, one may draw the following general and fundamental conclusions.

(a) Extensional flows near the interface effectively activates the viscoelastic stress in the bulk, which then exerts significant influences on the interface.

(b) Such influences may be manifested by relatively mild deformation of the interface, which enlists interfacial tension to balance the viscoelastic stress. Or they may cause more drastic changes of interfacial morphology, causing instability or even rupture.

(c) This fundamental balance between interfacial tension and polymer stress may be exploited in a well-controlled geometry to measure the polymer stress, and thus the polymer elongational viscosity. This would be of great practical value since there is a dearth of viable methods for such measurements.

(d) In terms of numerical simulation of interfacial flows, the choice of model and algorithm must be dictated by the need for interfacial resolution. Whereas a diffuse-interface model might suffice for relatively mild flow situations, more severe deformation of the interface may call for a sharp-interface formulation. In either case, simulating singular events of the interface, such as rupture or coalescence, remains a challenge.

5.1 Summary of research findings

The thesis consists of three related but independent projects: drop deformation in converging pipe flow, experiment on selective withdrawal, and numerical simulation of selective withdrawal. Within each, we strive to elucidate the mechanisms by which non-Newtonian bulk rheology affects interfacial dynamics. The main results are summarized below.

(i) In the first project, I investigated the influence of viscoelasticity on drop deformation in converging pipe flows in a conical geometry. Three series of simulations have been carried out, with Newtonian drops in a Newtonian matrix, Giesekus drops in a Newtonian matrix and Newtonian drops in a Giesekus matrix. Viscoelastic effect may enhance or suppress drop deformation depending on the flow and material parameters. The key factor is whether the polymer chains have had sufficient time to stretch and develop a sizeable polymer stress, based on which two regimes can be defined. In the weak regime, a polymer drop deforms more readily than a comparable Newtonian one, and a polymer matrix is less able to deform a drop than a Newtonian matrix of the same viscosity. In the strong regime, the trend is reversed. Which behavior prevails in a conical flow channel depends on the capillary number and the viscosity ratio. This understanding reconciles contradictory results in the literature.

(ii) The second project is an experimental study of air-liquid selective withdrawal. Newtonian liquids only exhibit the subcritical behavior, with a deformed but continuous interface. This behavior and the quantitative surface shape are in good agreement with previous experiments. For viscoelastic polymer solutions, on the other hand, we discover a threshold beyond with the interface becomes a cusp, emits an air jet and becomes supercritical. The critical condition depends on the flow rate, rheology of the fluid and the location of the interface. The contrast between Newtonian and polymeric liquids is explained in terms of the elongational stress pulling the surface down.

(iii) The third project, finite-element simulation of selective withdrawal, complements the second. Subject to numerical limitations to be detailed below, we have reproduced the key effects in the experiments, and confirmed that it is the elongational polymer stress, or strain hardening, that is at the root of the viscoelastic effects. More specifically, the simulations show that the surface of the viscoelastic liquid deforms more than the Newtonian one, and that the critical condition, in terms of rheological and operating parameters, is captured with reasonable accuracy. As an outgrowth of this study, we suggest that the steady-state interface be used as an extensional rheometer for measuring the elongational viscosity of dilute polymer solutions. Based on the limited data we have, the scheme seems to be viable, yielding better accuracy than has been achieved by pre-existing methods.

5.2 Limitations of current work

Both the numerical algorithms and experimental techniques suffer from certain shortcomings. This to some extent limits the scope and depth of the study. These are summarized as follows.

(i) The sharp-interface method and ALE moving grid algorithm cannot accommodate the critical condition in selective withdrawal. This is because the surface is represented by grid points, and thus the code can only track surface curvature to a certain finite value. Beyond that, the interfacial forces are not evaluated accurately, the surface loses smoothness, and the numerical computation breaks down. This is a well-known limitation for interface-tracking schemes, and in the case of drop breakup is often bypassed by artificially removing and reconnecting interfaces. In our problem such schemes would not work as the thin air jet is a stable feature that has to be accounted for. This precludes a simulation of the critical conditions, the supercritical regime, as well as the hysteresis observed experimentally.

(ii) The well-known "high Weissenberg number problem" prevented me from attaining the same Deborah number in the simulations as in the experiments. Thus, the numerical data range overlaps but does not fully cover that of the experimental data. This presents some inconvenience in comparing the two in terms of the critical condition for jet formation.

(iii) Experimentally, the surface is well resolved except for the very thin air jet in the supercritical regime with viscoelastic liquids. Poor image quality led to noisy data for the thin air jet in the supercritical regime. As such, I was unable to examine the relationship between the air jet diameter and the control parameters of the experiment with confidence.

(iv) The examination of the proposed new strategy for measuring the elongational viscosity is hampered by the lack of a suitable benchmark. This is mainly due to the lack of an accurate device for such measurements, which was the motivation for our proposing a new device to begin with.

5.3 Recommendations for future work

In light of the above, it seems that the fundamental physics of the process, in terms of how the polymer stress affects interfacial deformation, is quite clear, at least qualitatively. What most urgently needs further investigation is the proposed strategy of measuring elongational viscosity by surface deformation. Compared with prior devices, the advantages are obvious: the setup is simple and the measurement is easy, and this process can measure low-viscosity fluids down to strain rates at least an order of magnitude smaller than previous equipments such as opposed nozzles and filament stretching. Further work should center on two areas:

(i) To establish a more accurate formula for estimating the local strain rate. The current data was obtained from a limited range of numerical computations, and no direct comparison with experiments could be carried out. Therefore, one needs to obtain detailed measurements of the flow field, using laser Doppler velocimetry for example, on which the required formula can be sounded based.

(ii) The develop more suitable and accurate benchmarks for the final measurements. In the present study, I had to use numerical results for a Giesekus fluid and limited data from a filament stretching device. The way forward seems to use highly viscous solutions that are more suitable for traditional elongational rheometers. For such fluids, steady-stretching can be achieved, and the elongational viscosity can be used to benchmark the proposed device.

Bibliography

[1] S. T. J. Peng and R. F. Landel, "Preliminary investigation of elongational flow of dilute polymer-solutions," J. Appl. Phys. **47**, 4255 (1976).

[2] E. Soto, C. Goujon, R. Zenit, and O. Manero, "A study of velocity discontinuity for single air bubbles rising in an associative polymer," Phys. Fluids **18**, 121510 (2006).

[3] B. Akers and A. Belmonte, "Impact dynamics of a solid sphere falling into a viscoelastic micellar fluid," J. Non-Newtonian Fluid Mech. **135**, 97 (2006).

[4] C. van der Reijden-Stolk and A. Sara, "A study on polymer blending microrheology. Part 3. Deformation of Newtonian drops submerged in another Newtonian fluid flowing through a converging cone," Polym. Eng. Sci. **26**, 1229 (1986).

[5] I. Cohen, "Scaling and transition structure dependence on the fluid viscosity ratio in the selective withdrawal transition," Phys. Rev. E **70**, 026302 (2004).

[6] S. Courrech du Pont and J. Eggers, "Sink flow deforms the interface between a viscous liquid and air into a tip singularity," Phys. Rev. Lett. **96**, 034501 (2006).

[7] S. L. Anna, G. H. McKinley, D. A. Nguyen, T. Sridhar, S. J. Muller, J. Huang, and D. F. James, "An interlaboratory comparison of measurements from filament-stretching rheometers using common test fluids," J. Rheol. **45**, 83 (2001).

[8] P. Dontula, M. Pasquali, L. E. Scriven, and C. W. Macosko, "Can extensional viscosity be measured with opposed-nozzle devices?" Rheol. Acta **36**, 429 (1997).

[9] D. Klempner and K. C. Frisch, editors, *Handbook of Polymeric Foams and Foam Technology* (Hanser Publishers, New York, 1991).

[10] L. A. Utracki, *Polymer Alloys and Blends* (Hanser, Munich, 1990).

[11] S. Gao, K. Moran, Z. Xu, and J. Masliyah, "Role of bitumen components in stabilizing water-in-diluted oil emulsions," Energ. Fuel. **23**, 2606 (2009).

[12] A. Lefebvre, editor, *Atomization and Sprays* (Hemisphere Publishing Corporation, 1989).

[13] A. A. Darhuber and S. M. Troian, "Principles of microfluidic actuation by modulation of surface stresses," Ann. Rev. Fluid Mech. **37**, 425 (2005).

[14] J. Kobayashi, Y. Mori, K. Okamoto, R. Akiyama, M. Ueno, T. Kitamori, and S. Kobayashi, "A microfluidic device for conducting gas-liquid-solid hydrogenation reactions," Science **304**, 1305 (2004).

[15] T. M. Squires and S. R. Quake, "Microfluidics: Fluid physics at the nanoliter scale," Rev. Mod. Phys. **77**, 977 (2005).

[16] K. Sato, A. Hibara, M. Tokeshi, H. Hisamoto, and T. Kitamori, "Microchip-based chemical and biochemical analysis systems," Adv. Drug Deliv. Rev. **55**, 379 (2003).

[17] R. G. Larson, editor, *The structure and Rheology of Complex Fluids* (Oxford University Press, Inc, New York, 1999).

[18] R. B. Bird, R. C. Armstrong, and O. Hassager, *Dynamics of Polymeric Liquids, Vol. 1. Fluid Mechanics* (Wiley, New York, 1987).

[19] A. B. Metzner, "Behavior of suspended matter in rapidly accelerating viscoelastic fluidsuebler effect," AICHE Journal **13**, 316 (1967).

[20] P. Poulin, H. Stark, T. C. Lubensky, and D. A. Weitz, "Novel colloidal interactions in anisotropic fluids," Science **275**, 1770 (1997).

[21] T. Podgorski and A. Belmonte, "Surface folding of viscoelastic fluids: Finite elasticity membrane model," Eur. J. Appl. Math. **15**, 385 (2004).

[22] A. Belmonte, "Self-oscillations of a cusped bubble rising through a micellar solution," Rheol. Acta **39**, 554 (2000).

[23] M. C. Sostarecz and A. Belmonte, "Beads-on-string phenomena in wormlike micellar fluids," Phys. Fluids **16**, L67 (2004).

[24] M. S. N. Oliveira and G. H. McKinley, "Iterated stretching and multiple beads-on-a-string phenomena in dilute solutions of highly extensible flexible polymers," Phys. Fluids **17**, 071704 (2005).

[25] A. M. Grillet, A. G. Lee, and E. S. G. Shaqfeh, "Observations of ribbing instabilities in elastic fluid flows with gravity stabilization," J. Fluid Mech. **399**, 49 (1999).

[26] M. A. Spaid and G. M. Homsy, "Stability of viscoelastic dynamic contact lines: An experimental study," Phys. Fluids **9**, 823 (1997).

[27] L. M. Pismen, "Perturbation theory for traveling droplet," Phys. Rev. E **74**, 041605 (2006).

[28] N. J. Balmforth, R. V. Craster, and C. Toniolo, "Interfacial instability in non-newtonian fluid layers," Phys. Fluids **15**, 3370 (2003).

[29] M. A. Spaid and G. M. Homsy, "Stability of newtonian and viscoelastic dynamic contact lines," Phys. Fluids **8**, 460 (1996).

[30] S. Hartland, editor, *Surface and Interfacial Tension* (Marcel Dekker, INC., 2004).

[31] J. A. Sethian and P. Smereka, "Level set methods for fluid interfaces," Ann. Rev. Fluid Mech. **35**, 341 (2003).

[32] D. M. Anderson, G. B. McFadden, and A. A. Wheeler, "Diffuse-interface methods in fluid mechanics," Ann. Rev. Fluid Mech. **30**, 139 (1998).

[33] J. D. van der Waals, "The thermodynamic theory of capillarity under the hypothesis of a continuous variation of density," Verhandel Konink. Akad. Weten. Amsterdam, (Sect. 1) **1**, 1 (1892), translation by J. S. Rowlingson, *J. Statist. Phys.* 20 (1979), 197–244.

[34] P. Yue, J. J. Feng, C. Liu, and J. Shen, "A diffuse-interface method for simulating two-phase flows of complex fluids," J. Fluid Mech. **515**, 293 (2004).

[35] J. J. Feng, C. Liu, J. Shen, and P. Yue, "An energetic variational formulation with phase field methods for interfacial dynamics of complex fluids: advantages and challenges," in M.-C. T. Calderer and E. M. Terentjev, editors, "Modeling of Soft Matter," pp. 1–26 (Springer, New York, 2005).

[36] C. L. Tucker and P. Moldenaers, "Microstructural evolution in polymer blends," Ann. Rev. Fluid Mech. **34**, 177 (2002).

[37] C. Zhou, P. Yue, and J. J. Feng, "Simulation of neutrophil deformation and transport in capillaries using simple and compound drop models," Ann. Biomed. Eng. **35**, 766 (2007).

[38] J. M. Rallison, "The deformation of small viscous drops and bubbles in shear flows," Ann. Rev. Fluid Mech. **16**, 45 (1984).

[39] H. A. Stone, "Dynamics of drop deformation and breakup in viscous fluids," Ann. Rev. Fluid Mech. **26**, 65 (1994).

[40] S. Ramaswamy and L. G. Leal, "The deformation of a Newtonian drop in the uniaxial extensional flow of a viscoelastic liquid," J. Non-Newtonian Fluid Mech. **88**, 149 (1999).

[41] S. Ramaswamy and L. G. Leal, "The deformation of a viscoelastic drop subjected to steady uniaxial extensional flow of a Newtonian fluid," J. Non-Newtonian Fluid Mech. **85**, 127 (1999).

[42] R. W. Hooper, V. F. de Almeida, C. W. Macosko, and J. J. Derby, "Transient polymeric drop extension and retraction in uniaxial extensional flows," J. Non-Newtonian Fluid Mech. **98**, 141 (2001).

[43] F. Greco, "Drop deformation for non-Newtonian fluids in slow flows," J. Non-Newtonian Fluid Mech. **107**, 111 (2002).

[44] P. Yue, J. J. Feng, C. Liu, and J. Shen, "Transient drop deformation upon startup of shear in viscoelastic fluids," Phys. Fluids **17**, 123101 (2005).

[45] P. Yue, J. J. Feng, C. Liu, and J. Shen, "Viscoelastic effects on drop deformation in steady shear," J. Fluid Mech. **540**, 427 (2005).

[46] P. Yue, C. Zhou, J. J. Feng, C. F. Ollivier-Gooch, and H. H. Hu, "Phase-field simulations of interfacial dynamics in viscoelastic fluids using finite elements with adaptive meshing," J. Comput. Phys. **219**, 47 (2006).

[47] V. Sibillo, M. Simeone, S. Guido, F. Greco, and P. L. Maffettone, "Start-up and retraction dynamics of a Newtonian drop in a viscoelastic matrix under simple shear flow," J. Non-Newtonian Fluid Mech. **134**, 27 (2006).

[48] D. Khismatullin, Y. Renardy, and M. Renardy, "Development and implementation of VOF-PROST for 3D viscoelastic liquid-liquid simulations," J. Non-Newtonian Fluid Mech. **140**, 120 (2006).

[49] P. G. Ghodgaonkar and U. Sundararaj, "Prediction of dispersed phase drop diameter in polymer blends: The effect of elasticity," Polym. Eng. Sci. **36**, 1656 (1996).

[50] H. B. Chin and C. D. Han, "Studies on droplet deformation and breakup. I. Droplet deformation in extensional flow," J. Rheol. **23**, 557 (1979).

[51] D. Bourry, R. E. Khayat, L. A. Utracki, F. Goudbille, J. Picot, and A. Luciani, "Extensional flow of polymeric dispersions," Polym. Eng. Sci. **39**, 1072 (1999).

[52] S. J. Kim and C. D. Han, "Finite element analysis of axisymmetric creeping motion of a deformable non-Newtonian drop in the entrance region of a cylindrical tube," J. Rheol. **45**, 1279 (2001).

[53] F. Mighri, A. Ajji, and P. J. Carreau, "Influence of elastic properties on drop deformation in elongatinal flow," J. Rheol. **41**, 1183 (1997).

[54] R. E. Khayat, "Boundary element analysis of planar drop deformation in confined flow. Part II. Viscoelastic fluids," Eng. Anal. Boundary Elements **22**, 291 (1998).

[55] F. N. Cogswell, "Measuring the extensional rheology of polymer melts," J. Rheol. **16**, 383 (1972).

[56] R. B. Bird, C. F. Curtiss, R. C. Armstrong, and O. Hassager, *Dynamics of Polymeric Liquids, Vol. 2. Kinetic Theory* (Wiley, New York, 1987).

[57] M. Doi and S. F. Edwards, *The Theory of Polymer Dynamics* (Oxford, New York, 1986).

[58] C. W. Macosko, *Rheology: Principles, Measurements, and Applications* (VCH Publishers, Inc., 1994).

[59] P. Yue, J. J. Feng, C. Liu, and J. Shen, "Diffuse-interface simulations of drop coalescence and retraction in viscoelastic fluids," J. Non-Newtonian Fluid Mech. **129**, 163 (2005).

[60] J. Lowengrub and L. Truskinovsky, "Quasi-incompressible Cahn-Hilliard fluids and topological transitions," Proc. Roy. Soc. Lond. A **454**, 2617 (1998).

[61] D. Jacqmin, "Calculation of two-phase Navier-Stokes flows using phase-field modelling," J. Comput. Phys. **155**, 96 (1999).

[62] C. Liu and J. Shen, "A phase field model for the mixture of two incompressible fluids and its approximation by a Fourier-spectral method," Physica D **179**, 211 (2003).

[63] P. Yue, C. Zhou, and J. J. Feng, "Spontaneous shrinkage of drops and mass conservation in phase-field simulations," J. Comput. Phys. **223**, 1 (2007).

[64] S. A. Khan and R. G. Larson, "Comparison of simple constitutive equations for polymer melts in shear and biaxial and uniaxial extensions," J. Rheol. **31**, 207 (1987).

[65] V. Tirtaatmadja and T. Sridhar, "Comparison of constitutive equations for polymer solutions in uniaxial extension," J. Rheol. **39**, 1133 (1995).

[66] P. Yue, C. Zhou, and J. J. Feng, "A computational study of the coalescence between a drop and an interface in Newtonian and viscoelastic fluids," Phys. Fluids **18**, 102102 (2006).

[67] H. H. Hu, N. A. Patankar, and M. Y. Zhu, "Direct numerical simulations of fluid-solid systems using the arbitrary Lagrangian-Eulerian technique," J. Comput. Phys. **169**, 427 (2001).

[68] H. Gan, J. J. Feng, and H. H. Hu, "Simulation of the sedimentation of melting solid particles," Int. J. Multiphase Flow **29**, 751 (2003).

[69] L. A. Freitag and C. F. Ollivier-Gooch, "Tetrahedral mesh improvement using swapping and smoothing," Int. J. Numer. Methods Eng. **40**, 3979 (1997).

[70] S. C. Eisenstat and H. F. Walker, "Choosing the forcing terms in an inexact Newton method," SIAM J. Sci. Comput. **17**, 16 (1996).

[71] H. A. Stone, B. J. Bentley, and L. G. Leal, "An experimental-study of transient effects in the breakup of viscous drop," J. Fluid Mech. **173**, 131 (1986).

[72] D. C. Tretheway and L. G. Leal, "Deformation and relaxation of Newtonian drops in planar extensional flows of a Boger fluid," J. Non-Newtonian Fluid Mech. **99**, 81 (2001).

[73] I. Delaby, B. Ernst, Y. Germain, and R. Muller, "Droplet deformation in polymer blends during uniaxial elongational flow: Influence of viscosity ratio for large capillary numbers," J. Rheol. **38**, 1705 (1994).

[74] V. Sibillo, M. Simeone, and S. Guido, "Break-up of a Newtonian drop in a viscoelastic matrix under simple shear flow," Rheol. Acta **43**, 449 (2004).

[75] I. Delaby, R. Muller, and B. Ernst, "Drop deformation during elongational flow in blends of viscoelastic fluids. Small deformation theory and comparison with experimental results," Rheol. Acta **34**, 525 (1995).

[76] R. Hooper, M. Toose, C. W. Macosko, and J. J. Derby, "A comparison of boundary element and finite element methods for modeling axisymmetric polymeric drop deformation," Int. J. Numer. Meth. Fluids **37**, 837 (2001).

[77] J. J. Elmendorp and R. J. Maalcke, "A study on polymer blending microrheology: Part I," Polym. Eng. Sci. **25**, 1041 (1985).

[78] F. Mighri, P. J. Carreau, and A. Ajji, "Influence of elastic properties on drop deformation and breakup in shear flow," J. Rheol. **42**, 1477 (1998).

[79] S. Guido, M. Simeone, and F. Greco, "Deformation of a Newtonian drop in a viscoelastic matrix under steady shear flow. experimental validation of slow flow theory," J. Non-Newtonian Fluid Mech. **114**, 65 (2003).

[80] W. L. Olbricht and L. G. Leal, "The creeping motion of immiscible drops through a converging/diverging tube," J. Fluid Mech. **134**, 329 (1983).

[81] J. Imberger, "Selective withdrawal: a review," in "IAHR Proc. Second Int. Symp. on Stratified Flows," vol. 1, 381–400 (Norwegian Institute of Technology, 1980).

[82] J. M. Raphael, "Prediction of temperture in rivers and reservoirs," J. Power Div. **88**, 157 (1962).

[83] W. D. Wunderlich and R. A. Elder, "Selective withdrawal from density stratified reservoirs," Water resources Research Advance Report No. 21 (1969).

[84] R. C. Y. Koh, "Viscous stratified flow towards a sink," J. Fluid Mech. **24**, 555 (1966).

[85] V. V. Anohin, J. Imberger, J. R. Romero, and G. N. Ivey, "Effect of long internal waves on the quality of water withdrawal from a stratified reservoir," J. Hydraul. Eng. **132**, 1134 (2006).

[86] D. E. Farrow and G. C. Hocking, "A numerical model for withdrawal from a two-layer fluid," J. Fluid Mech. **549**, 141 (2006).

[87] L. K. Forbes and G. C. Hocking, "Withdrawal from a tow-layer inviscid fluid in a duct," J. Fluid Mech. **361**, 275 (1998).

[88] L. K. Forbes and G. C. Hocking, "Unsteady draining flows from a rectangular tank," Phys. Fluids **19**, 082104 (2007).

[89] L. K. Forbes, G. C. Hocking, and S. Wotherspoon, "Salt-water up-coning during extraction of fresh water from a tropical island," J. Eng. Math. **48**, 69 (2004).

[90] G. C. Hocking and L. K. Forbes, "Withdrawal from a fluid of finite depth through a line sink," J. Eng. Math. **38**, 91 (2000).

[91] G. C. Hocking and L. K. Forbes, "Super-critical withdrawal from a two-layer fluid thourgh a line sink if the lower layer is of finite depth," J. Fluid Mech. **428**, 333 (2001).

[92] I. R. Wood, "Extensions to the theory of selective withdrawal," J. Fluid Mech. **448**, 315 (2001).

[93] F. J. Spera, "Some numerical experiments on the withdrawal of magma withdarwal from stratified magma chambers," Geology **14**, 723 (1984).

[94] J. R. Blake and G. N. Ivey, "Magma-mixing and the dynamics of withdrawal from stratified reservoirs," J. Volcanol. Geoth. **27**, 153 (1986).

[95] J. R. Lister, "Selective withdrawal from a viscous two-layer system," J. Fluid Mech. **198**, 231 (1989).

[96] I. Cohen and S. R. Nagel, "Scaling at the selective withdrawal transition through a tube suspended above the fluid surface," Phys. Rev. Lett. **88**, 074501 (2002).

[97] M. K. Berkenbusch, I. Cohen, and W. W. Zhang, "Liquid interfaces in viscous straining flows: numerical studies of the selective withdrawal transition," J. Fluid Mech. **613**, 171 (2008).

[98] S. C. Case and S. R. Nagel, "Spout states in the selective withdrawal of immiscible fluids through a nozzle suspended above a two-fluid interface," Phys. Rev. Lett. **98**, 114501 (2007).

[99] J. Eggers and S. Courrech du Pont, "Numerical analysis of tips in viscous flow," Phys. Rev. E **79**, 066311 (2009).

[100] A. M. Gañán-Calvo, "Generation of steady liquid microthreads and micron-sized monodisperse sprays in gas streams," Phys. Rev. Lett. **80**, 285 (1998).

[101] I. Cohen, H. Li, J. L. Hougland, M. Mrksich, and S. R. Nagel, "Using selective withdrawal to coat microparticles," Science **292**, 265 (2001).

[102] J. L. Wyman, S. Kizilel, R. Skarbek, X. Zhao, M. Connors, W. S. Dillmore, W. L. Murphy, M. Mrksich, S. R. Nagel, and M. R. Garfinkel, "Immunoisolating pancreatic islets by encapsulation with selective withdrawal," Small **3**, 683 (2007).

[103] A. M. Gañán, M. Pérez-Saborid, J. M. López-Herrera, and J. M. Gordillo, "Steady high viscosity liquid micro-jet production and fiber spinning using co-flowing gas conformation." Eur. Phys. J. B Condens. Matter **39**, 131 (2004).

[104] A. D. Fitt, K. Furusawa, T. M. Monro, and C. P. Please, "Modeling the fabrication of hollow fibers: capillary drawing," J. Lightwave Tech. **19**, 1924 (2001).

[105] D. V. Boger, "Highly elastic constant-viscosity fluid," J. Non-Newtonian Fluid Mech. **3**, 87 (1977).

[106] X. P. Chen, S. Mandre, and J. J. Feng, "An experimental study of the coalescence between a drop and an interface in Newtonian and polymeric liquids," Phys. Fluids **18**, 092103 (2006).

[107] L. Choplin, P. J. Carreau, and A. A. Kadi, "Highly elastic-constant viscosity fluids," Polym. Eng. Sci. **23**, 459 (1983).

[108] E. Krygier, G. X. Lin, J. Mendes, G. Mukandela, D. Azar, A. A. Jones, J. A. Pathak, R. H. Colby, S. K. Kumar, G. Floudas, R. Krishnamoorti, and R. Faust, "Segmental dynamics of head-to-head polypropylene and polyisobutylene in their blend and pure components," Macromolecules **38**, 7721 (2005).

[109] V. S. Molchanov and O. E. Philippova, "Effects of concentration and temperature on viscoelastic properties of aqueous potassium oleate solutions," Colloid J. **71**, 239 (2009).

[110] S. Schuberth and H. Munstedt, "Transient elongational viscosities of aqueous polyacrylamide solutions measured with an optical rheometer," Rheol. Acta **47**, 139 (2008).

[111] C. Tufano, G. W. M. Peters, P. D. Anderson, and H. E. H. Meijer, "Transient interfacial tension of partially miscible polymers," J. Colloid Interface Sci. **325**, 130 (2008).

[112] C. Clasen, J. P. Plog, W. M. Kulicke, M. Owens, C. Macosko, L. E. Scriven, M. Verani, and G. H. McKinley, "How dilute are dilute solutions in extensional flows?" J. Rheol. **50**, 849 (2006).

[113] V. M. Entov and E. J. Hinch, "Effect of a spectrum of relaxation times on the capillary thinning of a filament elastic liquid," J. Non-Newtonian Fluid Mech. **72**, 31 (1997).

[114] F. Blanchette and W. W. Zhang, "Force balance at the transition from selective withdrawal to viscous entrainment," Phys. Rev. Lett. **102**, 144501 (2009).

[115] J. T. Jeong and H. K. Moffatt, "Free-surface cusps associated with flow at low Reynolds-number," J. Fluid Mech. **241**, 1 (1992).

[116] Y. J. Liu, T. Y. Liao, and D. D. Joseph, "A two-dimensional cusp at the trailing edge of an air bubble rising in a viscoelastic liquid," J. Fluid Mech. **304**, 321 (1995).

[117] S. B. Pillapakkam, P. Singh, D. Blackmore, and N. Aubry, "Transient and steady state of a rising bubble in a viscoelastic fluid," J. Fluid Mech. **589**, 215 (2007).

[118] J. R. Herrera-Velarde, R. Zenit, D. Chehata, and B. Mena, "The flow of non-Newtonian fluids around bubbles and its connection to the jump discontinuity," J. Non-Newtonian Fluid Mech. **111**, 199 (2003).

[119] G. I. Taylor, "The formation of emulsions in definable fields of flow," Proc. R. Soc. A **146**, 501 (1934).

[120] M. R. Booty and M. Siegel, "Steady deformation and tip-streaming of a slender bubble with surfactant in an extensional flow," J. Fluid Mech. **544**, 243 (2005).

[121] C. D. Eggleton, T. M. Tsai, and K. J. Stebe, "Tip streaming from a drop in the presence of surfactants," Phys. Rev. Lett. **87**, 048302 (2001).

[122] R. A. Debruijn, "Tipstreaming of drops in simple shear flows," Chem. Eng. Sci. **48**, 277 (1993).

[123] J. D. Sherwood, "Tip streaming from slender drops in a nonlinear extensional flow," J. Fluid Mech. **144**, 281 (1984).

[124] P. Yue, J. J. Feng, C. A. Bertelo, and H. H. Hu, "An arbitrary Lagrangian-Eulerian method for simulating bubble growth in polymer foaming," J. Comput. Phys. **226**, 2229 (2007).

[125] G. H. McKinley and T. Sridhar, "Filament-stretching rheometry of complex fluids," Ann. Rev. Fluid Mech. **34**, 375 (2002).

[126] S. H. Spiegelberg, D. C. Ables, and G. H. McKinley, "The role of end-effects on measurements of extensional viscosity in fliament stretching rheometers," J. Non-Newtonian Fluid Mech. **64**, 229 (1996).

[127] G. H. McKinley and A. Tripathi, "How to extract the Newtonian viscosity from capillary breakup measurements in a filament rheometer," J. Rheol. **44**, 653 (2000).

[128] K. S. Sujatha, H. Matallah, M. J. Banaai, and M. F. Webster, "Modeling step-strain filament-stretching (CaBER-type) using ALE techniques," J. Non-Newtonian Fluid Mech. **148**, 109 (2008).

[129] G. G. Fuller, C. A. Cathey, B. Hubbard, and B. E. Zebrowski, "Extensional viscosity measurements for low-viscosity fluids," J. Rheol. **31**, 235 (1987).

[130] J. C. Cai, P. R. de Souza Mendes, C. W. Macosko, L. E. Scriven, and R. B. Secor, "A comparison of extensional rheometers," in P. Moldenaers and R. Keunings, editors, "Theoretical and Applied Rheology: Proceedings of the XIth International Congress on Rheology," vol. 2, 1012 (Elsevier, Amsterdam, 1992).

[131] C. G. Hermansky and D. V. Boger, "Opposing-jet viscometry of fluids with viscosity approaching that of water," J. Non-Newtonian Fluid Mech. **56**, 1 (1995).

[132] D. M. Binding and K. Walters, "On the use of flow through a contraction in estimating the extensional viscosity of mobile polymer-solutions," J. Non-Newtonian Fluid Mech. **30**, 233 (1988).

[133] H. H. Hu, "Direct simulation of flows of solid-liquid mixtures," Int. J. Multiphase Flow **22**, 335 (1996).

[134] P. Singh and L. G. Leal, "Computational studies of the FENE dumbbell model in a co-rotating two-roll mill," J. Rheol. **38**, 485 (1994).

[135] G. Astarita, "Objective and generally applicable criteria for flow classification," J. Non-Newtonian Fluid Mech. **6**, 69 (1979).

[136] M. A. Hulsen, R. Fattal, and R. Kupferman, "Flow of viscoelastic fluids past a cylinder at high Weissenberg number: Stabilized simulations using matrix logarithms," J. Non-Newtonian Fluid Mech. **127**, 27 (2005).

[137] T. Schweizer, K. Mikkelsen, C. Cathey, and G. Fuller, "Mechanical and optical responses of the M1 fluid subject to stagnation point flow," J. Non-Newtonian Fluid Mech. **35**, 277 (1990).

[138] J. R. Herrera-Velarde, R. Zenit, D. Chehata, and B. Mena, "The flow of non-Newtonian fluids around bubbles and its connection to the jump discontinuity," J. Non-Newtonian Fluid Mech. **111**, 199 (2003).